# A Scalable Room-Temperature Quantum Processing Network

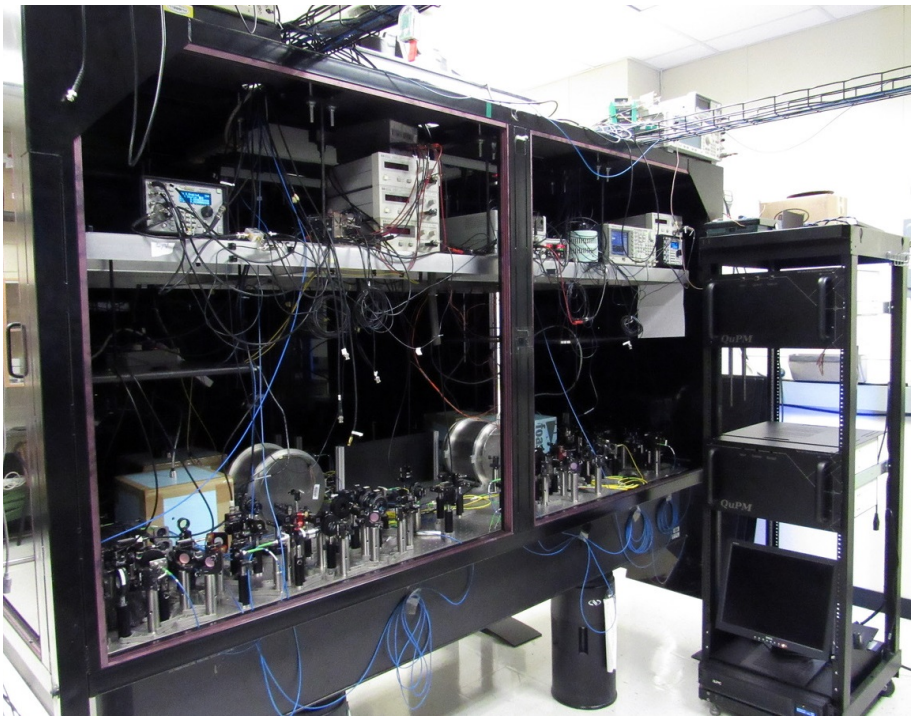

Stony Brook University

**A Scalable Room-Temperature Quantum Processing Network**

A Dissertation presented

by

**Mehdi Namazi**

to

The Graduate School

in Partial Fulfillment of the

Requirements

for the Degree of

**Doctor of Philosophy**

in

**Physics**

**Atomic, Optical and Molecular Physics**

Stony Brook University

**August 2018**

**Stony Brook University**

The Graduate School

Mehdi Namazi

We, the dissertation committe for the above candidate for the

Doctor of Philosophy degree, hereby recommend

acceptance of this dissertation

**Eden Figueroa - Dissertation Advisor**
**Assistant Professor, Department of Physics and Astronomy**

**Dominik A. Schneble - Chairperson of Defense**
**Associate Professor, Department of Physics and Astronomy**

**Tzu-Chieh Wei**
**Associate Professor, Department of Physics and Astronomy**

**Irina Novikova**
**Associate Professor, Department of Physics and SUPA, The College of William & Mary**

This dissertation is accepted by the Graduate School

Charles Taber
Dean of the Graduate School

Abstract of the Dissertation

# A Scalable Room-Temperature Quantum Processing Network

by

**Mehdi Namazi**

**Doctor of Philosophy**

in

**Physics**

**Atomic, Optical and Molecular Physics**

Stony Brook University

**2018**

Quantum mechanical behaviors can be exploited to enhance the current processing and communication capabilities. To do so, several quantum nodes need to coherently work together and manipulate the quantum bits (qubits) in a deterministic manner. A scalable network requires nodes that are capable of generating, storing, gating, transmitting and measuring the targeted qubits. Not only each node is required to do its task with high fidelity, but the quantum interconnectivity between these nodes also has to be designed very efficiently. An exciting direction for releasing large-scale quantum networks is the use of atoms interfaced with light in the form of collective excitations known as dark state polaritons (DSPs).

A major application of DSPs is to store and retrieve single photons with arbitrary polarization states coherently. By applying various experimental techniques, we achieve storage fidelities that surpass any classical strategies in a warm 87Rb atomic vapor. The latest generation of these quantum memories is integrated into quantum-secured networks to extend their transmission

length. It is also possible to create superposition of several DSPs to mimic and investigate relativistic quantum systems. By addressing specific atomic transitions using multiple light fields, we create interaction between the DSPs, following dynamics outlined by Dirac-like Hamiltonians. We use this platform to experimentally simulate relativistic particles with variable mass and the Jackiw-Rebbi model. Similar experiments are also done to induce phase-phase modulation for single photon level pulses using DSPs in closed loops. These devices have all the necessary criteria for building blocks of the first scalable quantum processing network.

# Contents

# List of Figures

One child, one teacher, one book, one pen can change the world.
-Malala Yousafzai

## Acknowledgements

I would like to use this opportunity to thank my adviser, Eden Figueroa, for accepting me into his group within the first half an hour of meeting him and spending the next five years, trying to make a scientist out of me! I cannot remember even one time during my entire Ph.D. track that I ran into a problem and he was not there to reach out and help, whether it was related to my work, the experiments, courses or personal matters. I will always see Eden as my teacher, adviser, friend and my older brother. I also wish to thank Dr. Dominik Schneble whose belief in me was always a major drive to move forward through all these years of graduate school. I had the honor of having him as my teacher for two years and as the head of my Ph.D. committee for four years. I also thank Dr. Tzu-Chieh Wei for following my progress during these years and always being very supportive of me and the project. A special thanks to Dr. Irina Novikova for her scientific guidance and her inspiring work on room temperature quantum technologies which opened a path for many researchers like me to follow. I would also like to thank my colleagues, Bertus Jordaan, Dr. Connor Kupchak, Thomas Mittiga, Connor Goham, Sonali Gera, Dr. Reihaneh Shahrokhshahi, Steven Sagona, Mael Flament, Christopher Ianzano and Alessia Scriminich. Working and being a friend among such a unique and multinational group of highly qualified and brilliant people certainly had many benefits which will help me through my career and life.

## Citations to Previously Published Work

Parts of Chapter 2 have been published as:

"Ultralow-noise room-temperature quantum memory for polarization qubits"
Namazi. Mehdi, Kupchak. Connor, Jordaan. Bertus, Shahrokhshahi. Reihaneh, Figueroa. Eden, Phy. Rev. Applied 8, 034023 (2017).

and,

"Room-Temperature Single-photon level Memory for Polarization States"
Kupchak. Connor, Mittiga. Thomas, Jordaan. Bertus, Namazi. Mehdi, Nolleke. Christian, Figueroa. Eden, Nature Scientific Reports 5 (doi:10.1038/srep07658).

Parts of Chapter 3 have been published as:

"Realizing topological relativistic dynamics with Slow light polaritons at room temperature"
Namazi. Mehdi, Jordaan. Bertus, Noh. Changsuk, Angelakis. Dimitris. G, Figueroa. Eden, arXiv:1711.09346.

Parts of Chapter 4 have been published as:

"Cascading quantum light-matter interfaces with minimal interconnection losses"
Namazi. Mehdi, Mittiga. Thomas, Kupchak. Connor, Figueroa. Eden, Phy. Rev. A 92, 033846 (2015).

Parts of Chapter 5 have been published as:

"Free-space quantum communication with a portable quantum memory"
Namazi. Mehdi, Vallone. Giuseppe, Jordaan. Bertus, Goham. Connor, Shahrokhshahi. Reihaneh, Villoresi. Paolo, Figueroa. Eden, Phy. Rev. Applied 8, 064013 (2017).

Parts of Chapter 6 have been published as:

"Room temperature conditional $\pi$-phase shifts mediated by simultaneously

propagating single-photon level pulses"
Shahrokhshahi. Reihaneh, Sagona-Stophel. Steven, Jordaan. Bertus, Namazi. Mehdi, Figueroa. Eden, arXiv:1803.07012.

# Chapter 1

# Universal Quantum Networks

Quantum mechanics is the realm of bizarre properties. As important as it is to understand these behaviors which form the reality of our universe, it is essential to explore the extent to which we can exploit these properties to our technological advantage. Quantum information science and technology is one of the most attractive research topics of this decade with the promise of leveraging quantum properties of fundamental particles in order to enhance our capability to process and transfer information. Such devices not only can be used to improve our daily life by creating un-hackable communication networks or exponentially faster computers, but also to answer questions about the fundamentals of this universe and the quantum mechanics itself through quantum simulation and computation.

More than three decades of research in the field have resulted in recognizing several suitable quantum platforms based on photons, atoms, ions, Josephson junctions and possibly the Majorana particles. There are merits in using each

of these bases as quantum bits (qubits) but in this dissertation we will primarily focus on a quantum information processing platform based on light-matter interfaces. As it stands today, there are a variety of physical systems which have successfully proven to operate as true quantum light-matter interfaces for quantum information, a few among them being, ultra-cold atoms, cavity QED single-atom systems and cryogenically cooled crystals [1].

In this chapter we will discuss the key criteria for creating a network of such quantum interfaces and the advantages of using room temperature devices. The following chapters will then explore in depth how our proposed platform satisfies all these criteria as a strong candidate for a scalable quantum processing network.

## 1.1 Room-Temperature Quantum Devices

The possible technological and societal implications of merging quantum mechanics with information science have been the driving motivation behind many scientific advancements involving the coherent control of individual quantum systems [2, 47, 4, 49]. Novel ideas have been proposed for combining and engineering individual systems that could suffice as the nodes of a future quantum information processing architecture, or rather a quantum processor. These ideas emanate from the fact that a functional and dependable quantum information processor would be at the core of any system capable of quantum computing [6, 121] and communication [8]. With recent experimental progresses in regard to the advancement of quantum devices, we are now at a

point where we must interconnect many quantum devices to bring about the first generation of scalable but practical quantum networks. However, despite much success and seminal findings [123], interconnections between room temperature based systems have not been attempted to date. In any optical-based, elementary quantum processor, individual nodes must be equipped with the functionality to perform several key tasks in order to meet the criteria necessary for quantum information processing. Namely, some nodes need to be able to receive, store and retrieve photonic qubits (quantum memories), while other nodes must be geared toward the manipulation of qubits (quantum gates). At the present time, room temperature systems often receive a negative connotation in this regard, since they can be plagued by noise and behave poorly in the maintaining of quantum coherence, and are therefore labeled as unsuitable for the aforementioned tasks. However, recent studies have demonstrated that with innovative and novel techniques, room temperature quantum operation is now a serious possibility [10, 11, **?**, 55, 13, 14]. An advancement in room temperature technologies to the level of practical quantum devices would have an enormous impact on the field. Most notably because warm vapors alleviate any need for laser trapping and cooling in vacuum or cryogenic temperatures and lend themselves towards relatively inexpensive and engineer friendly designs.

.

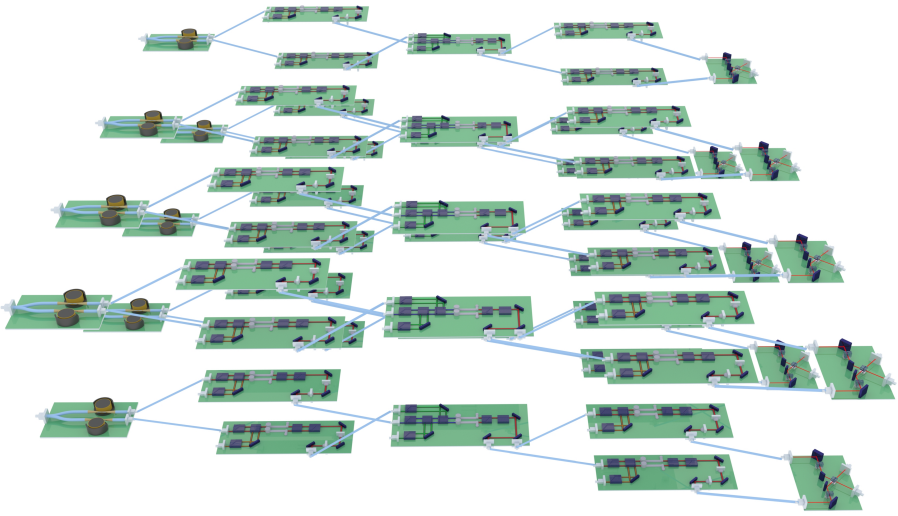

Figure 1.1: A conceptual demonstration of a scalable quantum processing network.

### 1.1.1 Quantum Memories

Optical room-temperature systems have shown much promise towards advanced optical technologies with progressions such as the miniaturization of vapor cells [15] and their integration into photonic structures for applications like light slow down [16], four-wave mixing [17], cross-phase modulation [18] and storage [14]. Using storage of light as an example, atomic vapors can operate with high efficiency (87%) [19], large spectral bandwidth (1.5 GHz) [20] and storage times on the order of milliseconds [123]. Vapor systems have also proven their ability to preserve non-classical properties in the storage and retrieval of quantum light states [21, 22, 124, 125]. In regard to polariza-

tion qubits, states were shown to be stored with high fidelity in experiments involving bright light pulses [25, 26]. However, complete quantum memory operation, i.e. storage of polarization qubits at the single photon level, was thought not possible due to the large control-field-related background photons constraining the signal-to-background-ratio (SBR) during retrieval, and only very recently have results demonstrated otherwise [27].

Currently, three main species of room-temperature memories exist to overcome this SBR obstacle. First is electromagnetically induced transparency with $\mu$s long pulses [**?**]. The second is the use of an off-resonant Raman configuration and fast ns long pulses (faster than the decoherence rates of the system) [20]. A third approach is the use of photon echo schemes combining off-resonant Raman absorption lines with magnetic field gradients (GEM memory) [19]. So far, the only room temperature system in which polarization qubits have been preserved at the single photon level is the EIT approach.

## 1.2 Quantum Systems

Although every quantum information device is, by definition, capable of creating, manipulating or measuring qubits, the unique advantages of quantum mechanics come into play when several of these devices work together as a system to achieve a unified goal such as quantum teleportation or processing. Before we talk about the minimum prerequisites needed to develop such a synchronized quantum system, we will go over a very important example of such a system with the potential of revolutionizing the telecommunication

field: Quantum Repeaters.

### 1.2.1 Quantum Repeaters

Creating a large scale quantum processing network relies on the ability to propagate the polarization qubits over extended distances. Due to the lossy nature of optical fibers, it is hardly possible to preserve the quantum coherence of the states beyond a distance of 100km. Quantum repeaters provide a pathway to overcome the non-cloning theorem restrictions (Which forbids the act of coping a quantum superposition state in order to multiple it similar to regular transmission amplifiers) [28, 29] and amplify the quantum states through entanglement swapping. Upon on-demand access to two pairs of entangled photons, entanglement swapping allows the entanglement of two photons of each different pair by doing a simultaneous quantum measurement on the remaining two photons. This measurement which results in a second-order quantum interference between the photons by erasing their path information is known as the Bell State Measurement. A simple quantum repeater node in theory can only consist of two separated entanglement sources and a Bell state measuring station. As the scale of the quantum network increases, more and more of these quantum repeater nodes are needed to compensate for the optical fiber losses. But since the entanglement sources are intrinsically non-deterministic and the Bell state measuring station requires the photons of different entanglement sources to arrive simultaneously, quantum repeaters need the help of quantum memories to store each entanglement pair and provide enough buffer

time for the other pairs to be generated. It is of practical importance for these quantum memories to be designed "all-environmental-friendly" and cost efficient, hence operating at room temperature.

Novel ideas have been proposed to combine individual quantum systems to serve as building blocks of a quantum communication network [4, 142, 31, 49, 157] which would eventually help the development process of quantum repeaters . Despite numerous proposals regarding quantum repeater architectures [33, 34] an experiment connecting several quantum devices in a quantum repeater configuration remains an extraordinary challenge [35, 36, 37, 38, 152]. Most of the experimental progress has been targeted at the realization of the DLCZ proposal [160], which is based upon a low-repetition rate probabilistic scheme to generate entanglement. Recent studies have demonstrated that fast room-temperature quantum memories can be used as an alternative strategy to circumvent this restriction [181, 182, 183, 27]. Further advancement along this line will have an enormous impact on the field towards building a quantum repeater, as warm vapor alleviates the need for laser trapping and cooling in vacuum or cooling to cryogenic temperatures. This will lead to inexpensive and commercialization-friendly designs that substantially enhance the practicality and reduce the cost of many-device quantum networks.

It is critical to understand the interconnections between the components of a quantum repeater prototype. In order to predict the entanglement generation rates vs. communication distance in a realistic device, all imperfections must be considered. We can model the behavior of a simple four-memory quan-

tum repeater network using the following relevant performance parameters of the constituent devices: rate of entanglement pair generation at the source ($R_o$), storage efficiency, fidelity and storage time in the quantum memory ($\eta_{st}, F, \tau_{st}$), frequency conversion efficiency ($\eta_{conv}$), detector efficiency ($\eta_{det}$), fiber loss ($\alpha_{fiber}$) and Bell-state-measurement visibility ($\alpha$). In our calculation we assume heralded quantum memories (an option to know when a photon is within the memory deterministically) and probabilistic entanglement swapping. Within this framework the useful entanglement-generation rate can be calculated as:

$$R_{Repeater}(L) = R_o(\eta_{\text{conv}}^4)(\eta_{\text{st}}^2)(10^{\alpha_{\text{fiber}} \cdot L/2})(N^{\log_2(\alpha \cdot (F \cdot \eta_{\text{det}})^2/4)}) \tag{1.1}$$

where $N$ is the number of entangled sources. In order to find the trade-off in the performance parameters of the components, we have targeted the quantum repeater operation to surpass the direct fiber losses $R_{\text{fiber}} = R_o(10^{\alpha_{\text{fiber}} \cdot L})$. Fig. 1.2 shows the parameters that must be achieved in order to develope the first fully room temperature quantum repeater ( the parameters of the figure will be discussed later).

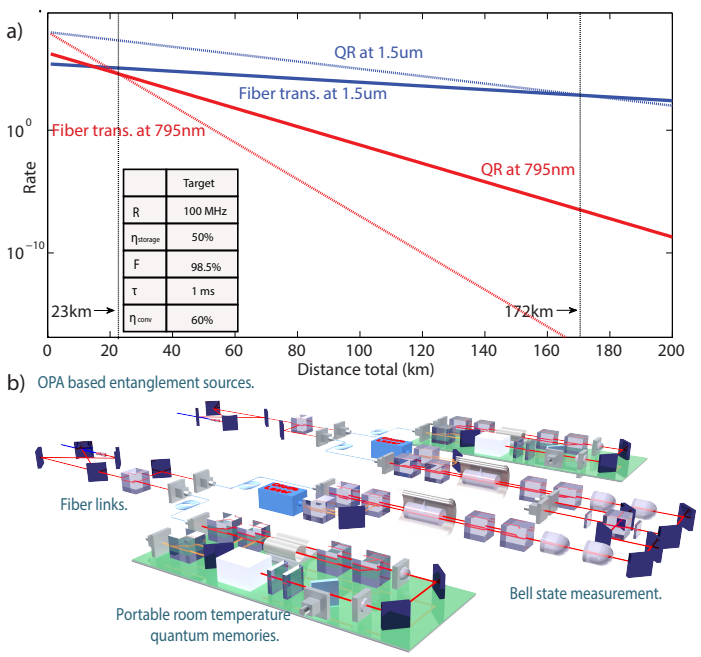


Figure 1.2: a) A four-memory quantum repeater outperforms direct propagation at a distances of $\sim$ 23 km when only the 795 nm wavelength is considered (larger fiber losses) and at $\sim$ 170 km when infrared conversion and transmission at 1367nm are considered. The table shows the trade-off of components' performance used in the simulations, which are the realistic targeted operational parameters of the proposal. QR transmission at 1367nm (solid blue line), direct fiber transmission at 1367nm (dotted blue line), QR transmission at 795nm (solid red line) and direct fiber transmission at 795nm (dotted red line). b) A prototype of a room-temperature four-memory quantum repeater node using table-top entanglement sources.

## 1.3 Three Criteria for a Scalable Quantum System

So far we have discussed the importance of quantum technologies and went over the famous quantum repeater example as a system of many quantum modules working together to achieve a specific goal. In this last section of the introduction, we present three main criteria to meet while designing and implementing a scalable quantum network whether for the means of processing, communication or both.

First and foremost, a quantum processing network requires several quantum nodes, capable of coherently manipulating the quantum information with fidelity near unity. A few examples are quantum memories, quantum simulators, linear and non-linear quantum gates, quantum measuring and sensing, and quantum sources. This is a trivial condition as such a system needs to prepare, modify and read out qubits. Although, as we mentioned above, researchers have developed many of these individual high efficient quantum modules, the second criteria, high fidelity quantum connectivity, prevents us from scaling up the networks. In simpler words, not only do we need highly efficient devices, but we also need optimal connections between these nodes. To achieve this goal, the output of each of these nodes need to be indistinguishable from the optimal input of other quantum nodes. The easiest way to make this quantum impedance matching happen is by using the same platform in all the quantum modules. Finally, for this network to turn into a system, a collection of quantum devices serving towards a specific purpose, the quantum network must

be compatible with the current digital and optoelectrical infrastructure. For instance, secure quantum communication and quantum teleportation are not possible without a classical link for the parties involved to verify the obtained measurements.

Having these three criteria in mind, we bring this chapter to a conclusion by outlining the content of all the chapters that follow:

In Chapter 2 we will start with developing and optimizing our very first quantum node at room-temperature: an EIT-based quantum memory capable of storing arbitrary polarization qubits at single photon level. We will carefully walk through every step of building and optimizing such a device and prove that true quantum operation is possible at such high temperatures. We end the chapter by introducing a novel approach to bring down the retrieval fidelity to near unity as required for a scalable network.

After showing how we can leverage such a room-temperature platform to do true quantum operations, in Chapter 3, we move forward with designing a more sophisticated quantum node, an analog quantum simulator. We will dedicate the majority of this chapter to carefully explain the design of the simulator together with an in-depth theoretical analysis of the involved dynamics. We then provide two experimental examples of how we use light to simulate a 1+1 Dirac particle with variable mass together with a Dirac particle coupled to a spatially dependent mass term. We conclude this chapter by showing how such a platform can be used to do quantum simulation of complex dynamical systems.

After providing sufficient evidence on how room-temperature light-matter in-

terfaces can be used to develop various quantum modules, in Chapter 4, we focus on the second criterion for designing scalable quantum networks: achieving high quantum connection fidelity. We will experimentally implement two networks with each consisting of two quantum memories. In the first network, the memories are in series and we use the control parameters of the first memory to optimize its output to be used as the input of the second node. In the second network, we will have two fully independent dual-rail quantum memories in parallel, and we demonstrate the indistinguishably of their outputs by performing a Hong-Ou-Mandel measurement on the stored photons. This is the key connectivity needed to design a memory-assisted quantum repeater.

After these three chapters, we will be equipped with what we need to design the very first hybrid quantum system at room-temperature in Chapter 5. The system is specifically designed to realize an ultra-high secure communication link between two parties, assisted with a quantum memory module. In this system, we take a look at the third criterion to make sure our quantum memories interact optimally with digital/optoelectrical networks such as an FPGA-based random polarization qubit generator. We will end this chapter by showing how such a network can be scaled up to perform protocols in which quantum memories can help in extending the operating distance beyond the optical fiber limits.

Finally, in the last chapter, we will revisit all the work done at QIT lab at Stony Brook University. We will briefly touch upon parallel yet distinct projects that aim at developing other room temperature quantum nodes such as narrowband single photon sources, quantum frequency converters, and single-photon

level phase-phase modulators. We will finish this dissertation by emphasizing on how all the work is geared toward enabling the creation of a real-life scalable quantum processing system, fully operating at room-temperature and all-environment friendly to be used outside laboratory spaces.

# Chapter 2

# Storage of Quantum Information Through Optimized Light-Matter Interfaces

The focus of this chapter is on designing and optimizing one of the most important nodes in a scalable quantum network; a room-temperature atomic system, capable of mapping photonic states on its collective spin excitation and successfully retrieving it back on the photons at any desired time. Such a device is commonly known as a quantum memory. Although this is a broad definition, there are some criteria to consider for a memory that fits well within our desired networks. Firstly, not only should the quantum memory be able to store and retrieve light at a single photon level, but there should also exist a mechanism that preserves the quantum information encoded on the photons in the form of polarization. This will allow the memory to be used for both

computation and to be integrated in secure quantum communication protocols such as BB84 and measurement device independent quantum key distribution (MDI-QKD).

Secondly, the quantum memory has to demonstrate its potential towards scalability: the possibility to achieve high storage fidelity, storing multiple photons within one unit, efficient cascadability between several memories and an all-environment-friendly operation. Each of these equirements are essential in order to have a network of many memories. Finally, the quantum memories must be compatible with other nodes of a network such as quantum simulators, true random number generators, entanglement sources and photon gates. A very promising technique to satisfy all the above conditions is to use electromagnetically induced transparency (EIT) to create the so-called Dark-State Polaritons (DSPs)[44]. In this chapter, we will go over the basics of designing an EIT-based quantum memory at room-temperature. We will follow the argument by optimizing the memory to work with high fidelities and long storage time. This will create a path to show in the upcoming chapters how to use the same DSPs for quantum simulation by adding several control field lasers to these atom-light interfaces. In the last chapter we will demonstrate the feasibility of introducing these memories in quantum secured networks.

## 2.1 Quantum Manipulation of light at Room Temperature

Measuring quantum mechanical effects at room temperature is counter intuitive due to the inherent decoherence mechanisms associated with single particles in motion. Nevertheless, robust and operational room temperature quantum devices are the fundamental cornerstone towards building quantum technology architectures consisting of several nodes [45, 46]. Given the recent success in the creation of elementary platforms in which single photons interact with atoms in controlled low temperature environments [47, 122, 49, 50], the next technological frontier is the design of interfaces in which quantum mechanical processes can be performed at room temperature [51, 52, 53, 54]. Despite this inherent drawback, many steps have been taken to assure that flying quantum or single-photon level fields are preserved after storage and retrieval in room temperature atomic ensembles in different physical implementations [55, 13, 14, 27]. Despite considerable efforts however, the storage of qubits at room temperature with high enough fidelity to overcome any possible classical strategy has remained a considerable challenge because the extremely weak retrieved light is accompanied by a considerable amount of background light. This problem stems from two main considerations imposed by the thermal motion of the atoms. First, the restriction of mandatory collinear probe/control geometry and second, the creation of background photons at the probe frequency due to the atomic response to the control fields applied[56, 57, 58, 59]. The former restriction caused by the Doppler broadening of the atoms and

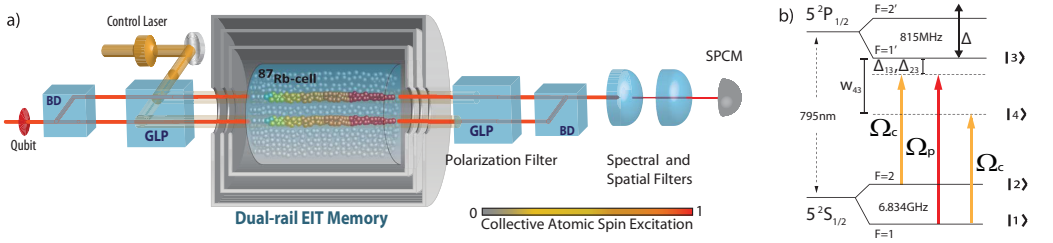


Figure 2.1: (a)Dual-rail quantum memory setup. Probe: red beam paths; control: yellow beam paths; BD: Polarization Beam Displacer; GLP: Glan Laser Polariser; SPCM: Single Photon Counter Module. The color-code bar depicts the strength of the collective atomic excitation. (b) Rubidium D1 line four-level scheme describing the transitions used in the description of the efficiency and background response. $|1\rangle$ and $|2\rangle$ (ground states), $|3\rangle$ (excited state), $|4\rangle$ (off-resonant virtual state) and $\Delta$ (one-photon laser detuning).

the fact that depending on the direction in which an atom moves, it sees a different frequency of the probe and control fields. In order to remain within the EIT bandwidth (which is typically in the order of MHz), the control field must be co-linear with the probe. The relevant figure of merit is the signal-to-background ratio (SBR). With $\eta$ being the retrieved fraction of a single excitation stored in the medium and $q$ the number of concurrently emitted photons in a single try, we define SBR as $\eta/q$. A regime in which the average retrieved fraction of a stored excitation $\eta$ exceeds considerably the average number of background photons $q$ being concurrently emitted is mandatory for room temperature experiments designed to achieve unconditional high qubit fidelities after storage.

## 2.2 Quantum Storage of Light at Single Photon Level

In this chapter we study how the optical response of cold atomic environments is transformed by the motion of atoms at room temperature and consequently characterize the optimal performance of room temperature quantum light matter interfaces. We demonstrate storage of light with 400 ns long pulses containing on average $\bar{n} = 1$ photons in warm $^{87}$Rb vapour using EIT and their retrieval with high SBR. In our setup, one retrieved excitation that has passed a filter system after the cell is accompanied by a background signal that is less than one sixth of the usable probe signal. As the ultimate application of this room temperature ultra-low background retrieval, we also demonstrate full quantum memory operation for polarization qubits in a dual rail system. We achieve an average measured fidelity of 87%, defeating any classical strategy exploiting the non-unitary character of the memory efficiency. We also demonstrate a novel technique to increase the fidelity to values above 95% by introducing a weak auxiliary field. Our achievement decreases significantly the technological overhead required to achieve quantum operation and thus paves the way for the construction of scalable many-memories quantum machines.

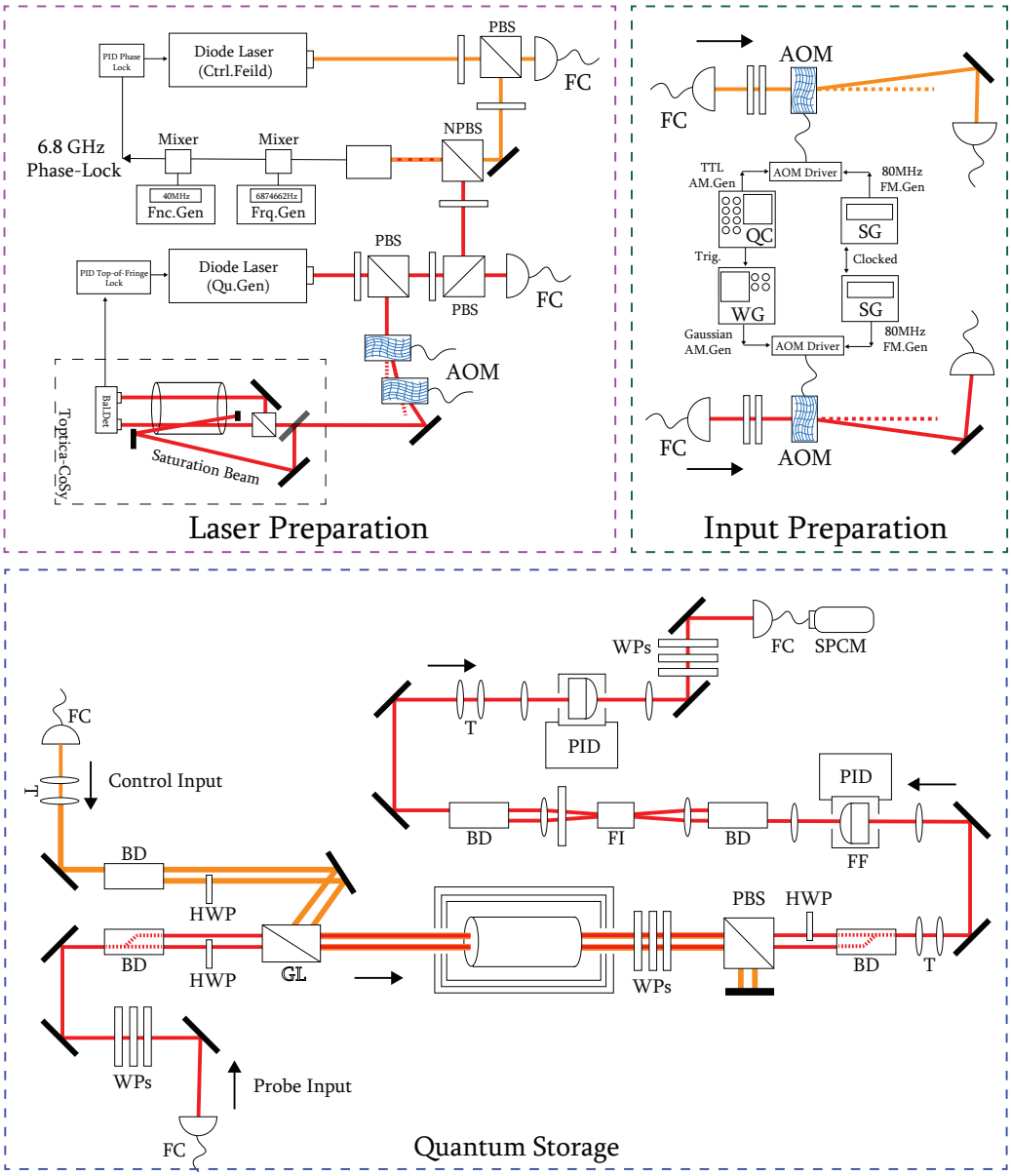


Figure 2.2: The Blueprint for quantum storage of light. Our experimental implementation can be describe in three separate stages, the preparation of the probe and control lasers to maintain the lambda scheme stably, preparation of the qubit and the control field pulsing sequence, and finally the full design of the quantum memory and the filtering system.

## 2.3 Experimental setup

Before we move forward with the optimization process and understanding of the noise dynamics of quantum memories, we will provide a full detailed blueprint of the quantum memory design and the preparation stages before the laser fields enter the memory. Figure 2.2 depicts all the elements used to obtain the experimental results of this chapter. In general, the experimental procedure can be divided into three distinct sections: I. Preparation of two independent laser fields to constantly stay in resonance with the desired Rb transitions at D1 line, II. Qubit preparation and control field pulse generation, and III. quantum storage of light followed by state-of-the-art filtering system.

### 2.3.1 Laser Preparation

Our memory is based on a Lambda-type EIT configuration [27], with a probe field frequency at the $5S_{1/2}F = 1 \rightarrow 5P_{1/2}F' = 1$ rubidium transition at a wavelength of 795 nm (red detuned) and a control field coupling the $5S_{1/2}F = 2 \rightarrow 5P_{1/2}F' = 1$ transition (See Fig 2.1b). At room temperature, EIT has a bandwidth of about 1MHz ( in general this bandwidth is a function of several parameters including the control field power) which forces us to stabilize and lock both the lasers to the lambda transitions very precisely. We achieve this goal in two steps; using saturation spectroscopy we first lock the probe field to F=1 to $F' = 1$ transition, after which we phase-lock the control field to always transmit light at exactly 6.8348 GHz away from the probe laser. Since the PID lock for the probe locks the laser only on the top (and side) of the

fringe, to induce large two-photon detunings (larger than 50MHz), we place an acousto-optic modulator (AOM) setup before the locking beam enters the saturation spectroscopy setup (See fig 2.2, laser preparation). This way, although the PID locks on the top of the peaks generated using the sat spec, the frequency of the laser will be shifted from the resonances depending on the AOM setup. As we will discuss in the future sections, most of the experimental results in this thesis have been achieved with one-photon detunings ranging between 200MHz to 400MHz. The locking system in our setup is realized with a Toptica DigiLock system and is fully automated.

In order to stabilize the control field laser, we use a phase-lock setup. A phase-lock setup not only generally locks the frequencies of the two lasers to each other within a Hertz range, it is precise enough to maintain the relative electrical phase of the two fields as well. This is crucial for the case of storage because the atoms store the electrical phase of the photons on their collective spin excitation. Achieving the maximum retrieval efficiency depends on how well we maintain the relative phase of the probe and writing control field at the moment of storing compared to the phase between the atomic spin excitation and the readout control field at the moment of retrieving. The phase-lock setup obtains a beat note between the two lasers with a frequency of 6.8GHz which is too high for most conventional spectrum analyzers to be able to display. To solve this problem, we mix this beat-note with a signal generated by a very precise frequency generator and only few MHz different from the 6.8GHz Rb ground state splitting. Currently we have chosen the signal to be generated at 6.874 GHz which is 40MHz away from the ground state splitting.

A function generator creates a signal at 40MHz to be used as the reference by the PID lock and both the final beat-note and the 40MHz reference signal go to a spectrum analyzer. This way we can simply change the offset of the control laser scan until its frequency is exactly 6.834MHz away from the probe and the beat-note overlaps with the reference signal on the spec analyzer.

### 2.3.2 Input Preparation

After locking both lasers to the atomic transitions, we temporally shape the fields entering the memory. The master trigger for the experiment is generated by a Quantum Composer (QC) device (See fig 2.2, Input preparation). We generally choose a repetition rate of 25kHz (40 $\mu$s long cycles) to provide enough time for optical pumping of the atoms to the F=1 ground state. This rate can conveniently be increased to 100kHz but to go faster we need to move from EIT to Raman regimes. A Raman memory can be realized using a lambda configuration but with largely detunned fields (in GHz range). The underlying physics of these systems is outside the scope of this thesis. EIT provides long storage times, but its narrow bandwidth limits the photons temporal shape to be wider than several hundreds of nanoseconds. Raman memories can store picosecond pulses for up to a few nanoseconds. After setting the repetition rate, we use a TTL signal generated by the QC as the master trigger for all the electrical components in this chapter including the AOM drivers and the SPCMs.

The shaping of the probe is controlled by a Wave Generator (WG), triggered

by the quantum composer to generate one 400ns FWHM Gaussian envelope per trigger. This pulse is then sent to the AOM driver as the Amplitude Modulation (AM) input. Commercial AOM drivers are typically equipped with an internal local oscillator to generate the frequency modulation (FM) to the amplifier. We have estimated a systematical uncertainty of 30kHz for these oscillators, hence, we bypass them and use a signal generator to generate a precise 80MHz reference signal (Hertz level precision). This modulation results in a $\pm$ 80MHz one-photon detuning in the experiment, depending on which diffraction order of the AOM crystal we select to use. Although the WG controls the amplitude of the Gaussian envelope which in turn controls the optical pulse intensity, it is not capable of single-photon level pulses. To do so, we add adequate optical attenuators to bring down the intensity to any desired level. We can also prepare the polarization state at this station using optical waveplates. The final qubits are then sent to the quantum memory through single-mode non-polarization-maintaining optical fibers.

### 2.3.3 Quantum Memory preparation

In general, quantum storage happens in two steps. First we store the single photon pulses using a dual-rail EIT configuration and then we filter out the background noise by means of polarization and frequency filters. Upon receiving the qubits at the probe input (see fig 2.2, quantum storage), a series of wave-plates compensate for the unitary polarization rotation of the optical fibers. After that, the probe passes through a beam displacer (BD) element

to allow for the storage of the polarization encoded on each pulse. Our BD is a birefringent crystal that allows the vertical component of a polarization to pass through straight but it displaces the horizontal part by 4mm (the displacement distance varies depending on the crystal). On a classical level, a BD splits a laser beam into two parallel beams of H and V polarized light. On a quantum level, any polarization state is a superposition of $|H>$ and $|V>$; BD maps this polarization superposition onto a spatial superposition of left and right rails while maintaining the relative phase between each rail. A half wave plate (HWP) rotates the polarization of the $|V>$ rail to $|H>$ in order for both the rails to pass through the Glan-Laser (GL) before entering the Rb cell.

Two independent control beams coherently prepare two volumes within a single $^{87}$Rb vapor cell at 62° C, containing Kr buffer gas to serve as the storage medium for each mode of the polarization qubit. This is achieved by passing the control beam through a separate BD, rotating the polarization of one of the rails to allow both rails to reflect inside the GL and overlap on top of the probe rails. To ensure that the control field rails fully cover the probe rails, a 1:2 telescope is placed at the control input. The vapor cell is placed at the center of three co-centric mu-metal cylindrical shields to reach a magnetic field attenuation of less than micro-Gauss order. Its temperature is controlled using a PID loop. We have selected the 62° C experimentally by measuring the SBR vs. T for a range of 55° C to 65° C and realized that around 62° C the optical density is high enough to result in efficient storage without creating excessive amount of background noise. To avoid any overheating, we use

high-duty Solid-State Relays and a secondary limit-PID to cut the main input power if the temperature raises above 90° C. Inside the vapor and under EIT condition, each mode propagates as a combined collective atomic and electromagnetic excitation (dark state polaritons) at a reduced group velocity in its respective volume. When the control fields are adiabatically switched off, the excitations turn into a purely atomic one and remain stationary within the cell. Switching the control fields back on 0.5-1 $\mu$s later reverses the storage procedure recreating the electromagnetic part of the excitation. After storage, the rails are recombined to recuperate the polarization qubit using another BD. As it is demonstrated in figure 2.2, the dual rail setup is implemented symmetrically to avoid any path difference between the $|H>$ and $|V>$ rails.

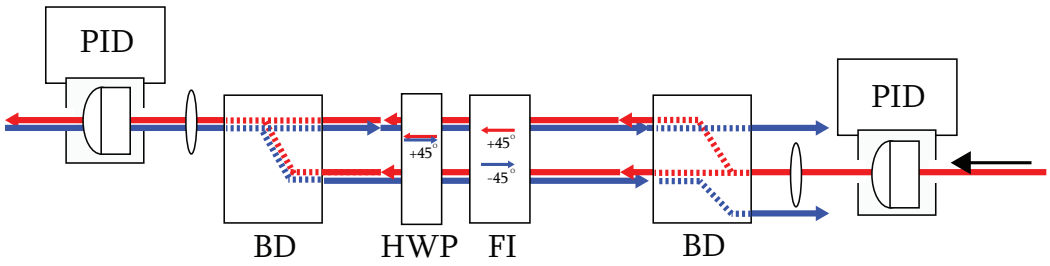


Figure 2.3: Polarization Maintaining Faraday Isolation Setup. We have implemented a design consistent of two Beam Displacers, one Faraday Isolator, one Half Wave-Plate angled at 45 degrees and two focusing lenses to prevent the back reflection of the second etalon to enter back inside the first etalon. Such an implementation is necessary in a polarization quantum memory setup to eliminate the back reflection beam without altering the polarization qubits. The combination of the FI and the HWP result in different polarization rotation depending on the direction of the laser beam. Here, the red beam represents the probe field and the blue is the back reflection.

Atoms at room temperature experience a Doppler broadening of 550MHz while the EIT bandwidth is only a couple of mega-Hertz. In order for the control field to effectively lie within this bandwidth it must be co-propagating with the probe. At the single photon level, after successfully retrieving the stored pulse, we must then eliminate $10^{12}$ unwanted photons of the control field. The first step is to filter the control field based on the polarization. A polarizing beam splitter (PBS) right after the vapor cell separates the vertically polarized control field photons from horizontally polarized probe pulses with an extinction ratio of 42 dB. After recombining the rails, probe and remaining control photons enter a frequency filter setup consisting of two Etalon Fabry-Perot cavities connected to each other with a polarization maintaining Faraday Isolator (FI). The Etalon crystals are 7.5mm and 4.0mm thick, corresponding to a free spectral range (FSR) of 13GHz and 21GHz respectively. In the last part of this chapter we will discuss the reason for choosing etalons with different FSRs but the tens of GHz range is to allow the control field frequency (-6.8GHz away from the probe) to lie between the transmission peaks. After a careful mode-matching process, the probe passes through the transmission peaks with 20-40MHz FWHM while each etalon provides a 50 dB control field attenuation. The fine tuning of the transmission frequency is done by controling the temperature of the etalon using a PID system with a precision of 0.01K. A magnetic FI is used to prevent the back reflection from the second etalon into the first one. Conventional FIs induce a 90 degrees polarization rotation between the forward and backward beams and deflect the backward beams using two PBSs. Due to the use of PBSs, these isolators are polariza-

tion selective which goes against the nature of our quantum memory. To avoid this issue, the two PBSs are replaced with two BDs (see fig. 2.3). This setup shifts the back-reflected beam and prevents it from entering the first etalon. Combined together, the filtering setup achieves 144 dB control field suppression while yielding a total 4.5% probe field transmission for all polarization inputs, exhibiting an effective, control/probe suppression ratio of 130 dB.
Finally, the stored pulses are sent to a single photon counting module (SPCM) which is triggered by the quantum composer to plot the histograms of the input pulse and the storage. To evaluate the polarization of the qubits we use a rotating quarter wave plate (QWP) and a horizontal polarizer (HP) before the SPCM. The intensity oscillation caused by the rotation of the QWP can be plotted versus the angle of the plate. We then evaluate the Stokes vectors of stored qubit states by fitting the Stokes equation of the QWP and the HP to these plots. In the rest of this chapter we will take a closer look at the atomic dynamics at room temperature and investigate various sources of noise and how to optimize the signal to background ratio of the output pulses.

## 2.4 Room temperature operation description

The key element to understand the performance of our device is to translate the optical response of stationary atoms to atomic media in which the atomic motion at room temperature drastically modifies such response. In general, a narrow frequency response in an ultra-cold atomic system has to be modified

by a velocity distribution of probable atomic responses to compensate for the Doppler effect experienced by moving atoms. Besides this, when the Doppler width of an atomic resonance is of the same order as the hyperfine splitting of an excited states, the cross influence of each resonance has to be considered. This is not the case in ultra-cold atomic systems in which each hyperfine line is addressed independently.

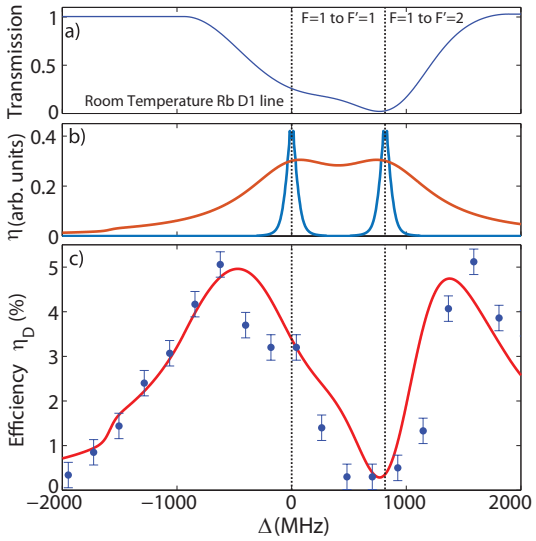


Figure 2.4: (a) Measured transmission profile $T_{RT}(\Delta)$. (b) Cold atom storage bandwidths $\eta_1(\Delta)$ and $\eta_2(\Delta)$ for the two excited states of the rubidium D1 line manifold (the blue line is a master equation prediction of the storage bandwidth) and room temperature storage bandwidth $\eta_{RT}(\Delta)$ (the solid red line is the result of the convolution with a velocity distribution). (c) Overall efficiency response $\propto (\eta_{RT}(\Delta))(T_{RT}(\Delta))$ (solid red line) and storage experiments over a 4 GHz scan region with a central frequency at the $F = 1$ to $F' = 1$ D1 line rubidium transition (blue dots). The error bars are statistical.

In order to exemplify how the response of ultra-cold atoms translates to room temperature we consider non-moving atoms exhibiting a double $\Lambda$-energy

level scheme. The double Λ-level scheme is characterized by the interaction with two laser fields, $\Omega_{p1}$ (probe) and $\Omega_{c1}$ (control), with one-photon detunings $\Delta_1$ and $\Delta_2$ respectively (see Fig. 2.1b) and the off-resonant interaction of the control field with a virtual state. The Hamiltonian which describes the atom-field coupling in a rotating frame is given by [126]:

$$\begin{aligned} H &= -\Delta_{13}\sigma_{11} - (\Delta_{13} - \Delta_{23})\sigma_{22} - \Omega_p E_p \sigma_{31} - \Omega_c E_c \sigma_{32} \\ &- \alpha_1 \Omega_c E_c \sigma_{41} - \alpha_2 \Omega_c E_c \sigma_{42} + (\Delta_{13} - \Delta_{14})\sigma_{44} + h.c \end{aligned} \tag{2.1}$$

where $\alpha \propto \frac{1}{\Delta_{14}}$ is the coupling parameter to the virtual state, $\hat{\sigma}_{ij} = |i\rangle\langle j|, i, j = 1, 2, 3$ are the atomic raising and lowering operators for $i \neq j$, and the atomic energy-level population operators for $i = j$ and $E_{p1}(z,t)$ is the normalized electric field amplitude of the probe.

The frequency bandwidth of the storage event in a cold atomic cloud can be obtained numerically by solving the master equation for the atom-light system:

$$\begin{aligned} \dot{\hat{\rho}} &= -i[\hat{H}, \hat{\rho}] + \sum_{m=1,2} \Gamma_{3m}(2\hat{\sigma}_{m3}\rho\hat{\sigma}_{3m} - \hat{\sigma}_{33}\hat{\rho} \\ &- \hat{\rho}\hat{\sigma}_{33}) + \sum_{m=1,2} \Gamma_{4m}(2\hat{\sigma}_{m4}\rho\hat{\sigma}_{4m} - \hat{\sigma}_{44}\hat{\rho} - \hat{\rho}\hat{\sigma}_{33}) \end{aligned} \tag{2.2}$$

together with the Maxwell-Bloch in an atomic sample of finite-length $L$:

$$\partial_z E_{p1}(z,t) = i\frac{\Omega_{p1} N}{c}\langle\hat{\sigma}_{31}(z,t)\rangle \tag{2.3}$$

Here the Gammas are the decay rates of the excited levels, $c$ is the speed

of light in vacuum and $N$ the number of atoms participating in the ensemble. Numerically solving this set of equations we can calculate the expected retrieved pulse shape $E_{OUT}(t)$ for different detunings, thus obtaining the storage efficiency bandwith response of a non-moving atom $\eta(\Delta_1)$.

In a room temperature system the atomic motion influences the atomic response in the form of field detunings, as light is blue shifted for atoms moving in one direction while red shifted for atoms moving in other direction, thus atoms respectively experience $\Delta_{\pm i} = \Delta_0 \pm i\Delta$ detunings in the addressing fields. The room temperature response can be calculated by a weighted average of the cold atom storage efficiency bandwidth $\eta(\Delta)$ and the distribution of possible atom velocities at certain temperature:

$$A(\Delta) : \eta_{RT} = A(\Delta_0)\eta(\Delta_0) + \sum_{i=1}^{\infty} A(\Delta_{\pm i})\eta(\Delta_{\pm i}) \tag{2.4}$$

where:

$$A(\Delta - \Delta_0) = A(2\pi v/\lambda) = \frac{\sqrt{Ln2}}{W_d\sqrt{pi}} \frac{1}{1 + (\Delta - \Delta_0)^2/W_d^2} \tag{2.5}$$

the Doppler distribution of velocities. The latter assumes the laser frequency to be tuned to the atomic resonance, with $A(\Delta_0) = A_0$ . For the case in which laser frequency is detuned by $\Delta'$ from the atomic resonance, the response is calculated as:

$$\eta(\Delta') = A(\Delta_0)\eta(\Delta_j) + \sum_{i=1}^{\infty} A(\Delta_{\pm i})\eta(\Delta_{j\pm i}) \tag{2.6}$$

The final response of the room temperature system is obtained by considering the influence of the absorption profile in the previous equation.

Using our dual-rail system we have tested the room temperature response of the system by performing storage experiments in which we have varied the one photon detuning $\Delta$ of our Raman laser pair over a 2 GHz region centered around the 1 to 1 D1 line rubidium transition. Fig. 2.4c shows the results of our experiments and the prediction of the simulation. The most important observation is that as a result of the atomic motion, maximum storage efficiency is not achieved at atomic resonance (as expected in a cold atomic system), but in regions beyond the Doppler width of the resonance. In our particular case, maximum efficiencies are at $\Delta'$= 500 (red detuned) and $\Delta'$= 1.2 GHZ (blue detuned).

### 2.4.1 Noise mechanism at room temperature

As discussed in the introduction, the relevant figure of merit of a room temperature quantum memory is the SBR and thus the efficiency response does not represent a complete picture. The Liouville equation that we have used in equation 2.2 contains decay terms for all atomic level and thus can also offer an insight into the leading dynamics of noise/background processes. With this in mind we simulate the dynamics of the system using pulses of control field light (without probe light present) and evaluate the atomic coherences that are transmitted through or frequency filtering for varying one photon detunings $\Delta'$. Fig. 2.5a shows the combined frequency response of the transition $|1>$ to $|3>$ and $|2>$ to $|4>$. The important feature of the response is the existence

of two bandwidths; a narrow line associated with photons incoherently scattered from the excited state $|3>$ as a result of population exchange with the virtual state $|4>$, mediated by decoherence rates between the ground state $|2>$ and $|3>$. The second feature is a broad frequency response associated with photons scattered from the virtual state $|4>$ (Stokes field) through an off-resonant coherent Raman process.

As an outcome of the numerical simulations and experimental data taken in the frequency space of the RT light-matter interface, a one-photon detuning of $220MHz$ is applied for the storage of light pulses with an average $n = 1$ photons with $|H>$ polarization using only a single rail setup (see Fig. 2.6a). The achieved results show SBRs above 6.5 for a storage time of 500ns and above 4.5 up to $1\mu$s (Fig. 2.6a inset). Such high SBRs can result in qubit storage fidelities above the classical threshold (due to the direct connection between SBR and polarization storage fidelity) as long as the quantum memory treats all the polarizations on the Poincare sphere the same way. To insure this, we store all six orthogonal polarization bases ($|H>$, $|V>$, $|D>$, $|A>$, $|R>$, and $|L>$) in a dual rail memory setup, where the background is inevitably twice that of the single rail (Fig. 2.6b). The outcome is an average SBR of 2.8 with average efficiency of 5% for all the polarizations.

As explained in section 3, the polarization of each of these stored qubit states is evaluated using a rotating quarter wave plate (QWP) and a horizontal polarizer (HP) before the single photon counter. The intensity oscillation caused by the rotation of the QWP can the plotted versus the angle of the plate. We obtain the Stokes vectors of stored qubit states through fitting the

Stokes equation of the QWP and the HP to these plots (See Fig. 2.7a-f). To evaluate the total polarization fidelity we follow this procedure: First we measure the polarization of all the input states. Since the average degree of polarization of the stored qubit states is high due to the ultra-high SBR, there is no need to separately measure the polarization of the input states propagating through the whole system. Instead we directly operate the polarization qubit storage experiment and take the polarized part of the Stokes vectors of these qubit states as the rotated input states ($S_{in}$) (Fig. 2.7g). Finally, we analyze the polarization of the stored qubits ($S_{out}$) to compare it with $S_{in}$ and to find the total fidelity using $F = \frac{1}{2}(1 + \mathbf{S}_{out} \cdot \mathbf{S}_{in} + \sqrt{(1 - \mathbf{S}_{out} \cdot \mathbf{S}_{out})(1 - \mathbf{S}_{in} \cdot \mathbf{S}_{in})})$. Figure 2.7h shows how well all the storage states keep their length and orthogonality on the Poincare sphere.

For a $< n >= 1$, the average fidelity obtained using this method is $86.5 \pm 0.8\%$ which is more than $3\sigma$ above 83%, the maximum fidelity of any classical strategy for a system with coherent light source and storage efficiency of 5% [61]. This, to our knowledge, is the first reported Room Temperature Quantum Memory for polarization qubits.

### 2.4.2 High-SBR quantum memory operation.

Although we have shown the true quantum operation of a polarization memory at room temperature, for many practical network applications the fidelity needs to be higher than 95%. In this section we briefly review a novel method, developed by us [126], which opens the doorway for such high fidelity operation at room temperature by coherently eliminating the four wave mixing noise. As

the first step, we have assumed the background response $Q(\Delta)$ to be a combination of two quantum fields produced by different physical mechanism and differing by 13.6 GHz. We have tested this concept by replacing one of the etalons in the filtering system with a similar unit with different free spectral range. This allow us to eliminate the background produced by scattering from the virtual state $|4\rangle$.

Moreover, we achieve noise elimination using a self interacting spinor (NESIS) by applying an additional weak auxiliary beam on resonance with the $5S_{1/2}F = 1 \rightarrow 5P_{1/2}F' = 1$ transition that remains on during the complete storage procedure [126]. We create an interaction between two dark-state-polariton modes (spinor components), one formed by the auxiliary field and $\Omega_c$, and one by $\Omega_c$ and the scattered photons from state $|3\rangle$ [60]. The interaction between the spinor components results in maxima/minima in the background noise depending on the phase relation between the auxiliary and control fields, independent of the probe field. By storing and retrieving the probe light with a small two-photon detuning, we further guarantee independence between the two processes, thus creating a noise-free region without altering the retrieved photons. A numerical modeling of the complex spinor component interactions involved in the NESIS technique is currently being developed by our group.

Figure 2.8a shows the obtained maxima/minima together with storage of pulses with $\langle n \rangle = 6$ and an increased control field power in order to highlight the aforementioned dynamics. By controlling the phases of the auxiliary and control fields using passive elements, we overlap the retrieved pulse with

the noise-free region (see Fig. 2.8a), translating into a SBR $> 25$ for the single-photon level case.

Applying the NESIS technique together with active phase control in each of the qubit rails in the polarization quantum memory shown above will allows us to achieve corresponding qubit fidelities $> 98\%$. Having such noise-reduction techniques in place will permit the use of higher optical depths and control field powers, leading to storage efficiencies above 50%, already establishing our system as a viable alternative to cryogenic and cold-atom technologies [62, 63]. Our results are a viable alternative to techniques using either cavity suppression [64], or ultra-fast pulse operation [65, 66, 67, 68].

We finish our investigation by improving the achievable storage times. We have used a different cell with a different amount of buffer gas and a low collisional depolarization cross-section (30 Torr Neon) and achieved storage times of $\sim 50$ $\mu$s at the few-photon-level (see Fig. 2.8b). By adding anti-relaxation coatings to the interior cell walls, storage times of $\sim 1$ ms are within reach.

## 2.5 Summary

Quantum properties are typically assigned to very small particles and numerous experiments have shown that the quantum effects vanish as the system becomes noisier. This behavior can be explained by quantum decoherence. In fact, regardless of the size or the environment, as long as the objects (or in our case qubits) maintain their quantum coherence they will obey the universal quantum laws. In this chapter we showed how an extensive optimization in

the parameter space can result in obtaining a fully quantum operation at a noisy room temperature system. As an example, we leveraged the light-matter interface to store polarization qubits with high read-out fidelity. In the next chapter we will explore another potential application of such interfaces by tuning the system for quantum simulation. The concept is practically the same, but this time we will introduce additional control fields to reshape the global Hamiltonian and force the DSPs to follow wave-propagation equations that mimic relativistic particles.

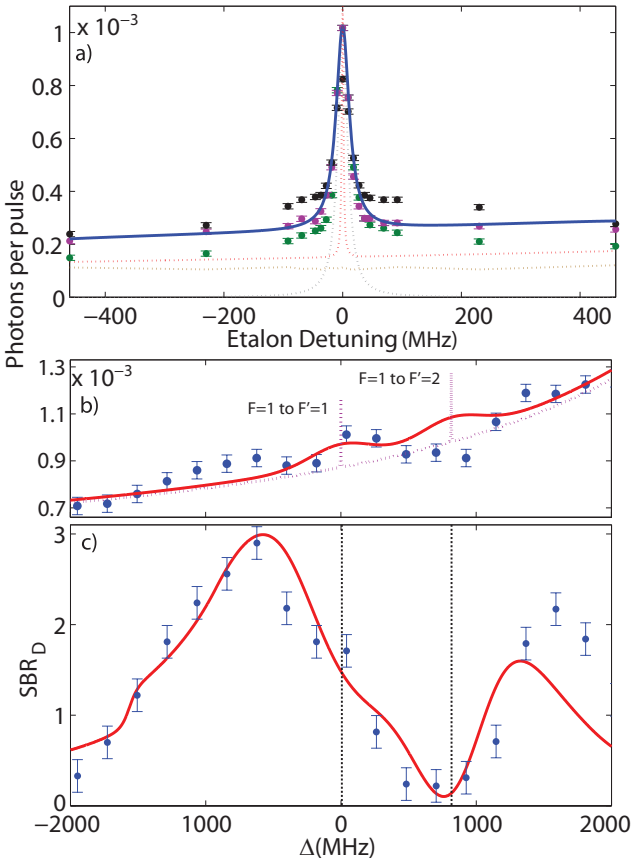


Figure 2.5: (a) Cold atom background response $Q(\Delta)$ (dashed red-line) featuring the contributions of incoherent scattering and Stokes fields; etalon transmission profile (dashed blue line); convoluted response indicating the background transmission through the filtering elements (solid blue line); experimental background measurement for $\Delta = -500$ MHz (green dots), 0 MHz (purple dots) and +500 MHz (black dots); technical background (brown dotted line). (b) Cold atom background bandwidths $Q_1(\Delta)$ and $Q_2(\Delta)$ for the two excited states of the rubidium D1 line manifold (the purple dotted line is a master equation prediction of the background bandwidth); warm atom background response $Q_{RT}(\Delta)$ ((the solid red line is the result of the convolution with a velocity distribution)); background measurements vs. $\Delta$ (blue dots). (c) Predicted room temperature signal to background ratio $SBR_{RT} \propto (\eta_{RT}(\Delta))(T_{RT}(\Delta))/(Q_{RT}(\Delta))$ (solid red line); SBR experimental measurements (blue dots). The error bars are statistical.

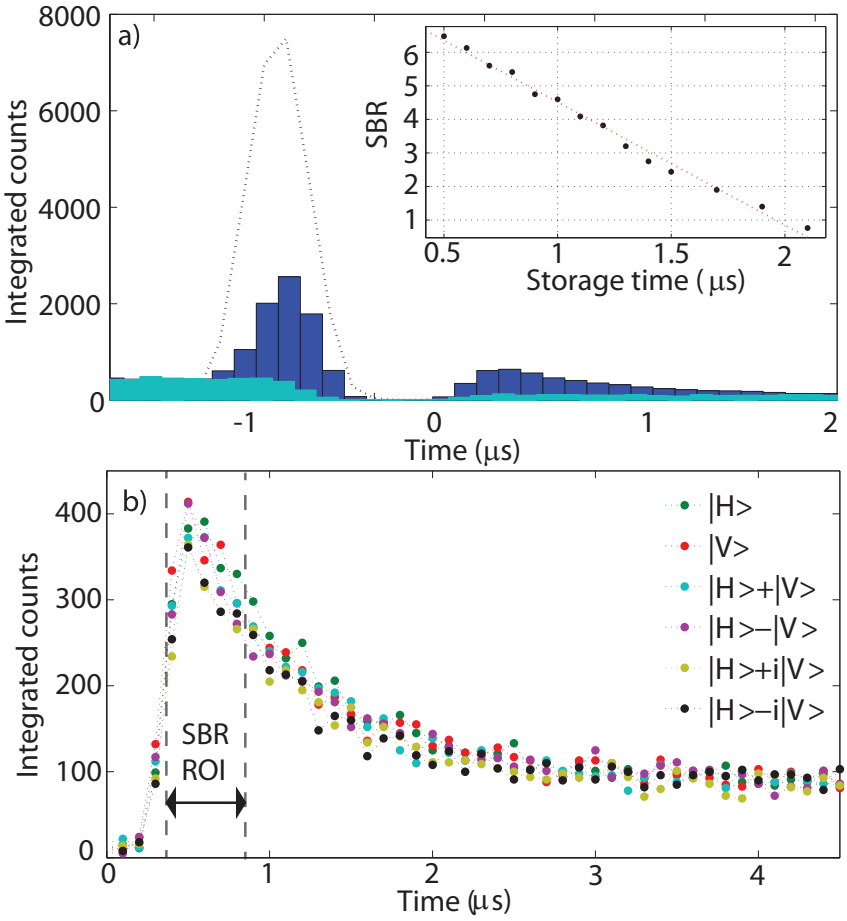


Figure 2.6: (a) Single rail storage with SBR of about 6 where the histogram of photons counts shows the retrieved signal (dark blue bars) compared background counts (light blue bars), the original pulse is shown by the dotted black line. Inset: SBR vs. storage time (black dots) and experimental fit (redline). (b) storage efficiencies for six different input polarizations using the dual rail system.

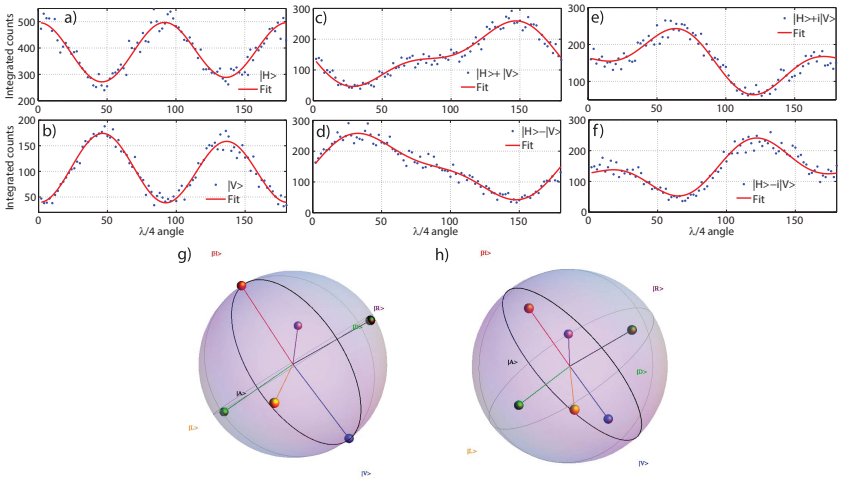


Figure 2.7: Unconditional quantum memory for polarization qubits. (a) Polarization analysis of six different retrieved qubits. (b) Poincare sphere of original and retrieved states.

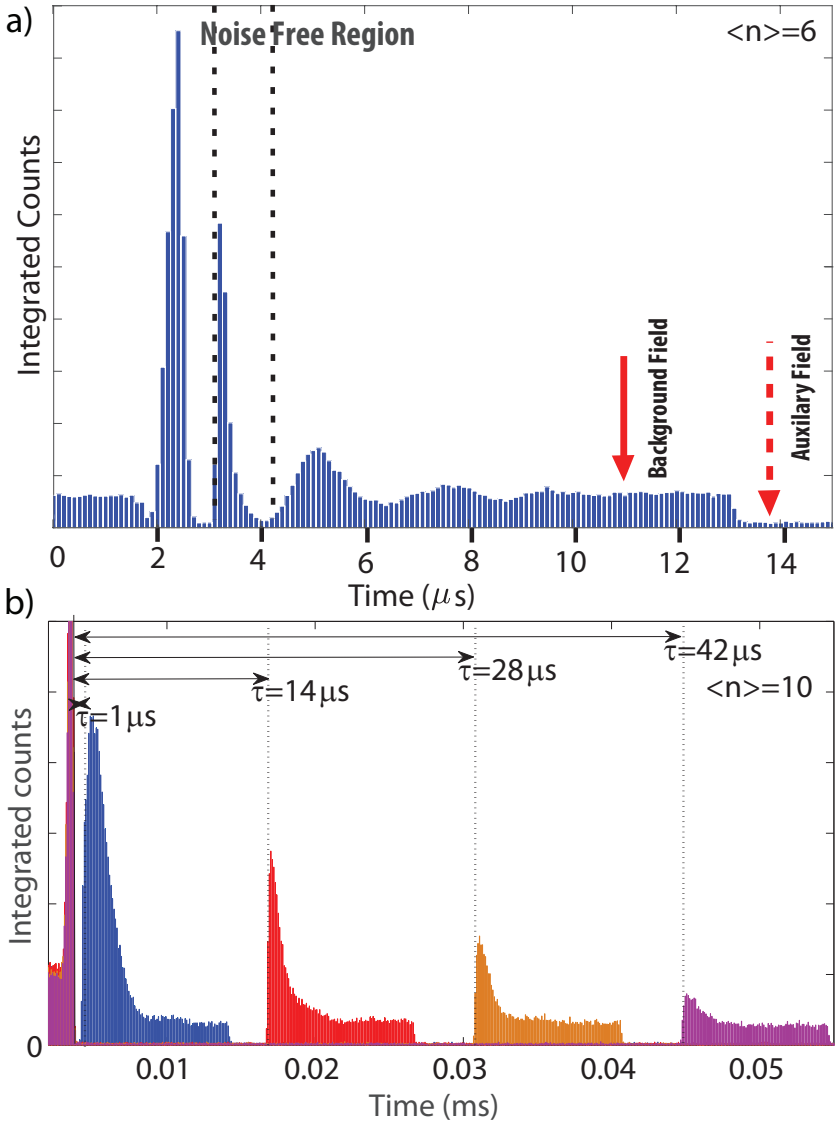


Figure 2.8: (a) Single rail storage with SBR of about 6 where the histogram of photons counts shows the retrieved signal (dark blue bars) compared background counts (light blue bars), the original pulse is shown by the dotted black line. Inset: SBR vs. storage time (black dots) and experimental fit (redline). (b) storage efficiencies for six different input polarizations using the dual rail system.

# Chapter 3

# Quantum Simulation using Spinor Slow Light

In a cursory fashion, Quantum Simulation can be described as using a controlled quantum experiment to mimic and understand much more complex phenomena in nature. This concept is of utmost importance when all other analytical and numerical models fail to describe the system we wish to probe. In the last chapter we explained in detail how to use a DSP to map a photonic state on collective spin excitation. In this chapter we will build upon that understanding to create more complex states such as Tripod DSPs and Spinor Slow Light (SSL, as defined in the chapter). We then show that these SSLs follow the same dynamics as 1+1 dimensional relativistic particles and it is possible to introduce terms that mimic relativistic particles with variable mass or induce a sign change in the mass.

## 3.1 Quantum Simulation of Relativistic Dynamics at Room Temperature

Over the last decade, a variety of exotic physical phenomena have been realised in artificially created quantum systems near zero temperature [69], including ultra-cold atoms [70], trapped-ions [71] and superconducting qubits [72]. Photonic setups have also been used to emulate relativistic and topological models [73, 74]. An unexplored direction for analogue and quantum simulation, allowing for operation at room temperature conditions, is the use of atoms interfaced with light in the form of collective excitations (DSPs) [44]. DSPs have formed the basis of many quantum technology applications including quantum memories [47, 122] and quantum non-linear frequency converters [170]. In this chapter, as explained above, we use DSPs to experimentally demonstrate an analogue simulation of the Jackiw-Rebbi (JR) model, the celebrated first example where relativity met topology [76]. Our DSPs are created by storing light in Rb atoms prepared in a dual tripod configuration using counter propagating laser fields. We first show how to realise relativistic Dirac spinor dynamics, as initially suggested in [77], and then create a static soliton background field as required in the JR model, via a spatially varying atom-photon detuning. We observe signatures of JR's famous zero-energy mode using a temporal analysis of the retrieved light pulses.

DSP's are created by storing and manipulating light in atomic media using electromagnetically induced transparency (EIT) [78, 79, 44, 80]. In a DSP-based analogue simulator, the DSPs are made to follow the dynamics outlined

by a light-matter Hamiltonian, prepared by addressing specific atomic transitions using control light fields [81]. The simulation results are then obtained by measuring the output photon wave functions. Along these lines, a spinor-like object consisting of two DSPs has been experimentally implemented in a double tripod configuration [82].

Moreover DSP-based quantum simulators have been proposed to realise Dirac models [77], and interacting relativistic systems [83]. Among those, the JR model is of paramount relevance [76] as it predicts charge fractionalisation [84]. This important aspect has been addressed in proposals using optical lattice setups [85, 86]. Additionally, the JR model has gained further attention due to the topological nature [87, 88, 89, 90, 91, 92, 93, 94, 95] of its zero-energy solution [96, 97]. This protected mode can be understood as a precursor to topological insulators [98], a hotly pursued topic nowadays [99, 100]. Recently, a soliton following a similar model has been observed experimentally in a fermionic superfluid [101].

In this chapter we describe the experimental realisation of relativistic dynamics exhibiting topological aspects as originally conceived in the JR model [76]. We use a room temperature atomic vapour addressed by laser fields in an EIT dual tripod configuration in order to produce slow light Dirac spinor dynamics. We then tune the system to the JR regime by using a linear magnetic field gradient, inducing a kink profile in the corresponding mass term [102]. The topological aspects of this novel EIT light-matter JR system are explored by analyzing the time correlations between the retrieved spinor components.

The structure of this chapter is as follows: firstly, we review the basics of

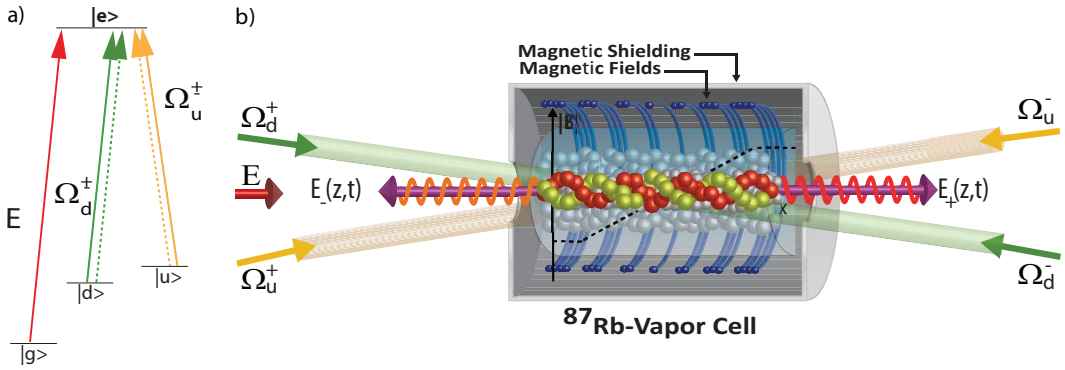


Figure 3.1: (a) The scheme used for creating an EIT tripod system (solid lines) and a dual tripod configuration (solid and dashed lines). (b) In order to experimentally create an EIT tripod system, an electric field $E(z,t)$ (red arrow) enters the medium, simultaneously with two strong co-propagating fields ($\Omega_d^+$ and $\Omega_u^+$). For the creation of the dual tripod configuration, the original field $E(z,t)$ is converted into two counter-propagating fields ($E_-(z,t)$ and $E_+(z,t)$) by introducing two pairs of counter-propagating control fields ($\Omega_d^+$, $\Omega_u^+$, $\Omega_d^-$ and $\Omega_u^-$). $m_{eff}(z)$ in the JR model is created using a spatially varying magnetic field gradient (dashed black lines).

coherent light propagation in a dual tripod EIT system. We then show the necessary conditions to connect this framework to Dirac and JR dynamics. Lastly, we present the experimental road map to prepare, evolve and benchmark this EIT light-matter JR system in a room temperature atomic interface.

## 3.2 Theoretical Background

### 3.2.1 Tripod DSP Dynamics

Here we describe the physical mechanisms underlying the creation of Tripod DSPs. Figure 3.1a depicts the atomic scheme used for creating these dynamics. We start the description of an atomic tripod by using the linearity of Hamilto-

nians and writing the light-matter interaction terms in the form $V = V_d + V_u$, with each component defined as:

$$V_d = \int (\hbar\Omega_\varepsilon \sigma_{eg} + \hbar\Omega_d \sigma_{de}) \frac{dz}{L} + H.C. \tag{3.1}$$

$$V_u = \int (\hbar\Omega_\varepsilon \sigma_{eg} + \hbar\Omega_u \sigma_{ue}) \frac{dz}{L} + H.C. \tag{3.2}$$

with L being the ensemble length, the $\sigma$'s are the atomic operators for the atomic coherences and the $\Omega$'s the coupling Rabi frequency for each transition (see Fig. 3.1 for the level definition in the atomic configuration). Furthermore, the Maxwell-Bloch equation describing the propagation of the input field in the medium follows:

$$(\partial_t + c\partial_z) E(z,t) = iN\Omega_\varepsilon \sigma_{ge}(z,t) \tag{3.3}$$

with $E = \varepsilon e^{i\omega_{ge} t - ikz}$ describing the initial input light field. In order to solve this equation for all terms we require another equation that relates the fields and the atomic operators. This is provided by the Heisenberg-Langevin equation for $V$. For $V_1$ we can write two relevant equations:

$$N\partial_t \sigma_{gd} = -iN\delta\sigma_{gd} + iN\Omega_d \sigma_{ge} \tag{3.4}$$

$$N\partial_t\sigma_{ge} = iN\Omega_\varepsilon E + iN\Omega_d\sigma_{gd} \tag{3.5}$$

We do not include the terms describing the effects of one-photon-detuning, decay and noise as they do not alter the general form of the propagation equation significantly in the time scale we are interested in. The only term of relevance is the two-photon detuning. As you will see in the next section, in our experimental implementation the applied magnetic field controls the tripod's two-photon detuning. Doing so results in opposite two-photon detunings for $V_d$ (negative) and $V_u$ (positive).

Following [44], we write: $\sigma_{ge} = \frac{1}{i\Omega_d}(\partial_t + i\delta)\sigma_{gd}$ and $\sigma_{gd} = -\frac{\Omega_\varepsilon}{\Omega_d}E$, and then substitute these terms into the Maxwell-Bloch equation, leading to:

$$(\partial_t + c\partial_z)E(z,t) = \frac{\Omega_\varepsilon}{\Omega_d}N(\partial_t - i\delta)\sigma_{gd} = \frac{\Omega_\varepsilon^2}{\Omega_d^2}N(-\partial_t - i\delta)E(z,t) \tag{3.6}$$

$$(\partial_t + v_g\partial_z)E(z,t) = -i\frac{\Omega_\varepsilon^2}{\Omega_d^2}N\delta E(z,t) \tag{3.7}$$

Here we define $v_g = \frac{c}{1+\frac{\Omega_\varepsilon^2}{\Omega_d^2}N}$ as the group velocity of the input field in the atomic medium. The resultant inhomogeneous equation can be re-written by redefining the frequency and the group velocity of the $E_d$ field as $\omega_d = \omega_{ge} - \frac{\Omega_\varepsilon^2}{\Omega_d^2}N\delta$ and $v_{gd} = v_g(1 - \frac{\Omega_\varepsilon^2}{\Omega_d^2}N\frac{\delta}{\omega_{ge}})$. This results in a shape-preserving equation in which the frequency of the E field inside the medium is acted

upon by the two-photon detuning, which in our case is controlled with the magnetic field. This works as long as the detuning is within the EIT bandwidth.

If we rewrite the Maxwell-Bloch equation for $\sigma_{gd}$ instead of E, we can obtain a similar equation to the one outlined above. The most general solution to this new equation is a superposition of E(z,t) and $\sigma_{gd}(z,t)$, the so-called Dark-state Polariton:

$$\Psi_d(z,t) = \cos\theta E_d(z,t) - \sin\theta\sigma_{gd}(z,t) \tag{3.8}$$

Following the same procedure for $V_u$, we arrive at a second DSP described as:

$$\Psi_u(z,t) = \cos\varphi E_u(z,t) - \sin\varphi\sigma_{gu}(z,t) \tag{3.9}$$

In which $E_u$ now has a frequency $\omega_u = \omega_{ge} + \frac{\Omega_\varepsilon^2}{\Omega_d^2}N\delta$, also induced by the magnetic field. Overall, the Tripod DSP dynamics is described by a linear combination of the two DSP's,

$$\Psi_T = \alpha\Psi_d + \beta\Psi_u \tag{3.10}$$

### 3.2.2 Dirac dynamics using Spinor Slow Light.

In this section, we study the dynamics of spinor slow light by coupling two counter-propagating Tripod DSP configurations. In our experiment this is done by adding counter-propagating control fields to the original tripod con-

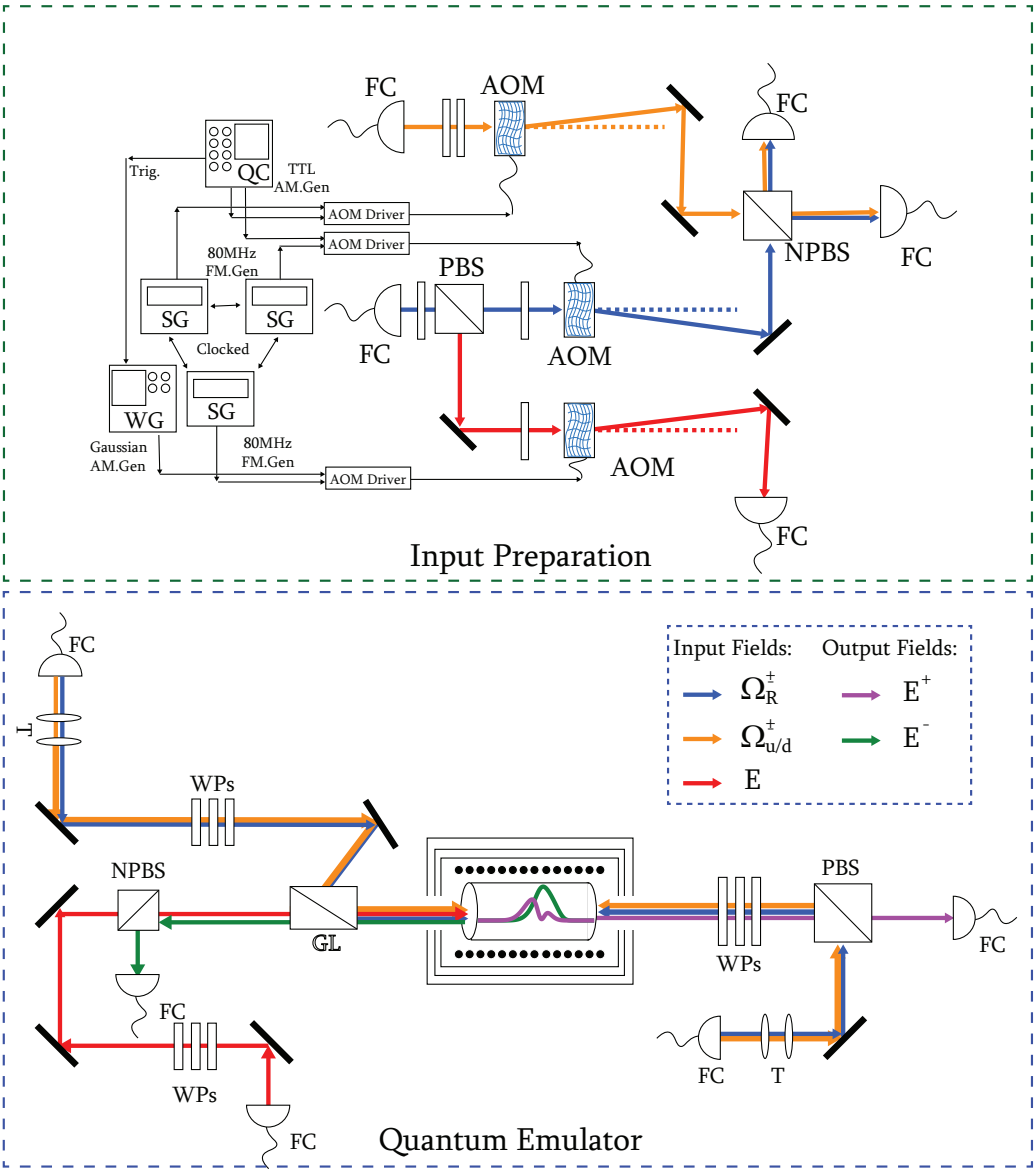


Figure 3.2: A blue print of the experimental setup, showing how to split and mix the light of two separate phase locked diode lasers to obtain all the necessary fields for creating SSLs.

figuration analyzed in the previous section. In this coupled case, it is more convenient to write the governing equations in matrix form. For the counter-propagating fields $E_{\pm} = \varepsilon e^{i\omega_{ge}t \mp ikz}$, the Maxwell-Bloch equation acquires the form:

$$(\partial_t - c\sigma_z\partial_z) \begin{pmatrix} E_+(z,t) \\ E_-(z,t) \end{pmatrix} = iN\Omega_\varepsilon \begin{pmatrix} \sigma_{ge+}(z,t) \\ \sigma_{ge-}(z,t) \end{pmatrix} \tag{3.11}$$

The two terms in this equation linking the atomic and photonic operators can be written as:

$$N\partial_t \begin{pmatrix} \sigma_{gd} \\ \sigma_{gu} \end{pmatrix} = -iN\sigma_z\delta \begin{pmatrix} \sigma_{gd} \\ \sigma_{gu} \end{pmatrix} + iN\mathbf{\Omega} \begin{pmatrix} \sigma_{ge+}(z,t) \\ \sigma_{ge-}(z,t) \end{pmatrix} \tag{3.12}$$

$$N\partial_t \begin{pmatrix} \sigma_{ge+}(z,t) \\ \sigma_{ge-}(z,t) \end{pmatrix} = +iN\Omega_\varepsilon \begin{pmatrix} E_+(z,t) \\ E_-(z,t) \end{pmatrix} + iN\mathbf{\Omega}^\dagger \begin{pmatrix} \sigma_{gd} \\ \sigma_{gu} \end{pmatrix} \tag{3.13}$$

Where we have defined the 2x2 Rabi frequency matrix as $\mathbf{\Omega} = \begin{pmatrix} \Omega_{d+} & \Omega_{u+} \\ \Omega_{d-} & \Omega_{u-} \end{pmatrix}$. Here we remark that a necessary condition to create a coupled system is that this matrix have a non-zero determinant. Else, these equations will describe two degenerate but decoupled Lambda systems. Following the analysis in the

previous section we write:

$$\begin{pmatrix} \sigma_{ge+}(z,t) \\ \sigma_{ge-}(z,t) \end{pmatrix} = \frac{1}{i\mathbf{\Omega^{-1}}}(\partial_t + i\sigma_z\delta) \begin{pmatrix} \sigma_{gd} \\ \sigma_{gu} \end{pmatrix} \tag{3.14}$$

and

$$\begin{pmatrix} \sigma_{gd} \\ \sigma_{gu} \end{pmatrix} = -\frac{\Omega_\varepsilon}{\mathbf{\Omega^{-1}}} \begin{pmatrix} E_+(z,t) \\ E_-(z,t) \end{pmatrix} \tag{3.15}$$

which lead to:

$$(\partial_t - v_g\sigma_z\partial_z) \begin{pmatrix} E_+(z,t) \\ E_-(z,t) \end{pmatrix} = i\frac{\Omega_\varepsilon^2}{\mathbf{\Omega^{-2}}}N\sigma_z\delta \begin{pmatrix} E_+(z,t) \\ E_-(z,t) \end{pmatrix} \tag{3.16}$$

In the latter equation each Rabi frequency can be written as $\Omega_i = \Omega e^{i(\theta_i+\theta_{Bi})}$, assuming control fields with similar intensities. Here $\theta_{Bi} = \frac{1}{\hbar}g_i\mu_B B\tau$ describes the overall effect of the applied magnetic field on the phase of each coupling, with $g_i$ being the g factor for each addressed Zeeman state and $\tau$ is the storage time before double-tripod retrieval.

Defining a total phase relation between all Rabi frequencies as $\Phi = (\theta_{d+} - \theta_{u+}) - (\theta_{d-} - \theta_{u-})$, it is possible to show that the aforementioned $\Omega$ matrix only has an inverse in the case of $\Phi \neq 0$. In this case $E_+$ and $E_-$ are coupled together and maximum coupling is achieved for $\Phi = \pi$.

Due to the symmetry of our configuration, the only interesting phase combina-

tion is such as to have two of the fields with a $\pi/2$ phase difference, or in terms of the Rabi frequency matrix, having the case $\mathbf{\Omega} = \Omega \begin{pmatrix} 1 & i \\ i & 1 \end{pmatrix} = \Omega(1 + i\sigma_x)$. Using this assumption the propagation equation can be re-written as:

$$i\hbar(\partial_t - v_g\sigma_z\partial_z) \begin{pmatrix} E_+(z,t) \\ E_-(z,t) \end{pmatrix} = \hbar\frac{\Omega_\varepsilon^2}{2\Omega^2} N\sigma_y\delta \begin{pmatrix} E_+(z,t) \\ E_-(z,t) \end{pmatrix} \tag{3.17}$$

It is possible to derive a similar equation for the atomic operators $\sigma^\pm(z,t) = \frac{1}{\sqrt{2}}(\sigma_{gu} \pm i\sigma_{gd})$, thus constructing an equation for spinor of slow light (SSL) object $\mathbf{\Psi} = \binom{\Psi^+}{\Psi^-}$ as:

$$i\hbar\partial_t\mathbf{\Psi} = \left(i\hbar v_g\sigma_z\partial_z + m_{eff_0}v_g^2\sigma_y\right)\mathbf{\Psi} \tag{3.18}$$

with $\Psi^\pm(z,t) = \cos\theta E^\pm(z,t) - \sin\theta\sigma^\pm(z,t)$ and $\theta = \arctan(\sqrt{\frac{g^2N}{\Omega^2}})$ [77]. Equation 3.18 resembles a 1+1 Dirac equation and describes the evolution of two coupled SSL components with an effective mass $m_{eff_0} = \hbar\frac{\delta}{2}\frac{1}{v_g^2}\sin^2(\theta)$ and $\alpha = \sigma_z$, $\beta = \sigma_y$.

We emphasize that the Dirac model has a unique position in the history of theoretical physics, as it always considered a bridge between quantum mechanics and relativistic physics, while also having a quantum optics analog in the Jaynes-Cummings model. Additionally, the solutions to this Hamiltonian mimic the behavior of Majorana particles in different condensed matter systems.

### 3.2.3 JR model

As we discussed so far, the Dirac equation in 1+1 dimension reads

$$i\partial_t \mathbf{\Psi} = -ic\alpha\partial_z \mathbf{\Psi} + \beta mc^2 \mathbf{\Psi} \tag{3.19}$$

in which $c$ is the speed of light, $\alpha^2 = \beta^2 = 1$ and $[\alpha, \beta] = 0$ holds. One possible choice is $\alpha = -\sigma_z$ and $\beta = \sigma_y$ in terms of the usual Pauli matrices, which means that the wavefunctions $\mathbf{\Psi}$ are 2 component objects in 1+1 dimension. Following Jackiw and Rebbi [76] let us replace the mass with a position dependent field:

$$i\partial_t \mathbf{\Psi} = -ic\alpha\partial_z + \beta c^2 \phi(z) \mathbf{\Psi}. \tag{3.20}$$

Noting that the sign of the mass can be changed, they considered a kink solution that interpolates between the negative and positive signs. Choosing $\phi(x) = \tanh(\lambda z)$, one sees that the solution

$$\mathbf{\Psi}_{zero}(z) = \exp\left(-c\int^z dz' \phi(z')\right)\chi = \exp\left[-c\ln\left(\cosh\lambda z\right)\right]\chi \tag{3.21}$$

with $\alpha\beta\chi = -i\chi$ is a zero-energy solution localized around $z = 0$. For our choice of $\alpha$ and $\beta$, $\chi \propto (1, -1)$ and we will denote the spatial part with $\phi(z)$ such that

$$\mathbf{\Psi}_{zero}(z) \equiv \psi_{zero}(z)(1, -1). \tag{3.22}$$

The presence of the zero-mode was shown to be robust against the detailed form of the kink due to its topological nature. What is important is the topology of the kink: it goes from negative to positive (or vice versa).

## 3.3 Experimental Simulation of Relativistic Systems

## 3.4 Experimental Realization.

### 3.4.1 Creation of tripod DSP.

In the previous section we went over the theoretical construction of SSLs and how they related to models such as Dirac and JR. During the rest of this chapter we will talk about the experimental realization of such a quantum simulator. We create the tripod DSP $\Psi_T$ in an atomic ensemble using EIT in the following way. Firstly, three separated EIT systems are created by breaking the degeneracy of the Rb atoms Zeeman sub-levels through applying a DC magnetic field B (see Fig. 3.4). Secondly, we isolate two of the EIT systems by using a single control laser that is symmetrically detuned ($\pm\delta/2 = \pm g_d \mu_B B/2$) from the transitions $|u\rangle \rightarrow |e\rangle$ and $|d\rangle \rightarrow |e\rangle$, effectively forming two control fields $\Omega_u$ and $\Omega_d$ (see Fig. 3.2b). Lastly, we send a pulse of light ($E(z,t)$) undergoing tripod DSP dynamics due to $\Omega_u$ and $\Omega_d$, thus creating the components of $\Psi_T$ ($\Psi_u$ and $\Psi_d$).

All the transitions used in the experiment are within the $^{87}$Rb $D_1$ line. The

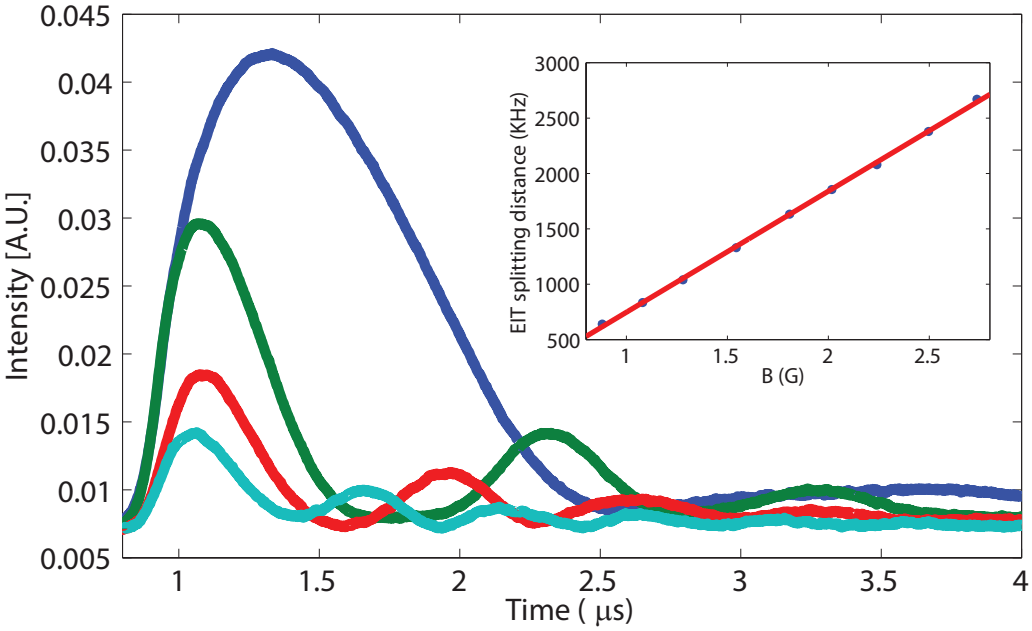


Figure 3.3: **Tripod DSP demonstration.** Forward propagating output of the tripod configuration after 2 micro seconds storage time. The results are plotted for different applied magnetic fields. The retrieved pulses correspond to magnetic-field-induced beat notes between the spinor components of 400kHz (blue), 875kHz (green), 1300kHz (red) and 1750 kHz (light blue). The inset shows the relation between the applied magnetic field and the EIT two-photon detuning. The ratio is measured to be 1.09 MHz/Gauss.

storage is based on EIT in warm $^{87}$Rb vapor. The probe is stabilized using top-of-fringe locking to saturation spectroscopy of a Rb vapor cell and the control field is phase-locked to the probe field as was explained in chapter 2. The probe pulses $E(z,t)$ with a width of 400 $\mu$s are tuned to $5S_{1/2}|F, m_F = 1, 0\rangle \rightarrow 5P_{1/2}|F', m_{F'} = 1, 0\rangle$ ($|g\rangle \rightarrow |e\rangle$) (with detuning $\Delta = 250MHz$). The writing control fields ($\Omega_u$ and $\Omega_d$) are tuned at $|F, m_F = 2, 0\rangle \rightarrow |F', m_{F'} = 1, 0\rangle$ ($|u\rangle \rightarrow |e\rangle$ with detuning $-\delta/2$) and $|F, m_F = 2, -1\rangle \rightarrow |F', m_{F'} = 1, 0\rangle$ ($|d\rangle \rightarrow |e\rangle$ with detuning $+\delta/2$)(see Fig. 3.2 and 3.4a). The EIT lines have an average FWHM of 1.2 MHz [103]. A constant magnetic field induces the two-photon detuning with a $\delta/B$ ratio of 1.09 MHz/G.

The time sequence of the creation of $\Psi_T$ and the readout of $\Psi_T^{'}$ is shown in fig. 3.4d. $\Psi_T$ is stored for $2\mu s$ after which it is mapped onto $E_d^{'}$ and $E_u^{'}$ using $\Omega_R$. $\Omega_R$ is tuned to $|F, m_F = 1, 0\rangle \rightarrow |F', m_{F'} = 1, 0\rangle$ ($|g\rangle \rightarrow |e\rangle$). We calibrate the coherence of this tripod scheme by storing $\Psi_T$ and retrieving it using a co-propagating control field ($\Omega_R$) coupled to the $|g\rangle \rightarrow |e\rangle$ transition. Polarization elements supply 42 dB of control field attenuation (80% probe transmission). The retrieved tripod DSP ($\Psi_T^{'}$) has two components, $\Psi_u^{'}$ and $\Psi_d^{'}$ with a frequency difference $\delta = \omega_{ue} - \omega_{de}$. In Figure 3.3 we observe this frequency difference. The presence of a magnetic-field controlled beat note is a testament to the creation of the two DSP in an interacting spinor configuration. We find a suitable $\delta$ by choosing a magnetic field B that maximizes the beat note in the retrieved mode. Here we mention that breaking the degeneracy of the Zeeman states with a magnetic field is in principle not necessary, yet we have used this method to facilitate the detection of the beat note between the

two optical components of the tripod after retrieval.

### 3.4.2 Measurement of 1+1 Dirac Dynamics.

Once suitable atom-light detunings are chosen, we proceed to create the SSL $\mathbf{\Psi}$. We use two control fields ($\Omega_u^+$ and $\Omega_d^+$) co-propagating with the probe $E(z,t)$ and two additional counter-propagating control fields $\Omega_u^-$ and $\Omega_d^-$ (see Fig. 3.2 and 3.4a). The created SSL components $\Psi^{\pm}$ are then stored. During storage, the temporal interaction of $\Psi^+$ and $\Psi^-$ follows the Dirac dynamics outlined by equation 3.18. After storage, these dynamics are mapped onto the SSL components $\Psi'^{\pm}$ by applying the counter-propagating control fields $\Omega_R^+$ and $\Omega_R^-$ (see Fig. 3.4b). We detect the optical form of $\Psi'^{\pm}$ ($E'^{\pm}(z,t)$) simultaneously in independent photo-detectors.

We vary the storage time for fixed two-photon detuning, thus changing the interaction time between the SSL components. Each pair of correlated experimental points is obtained by measuring the respective storage of light signals, integrating its total energy for varying storage time. We observe coupled oscillations for the intensities retrieved in each direction, $|E'^{+}(z,t)|^2$ (blue dots) and $|E'^{-}(z,t)|^2$ (red dots) in Fig 3.5, as expected from the usual Dirac dynamics coupling the two components of the spinor. Most importantly, the frequency of the oscillation is changed by varying the two-photon detuning, which illustrates to the coherent nature of the process (see Fig. 3.5a and 3.5b). We note that similar oscillations between SSL frequency components have been shown in previous studies [82]. However, in our implementation the two spinor components correspond to different propagation directions, which

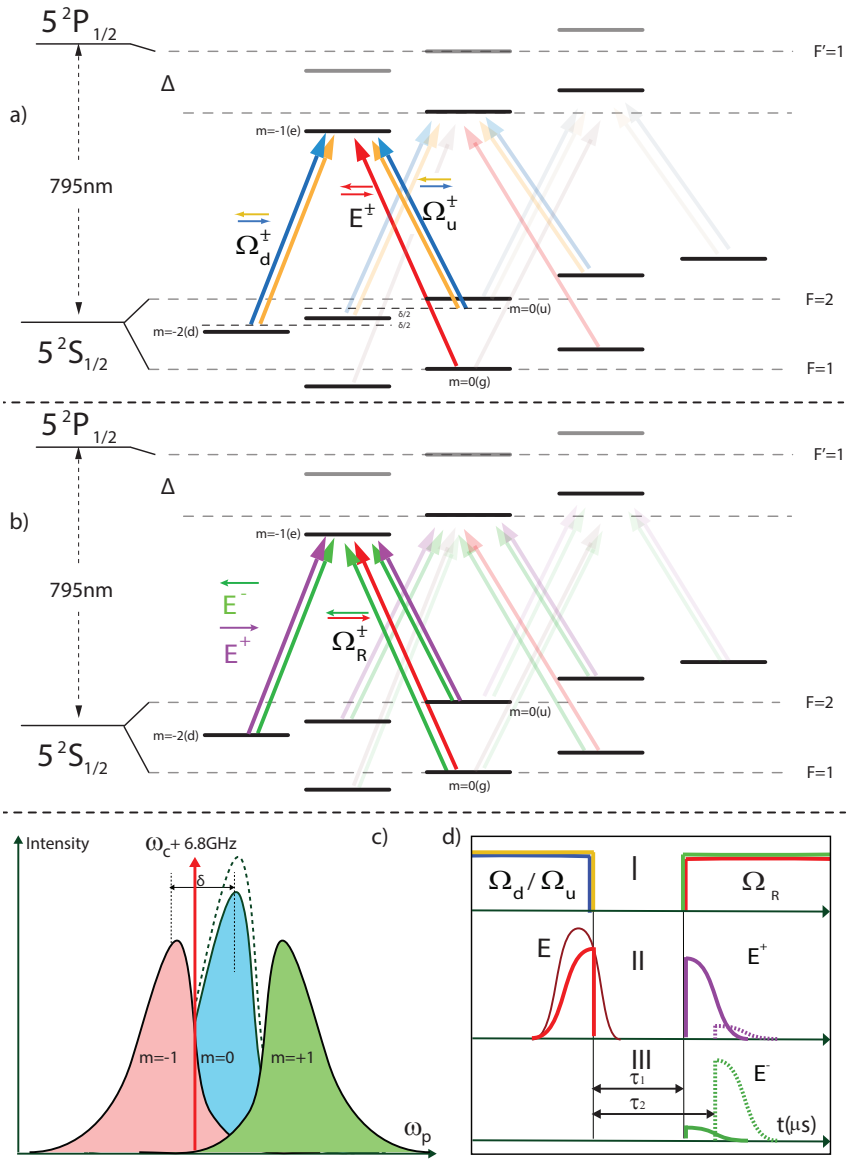


Figure 3.4: **SSL setup.** (a) The SSL $\mathbf{\Psi}$ is created using $\Omega_u^{\pm}$ and $\Omega_d^{\pm}$. The two-photon detuning is chosen to minimize the effect of other possible tripod configurations (faded solid lines) (b) $\mathbf{\Psi}$ is stored for a time $\tau$ after which it is mapped onto $E^{\pm'}$ using $\Omega_R^{\pm}$ (c) An original EIT line (dashed black line) is separated into three lines via applying a magnetic field B. Placing the control laser with a proper two-photon detuning ($\pm\delta/2$ from Zeeman states m=0 and m=-1) creates two isolated EIT systems. (d) Pulsing sequence for the creation of dual-tripod dynamics.

is the key design element for engineering Dirac dynamics.

We benchmarked the aforementioned results against numerical solutions (performed by our collaborators) of the 1+1 dimensional Dirac equation of the form (including a coherence decay rate $\gamma$ to account for losses in the real experiment):

$$i\partial_t \mathbf{\Psi} = \left(iv_g\sigma_z\partial_z + m_{eff_0}v_g^2\sigma_y - \gamma\right)\mathbf{\Psi}, \tag{3.23}$$

with the initial condition $\mathbf{\Psi_0} = (\Psi_0^+, \Psi_0^-)$ extracted from the shape of the original SSL right after storage. The solid lines in Fig. 3.5a and 3.5b represent the numerical simulation with fixed $v_g = 1.0cm/\mu s$, $m_{eff_0}v_g^2 = 3.3 * \delta$ and $\gamma = 0.3$.

As storage time is increased, the SSL components lose their mutual coherence and thus the experimental data begins to deviate from the theoretical prediction. Nonetheless, these measurements provide strong evidence that the SSL dynamics follows that of relativistic particles.

### 3.4.3 Relativistic dynamics with topological behavior.

Having built an analog Dirac simulator, we now move to mimic JR's topological predictions. In order to engineer $m_{eff}(z)$, we use a spatially varying magnetic field changing the two-photon detuning along the propagation axis of the light. In the original proposal, the bosonic field varies from a negative value to a positive value following the hyberbolic tangent function [76]. Due to its topological nature however, other profiles exhibiting similar behaviour at the

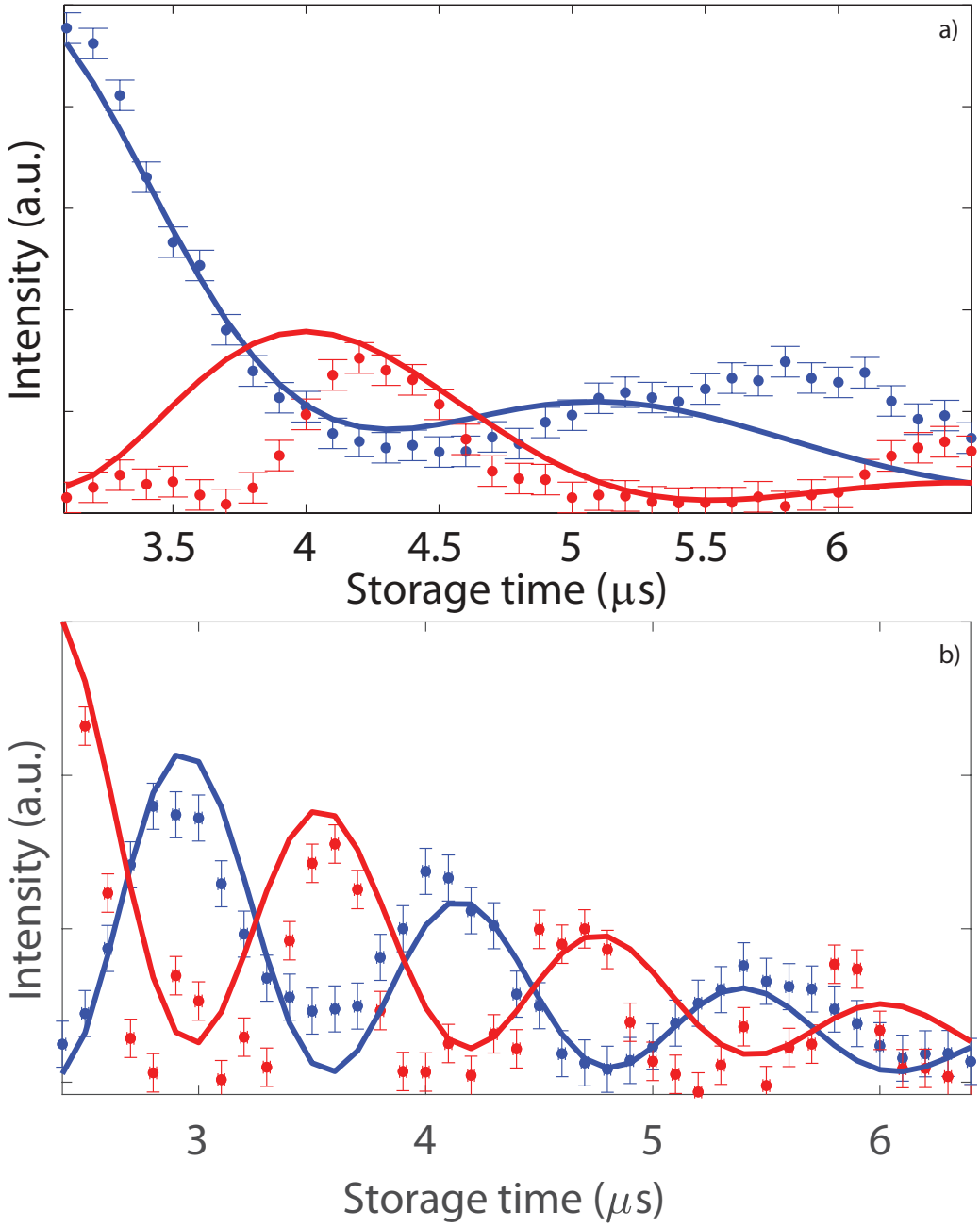


Figure 3.5: **Dirac dynamics using SSL.** Evaluating $|E^{\pm'}|^2$ for each $\tau$ results in an out of phase oscillation between the forward (blue dots) and backward (red dots) components of the SSLs. We plot the experimental data for $\delta =$ 350kHz (c) and 700kHz (d). Solid lines in (c) and (d) corresponds to numerical solutions of the SSL Dirac equation (eq. 2).

boundary work too, as discussed in detail in [102]. In this work, we choose a linearly-varying magnetic field, $B(z) = B_0 z$, and perform experiments akin to our previous section. Figure 3.6a shows the obtained results. We observe the suppression of the coupled oscillation dynamics of the bare Dirac model by increasing the strength of the gradient, as predicted in [76, 102].

We again benchmarked this result against a numerical solution of the Jackiw-Rebbi equation. The procedure is similar to the one presented in the previous section, reconstructing the initial SSL components $\mathbf{\Psi_0} = (\Psi_0^+, \Psi_0^-)$ (red and blue solid line in fig. 3.6b) and using $\gamma = \begin{pmatrix} \gamma_1 & 0 \\ 0 & \gamma_2 \end{pmatrix}$ and $m_{eff}(z)v_g^2 \propto \delta = (0.745\frac{MHz}{cm}(z - 2.5cm) + 0.35MHz)$. In general each of the wave-functions can be written as $\psi^{\pm}(x) = e^{i\Phi^{\pm}(x)}|\psi^{\pm}(x)|$. Assuming $|\Phi^{\pm}(x)|$ to be constant, we define a global phase between the SSL components that is represented as $\Phi$ (a free parameter in the numerical fit). The numerical solutions ($\int dz|\Psi^+(z)|^2$ and $\int dz|\Psi^-(z)|^2$) are obtained numerically by fixing the group velocity, effective mass and loss rate to experimental estimations. The free parameters $\Phi$ and initial relative intensity are then fitted to the data. The solid lines in Fig. 3.6a (red and blue) represent the numerical solution with $\Phi = \pi$.

To probe the creation of the predicted JR zero energy mode, we first construct $\phi(z)$ (see Fig. 3.6b, green line) using the effective mass provided by the magnetic field gradient (purple line in Fig. 3.6b). We then calculate the overlap of the experimentally extracted $\mathbf{\Psi_0} = (\Psi_0^+, \Psi_0^-)$ (red and blue lines in Fig. 3.6b, measured at 1.5 $\mu s$ storage time) with the zero-mode spinor: $\int dz \mathbf{\Psi_0^\dagger} \psi_{zero}$. In Fig. 3.6c, we plot this overlap for different values of the

global phase between the SSL components, $\Phi$. Noticeably, the best overlap of $\sim 80\%$ is also obtained for $\Phi = \pi$, which strongly hints that $\mathbf{\Psi_0}$ was prepared in the zero-mode.

In our experimental results, we have two decay rates for $\Psi^{+'}$ and $\Psi^{-'}$ as they couple to a magnetic field insensitive and a magnetic field sensitive EIT line, respectively (see Fig. 3.4c). Our interpretation of the high initial overlap at 1.5 $\mu s$ storage time is that we have created a zero-energy mode within the medium during this initial time interval.

## 3.5 Summary

In this chapter we demonstrated the experimental realization of a controllable coupling between two counter-propagating SSL components, simulating the dynamics of a relativistic massive fermion in a 1+1 Dirac equation. By adding a static background bosonic field (via the use of a magnetic field gradient), we have also simulated the celebrated Jackiw-Rebbi model. We have benchmarked our work with theoretical simulations by carefully reconstructing the initial SSL wave functions and using them in a numerical solution of the corresponding Dirac and JR differential equations. These values are then compared with the experimental data achieved by varying the storage time, showing a very good correlation within the coherence time of the atoms. Lastly, we have also measured signatures of the JR zero-mode by observing the inhibition of the oscillation between the spinor components as predicted in the theory.

This experiment is an important first step towards more complex quantum

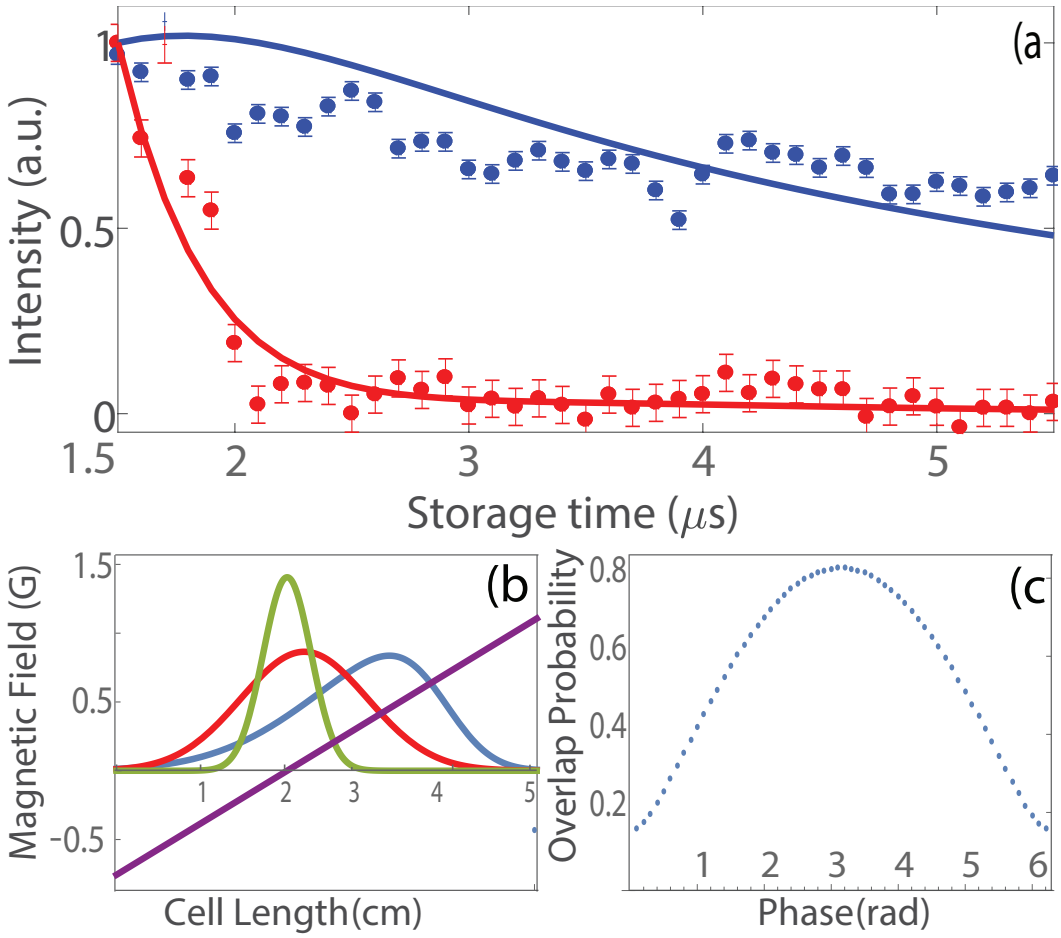


Figure 3.6: **JR dynamics using SSL**. (a) Evaluating $|E^{\pm'}|^2$ for each $\tau$ shows a suppression of the oscillation between $E^{+'}$ (blue dots) and $E^{-'}$ (red dots) as predicted by the JR seen in Fig. 3.5c. Full oscillation suppression is obtained for a gradient of 435 mG/cm. (b) The spatial location of initial SSL components $\Psi_0^+$ (blue) and $\Psi_0^-$ (red) together with $\phi(z)$ (green) in the cell. Magnetic gradient (purple). (c) $\int dz \mathbf{\Psi_0^\dagger} \psi_{zero}$ as a function of the phase between $\Psi^{+'}$ and $\Psi^{-'}$.

simulations with many quantum relativistic particles. Possible extensions include the study of the Klein paradox [104] or the MIT bag model [105] by using coupled light-matter SSLs. Moreover, as slow light polaritons can be made to interact strongly, our work provides a pathway towards analog simulators of complex phenomena described by interacting quantum field theories. Possibilities include the simulation of: charge fractionalisation in bosons [106], the interacting random Dirac model [107] and the renormalization of mass due to interacting fermions [108]. Furthermore, interacting relativistic models such as the famous Thirring model [109] are now within experimental reach. As many of these important QFT predictions are only addressable using high energy experiments, this new breed of light-matter room temperature simulators will be an exciting tool to reach unexplored realms of physics.

# Chapter 4

# Network of Quantum Devices

The focus of previous chapters was on the design of individual quantum nodes, capable of coherently manipulating the qubits at room temperature. Quantum memories and simulators are the key elements of a scalable quantum processing network. Alongside these nodes, our lab has successfully demonstrated a photon-photon cross-phase modulator at room temperature for on average single photon pulses using the same light-matter platform. We have also taken the first steps in realizing high efficiency quantum frequency converters. In the final chapter we will briefly discuss these nodes and their importance for a scalable quantum system.

As we discussed in the first chapter, in order to develop a scalable network of quantum devices, having several high fidelity quantum nodes is a necessary but not a sufficient condition. For the scalability of the network not only does each node need to perform with high efficiency and minimum loss, but also the interconnectivity between these quantum nodes is required to be as efficient as

possible, preventing an exponential qubit loss as the network scales up. The quantum nodes of our room temperature platform have two very unique properties which make them prime candidates for a scalable processing network: I. They all work at room temperature and are relatively easy and low cost to miniaturize and employ outside laboratory space and II. They all operate based on the same physics (EIT) which should result in a maximum quantum impedance matching between the nodes.

In the following chapters, we will discuss and design networks of multiple light-matter interfaces and study the new properties that emerge in the network as a result. Since our quantum memories are on a more developed stage, all these experiments are focused on integrating these devices within quantum networks. In this chapter, we will discuss networks of two quantum memories in series and parallel. In the next chapter, we will integrate our quantum memory within known quantum cryptography networks such as BB84 and MDI-QKD and study the behavior of the memories upon receiving random strings of polarization qubits.

## 4.1 Cascading Quantum Memories

### 4.1.1 Introduction

Any machine can be defined as device composed of many constituents with their own specific functions which, when interfaced together, carry out a much greater task. This same description would hold true for a quantum information processor, a complex machine capable of operating and processing

quantum entities encoded with information. Given the recent success in the creation and control of individual quantum systems with a variety of physical architectures [50, 49], the next logical step towards the realization of such a quantum machine is the interconnection between multiple quantum interfaces [110, 111, 112, 113]. This type of functionality will be a prerequisite for networks in which quantum information and entanglement can be shared, either sequentially or simultaneously [114, 54, 115].

The success of these networks will rely on having universal quantum nodes producing outputs suited for driving (as inputs) further quantum nodes. This is the concept of quantum cascadability [116] and it is necessary in several implementations of quantum computer architectures and quantum communication protocols [117, 118, 119, 120]. In order for many of these protocols to come to fruition they will be reliant on operational quantum memories [121], and therefore the ability to cascade memory devices, i.e. driving a quantum memory with the output of another quantum memory is a desired characteristic on any future network.

Recently, the concept of cascading has been applied to the interconnection of quantum state sources and quantum memories [47, 122], but no experiment has been performed in which a third degree of connectivity has been explored by driving a second quantum memory with the output of a first. The experiments require an initial, high fidelity (with respect to the original input) quantum memory operation with the output also suited as an input for a second memory operation. After the second storage process, the output would still maintain a high fidelity with the original input; a requirement

ideally attained with high efficiency and low propagation losses. These are two restrictive conditions met by only a few systems that are capable of the compromise between efficiency and low noise to permit such interconnection. Considering this, a promising technology for the creation of cascadable devices is the use of room temperature atomic vapor memories [123, 14, 13], as they offer a relatively inexpensive experimental overhead while also having strong light matter interaction at the single photon level [124, 125, 27, 126].

In this chapter we discuss the cascaded storage of optical pulses containing a few photons on average in two room-temperature quantum light-matter interfaces. Our setup is derived from our recent results in which we have built a room temperature optical quantum memory for polarization qubits using a dual rail configuration [27, 126]. After the first storage of light procedure using one of the ensembles in the dual-rail setup, we retrieved the atomic excitation using a control field that has been temporally shaped in amplitude such that the shape of the retrieved pulse resembles the original input [123]. This retrieved probe pulse is then sent back to the ensemble in the other rail to serve as the input for a sequential storage.

### 4.1.2 Numerical Modeling of a Cascaded System

In order to achieve the cascading of quantum warm vapour light-matter interfaces, we use the technique of EIT) provided by a $\Lambda$ energy level scheme both storage procedures. The output of the first $\Lambda$-type atomic level structure, characterized by the interaction with two laser fields, $\Omega_{p1}$ (probe) and $\Omega_{c1}$ (control), with one-photon detunings $\Delta_1$ and $\Delta_2$ respectively (see Fig.

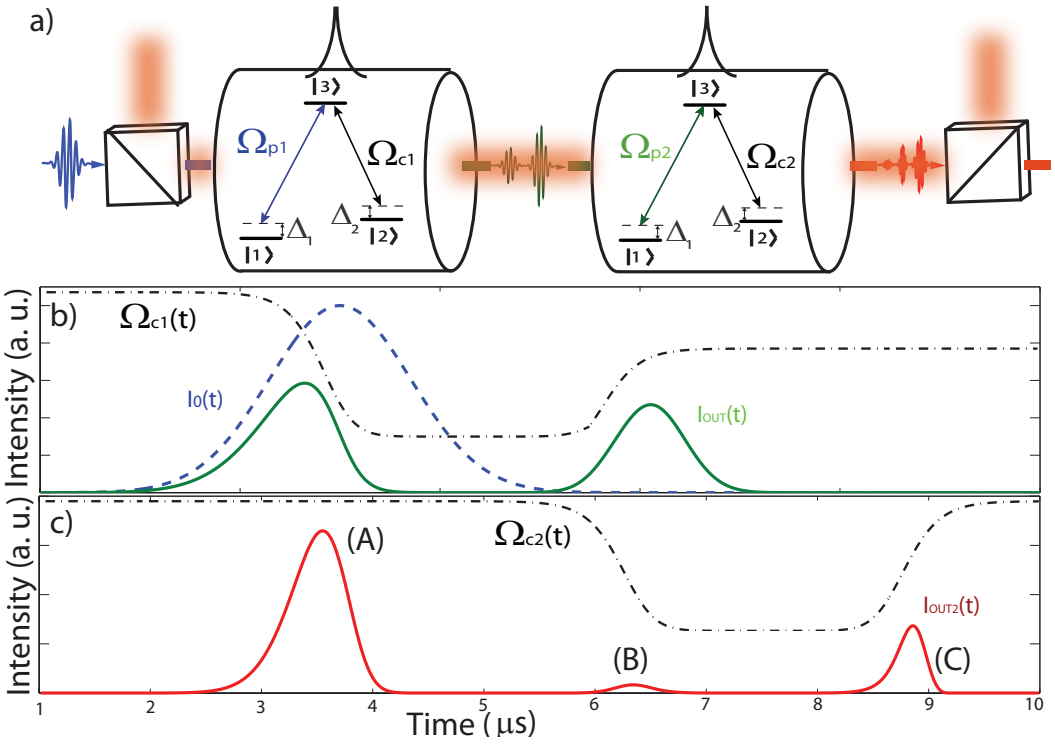


Figure 4.1: **Cascading of quantum light-matter interfaces.** (a) Concept of the cascading experiment. (b) Input pulse (blue dotted line), Control field 1 time sequence (black dotted line) and retrieved light signal (solid green line) as obtained by simulation. (c) Control 2 time sequence (dotted black lines) and cascaded retrieved signal (solid red line).

4.1), needs to function as the input of a second Λ-type atomic level structure, also characterized by the interaction with two laser fields, $\Omega_{p2}$ (retrieved probe coming from system 1) and $\Omega_{c2}$ (control). We assume the detunings to be the same as in the first system.

As explained in chapter 2, the process of storage of light in the first Λ-system can be understood using the time-independent Hamiltonian which de-

scribes the atom-field coupling in a rotating frame, given by:

$$\hat{H} = \Delta_1 \hat{\sigma}_{33} + (\Delta_1 - \Delta_2)\hat{\sigma}_{22} + \Omega_{p1} E_{p1}(z,t)\hat{\sigma}_{31} + \Omega_{c1}(t)\hat{\sigma}_{32} + h.c. \tag{4.1}$$

where $\hat{\sigma}_{ij} = |i\rangle\langle j|, i, j = 1, 2, 3$ are the atomic raising and lowering operators $i \neq j$, and atomic energy-level population operators $i = j$. Notice that in this chapter we return to the more common three level Hamiltonian. The dynamics of the first storage event can be obtained numerically by solving the master equation for the atom-light system density operator together with the Maxwell-Bloch equation that contains the impact of the atomic polarization on the electromagnetic field

$$\dot{\hat{\rho}} = -i[\hat{H}, \hat{\rho}] + \sum_{m=1,2} \Gamma_{3m}(2\hat{\sigma}_{m3}\rho\hat{\sigma}_{3m} - \hat{\sigma}_{33}\hat{\rho} - \hat{\rho}\hat{\sigma}_{33}) \tag{4.2}$$

$$\partial_z E_{p1}(z,t) = i\frac{\Omega_{p1} N}{c}\langle\hat{\sigma}_{31}(z,t)\rangle. \tag{4.3}$$

Here $\Gamma_{31}$ and $\Gamma_{32}$ are the polarization decay rates of the excited level $|3\rangle$ to the ground states $|1\rangle$ and $|2\rangle$ respectively, $c$ is the speed of light in vacuum and $N$ the number of atoms participating in the ensemble. Initial conditions provided by $\Omega_{C1}(t)$ and $E_p(0,t) = E_o(t)$ (the original probe pulse shape) allow us to solve this set of equations and make predictions about the retrieved pulse shape $E_{OUT}(t) = E_{p1}(L;t)$, where $L$ denotes the length of the atomic ensemble. Once we know $E_{OUT}(t)$ we can propagate this result as an input of another system akin to the one describe above and calculate $E_{OUT2}(t)$ corresponding to a pulse that has been stored in a cascading fashion in the two systems.

In Figure 4.1b, we plot the results of the first simulation, by using $\Omega_{c1}(t)$ (black dotted line in Fig. 4.1b) and $E_p(0,t) = E_o(t)$ (blue dotted line in Fig. 4.1b) as the control and probe inputs respectively . The results of our simulation for $E_{OUT}(t) = E_{p1}(L;t)$ are plotted in Figure 4.1b (see solid green line) and resemble the characteristic storage of light signal, presenting a probe leak signal (left peak) and the retrieved signal after storage (right peak). A second simulation is performed but now using $\Omega_{c2}(t)$ (dotted black line in Fig. 4.1c, notice the time delay with respect to $\Omega_{c1}(t)$ to account for the first storage) and $E_{OUT}(t)$ as the control and probe field inputs respectively. The results of the second simulation are presented in Fig. 4.1c (solid red line).

The resultant cascaded stored signal has three peaks (Fig. 4.1c), a slow down leakage coming from the first experiment (A, leftmost peak), a second small leakage created in the second memory (B, middle peak) and a third peak that corresponds to the timing in which the control field 2 is switch on again (C, right most peak). The final peak corresponds to a portion of the light field that has been successively stored twice in independent light matter interfaces and is the focus of this letter.

### 4.1.3 Experimental Impedance Matching of Two Atomic-based Memories in Series

In order to measure the aforementioned cascaded storage signal, we employed the same quantum storage configuration as was described in Chapter 2: two external-cavity diode lasers as light sources, phase-locked at 6.8 GHz are resonantly coupled to a $\Lambda$-configuration composed of two hyperfine ground states

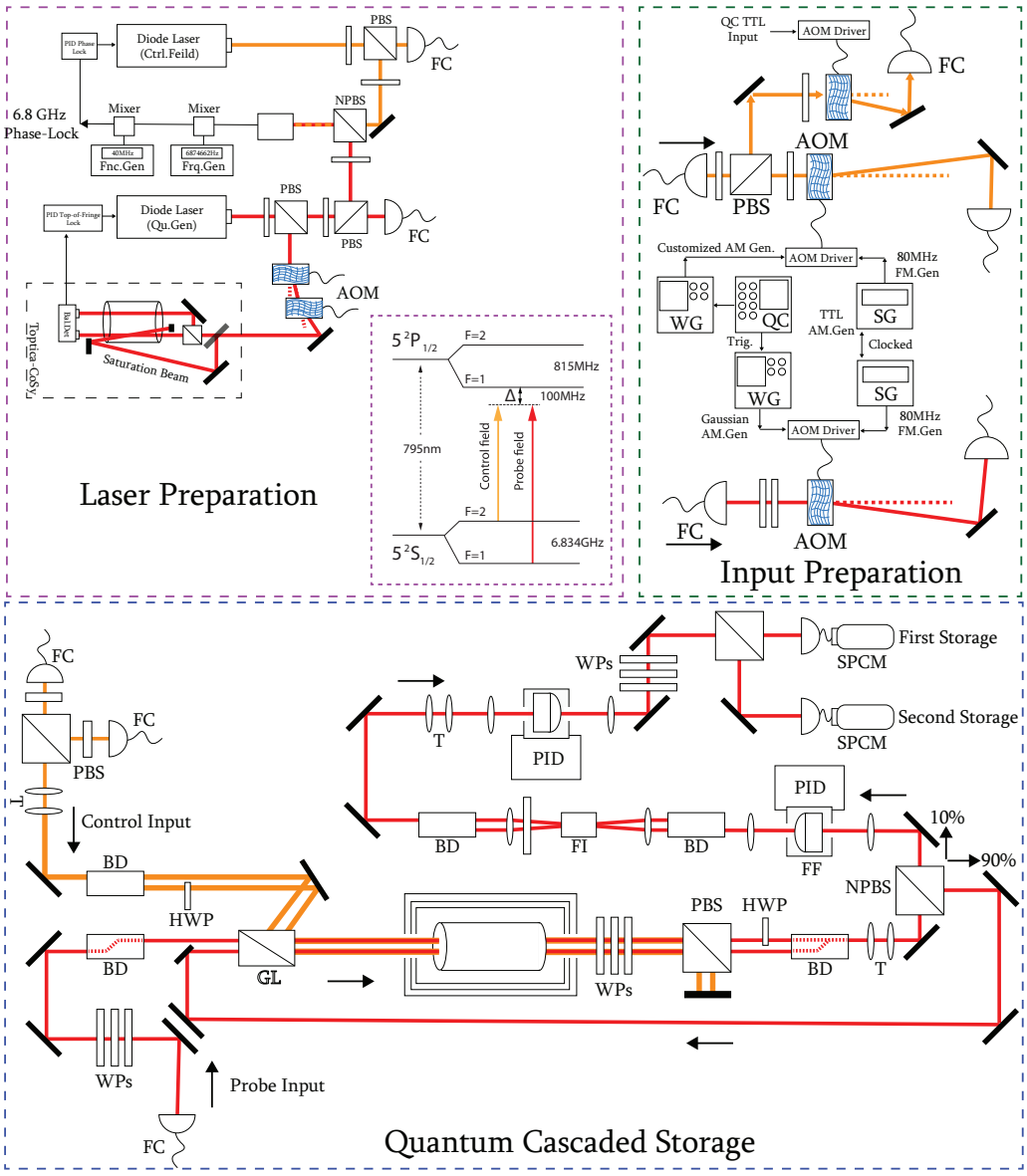


Figure 4.2: **Experimental setup.** Experimental setup for successive storage of pulses at the few-photon level, including the stages of control-filtering. AOM: Acousto-optical modulators; BD: Beam displacers; GLP: Glan-Laser-Polarizer; FR: Faraday rotator; SPCM: Single-Photon-Counting-Module; L: Lens; M: Mirror; NPBS: Non-Polarizing Beam Separator. Probe: red beam paths; control: yellow beam paths. The NPBS sends 10% of the stored pulse to the filtering system to be measured and returns 90% of it back to a second rail through the vapor for a successive stroage.

sharing a common excited state. The probe field frequency is stabilized to the $5S_{1/2}F = 1 \rightarrow 5P_{1/2}F' = 1$ transition at a wavelength of 795 nm (red detuning $\Delta$=100 MHz) while the control field interacts with the $5S_{1/2}F = 2 \rightarrow 5P_{1/2}F' = 1$ transition (see fig. 4.2, laser preparation).

The details of the input preparation state are identical to Chapter 2 with only two modifications: a) We have designed two fully independent control field sequencers to have separate control over each rail of the quantum memory. b) The AOM driver of the first storage control field is receiving its AM input from a wave generator triggered by the quantum composer rather than directly from the composer itself. This was done to modify the temporal shape of the retrieval control field which allows us to mode-match the output of the first storage with the input of the second memory (see fig 4.2, input preparation).

In the quantum memory setup, each rail will serve as a distinct optical memory. The two control field inputs are mapped onto each other with perpendicular polarizations. A polarization beam displacer is used to create a dual-rail set-up for the control field which is mode matched to the probe via a Glan-laser polarizer (see Fig. 4.2, quantum cascaded storage ). An initial input pulse of 1 $\mu$s duration (solid blue line in Fig. 4.3) is fixed to horizontal polarization and sent through the first rail. Using one of the control fields, the probe pulse is stored in a room temperature cell containing Rb vapor for a duration of 1 $\mu$s using EIT for storage and retrieval. For the control field involved in the first retrieval, we employ an user-defined control field temporal dependence, which allows tuning of the instantaneous group velocity of

the retrieved excitation and consequently the tailoring of its temporal shape. We engineer the control field amplitude to provide a retrieved pulse (from the atomic ensemble in rail 1) with a near Gaussian temporal profile (see 2nd peak of solid green line in Fig. 4.3) to yield an efficiency ($\eta_1$) of 12%. We notice that because the length of our vapor cell does not accommodate the full length of the original input pulse, we also have a leakage (see 1st peak of the solid green line in Fig. 4.3). Notice that to compensate for the loss difference of two rails, the stored pulse (solid green line in Fig. 4.3) is scaled by a factor of 1/3.9 in Fig. 4.3.

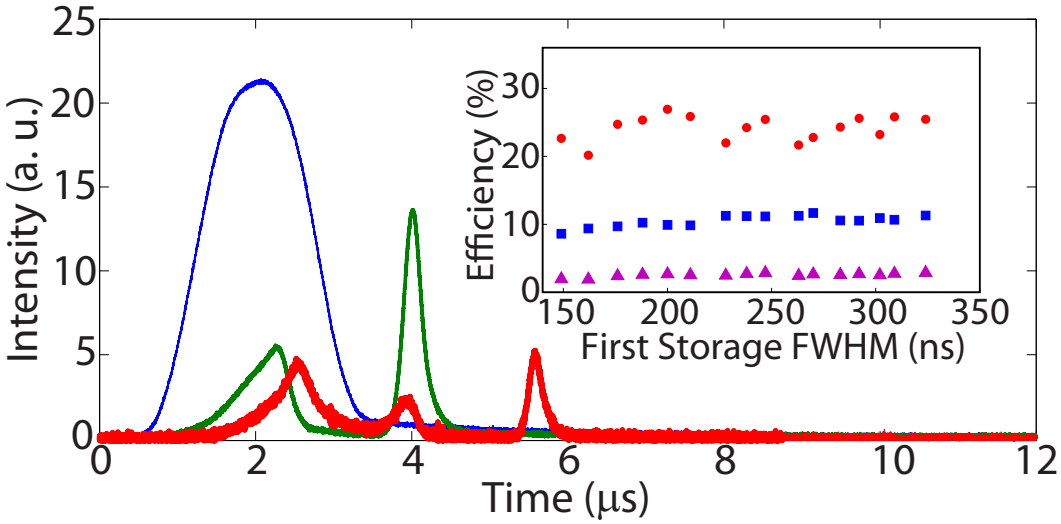


Figure 4.3: **Successive storage of light and the efficiency variation compared to the stored pulse.** Successive storage of classical pulses. Blue: input pulse; Green: stored pulse; Red; The storage of the stored pulse. The blue line is scaled to compensate for the losses of light between the first and the second storage. Inset: The dependency of efficiency to the FWHM of the stored pulse (green line). Blue: Efficiency of the first storage; Red: the efficiency of the second storage; Purple: The overall efficiency of successive storage.

The retrieved pulse passes through another Glan-laser polarizer (used to

remove part of the control field with original polarization V) and an additional beam displacer for recombination of beam paths. After this step, a 90/10 beam splitter is used to send a majority of the retrieved photons back to the front of the vapor cell (see Fig. 4.1) where a pick-off mirror sends the signal (from the memory in rail 1) through the second rail. The timing of control field 2 is matched to the retrieval of the first memory to provide a second retrieval sequence. As shown in Figure 4.3 (red line), the resultant cascaded stored signal has three peaks as was predicted by our simulations.

To maximize the efficiency of the cascaded storage ($\eta_T$), we modify the duration of the control field used for the first retrieval which also affects the temporal length of the retrieved probe field. This has a significant effect on $\eta_T$, as the optimal bandwidth of the retrieved pulse resembles the EIT bandwidth of exhibited by the vapor cell. A total storage efficiency of $\sim 3\%$ is obtained when the duration of the control field for the first retrieval is 300ns. From these values and back calculating the total propagation losses in the path connecting rails 1 and 2 ($\sim 53.4\%$), we can estimate the efficiency of the storage process in memory 2 ($\eta_2$), which yields a value of $\sim 25\%$. Since we are using independent control fields, we can ensure our signal indeed represents excitations that have been stored twice in different spin waves, and not remnants of excitation only stored in rail 1.

Now that we have demonstrated our ability to successively store light pulses, we turn our attention to investigating our system at the few-photon level. Specifically, we are interested in benchmarking the behaviour of the complete optical storage network and determine what the pertinent parame-

ters are to obtain a cascaded retrieved signal (at the end of the network) that is at the same level of the background produced by the experiment, i.e. a signal-to-background ratio (SBR) of 1.

To do so, we will probe our system using faint coherent state pulses near the few photon level. A histogram of the input state is shown in Figure 4.4 (solid green line, from 1 to 2 $\mu$s) for an input mean photon number to be $\sim 8$. In order to sufficiently extinguish the exorbitant number of photons coming from the control field, we employ a filtering system akin to the one used in a previous setup [27]. Note that because the dual-rail setup is generated by beam displacers combining the rails in a single beam path, the filtering setup allows us to examine either the storage of few-photon level pulses in rail 1 (see inset in Figure 4.4) or the cascaded storage at the output of rail 2 (main Figure 4.4).

To determine the total storage efficiency ($\eta_1$) in rail 1, we integrate the number of counts over the region of interest (ROI) corresponding to the retrieved pulse (from 2 to 2.5 $\mu$s in the inset of Fig. 4.4) and subtract the number of counts from a signal-free measurement of the background over the same ROI (from 2 to 2.5 $\mu$s in the inset of Fig. 4.4). The magnified background shape is also included ( dashed black line in the inset of Fig. 4.4). The efficiency is then calculated by comparing this difference in counts to the total counts in the transmitted probe through the filtering system without atomic interaction. The signal to background ratio is obtained in a similar fashion using the counts integrated over the ROI in the storage histogram (signal+background) and the number of counts over a signal-free

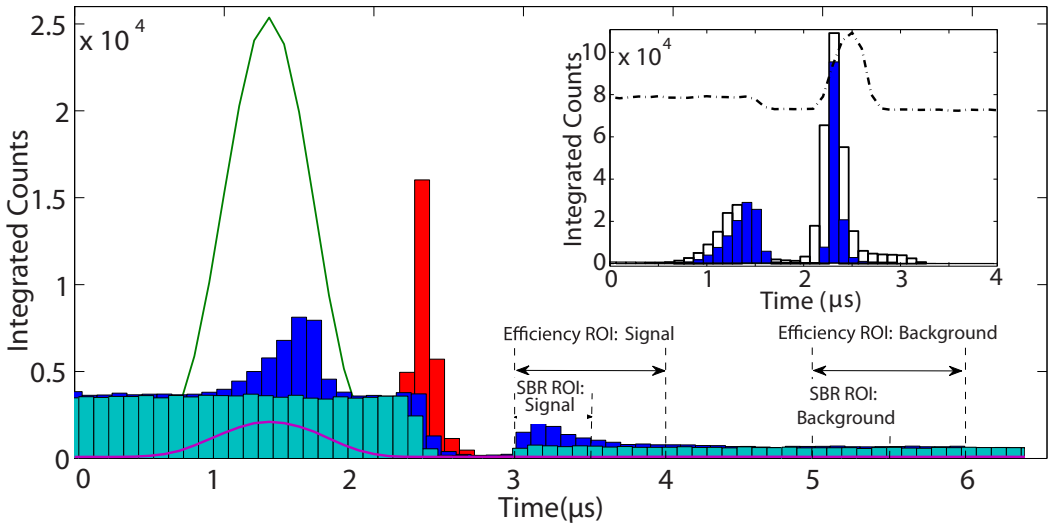


Figure 4.4: **Quantum successive storage of light.** Successive storage of pulses containing 8 photons per pulse on average. Purple: input pulse; Red: absorbed pulse; Green: retrieved pulse after first storage; Blue; retrieved pulse after cascaded storage; The green bars are scaled to compensate for the propagation loses between the storage experiments. Inset: The effect of reshaping the retrieval control field on the storage of pulses. Storage using TTL driven control field (blue bars) and storage counts obtained with a temporally modulated control field (green bars).

region in the same histogram (background). The SBR is then calculated as [(signal+background)-(background)]/(background). In Fig. 4.4, the red bars are again scaled by a factor of 1/3.9 to be consistent.

We show in the inset of Figure 4.4 that there is a considerable effect on $\eta_1$ due to the temporal shaping of the control field retrieval pulse (green bars), as compared to an experiment in which the control field 1 for retrieval is driven by a TTL signal. The optimal retrieval corresponded to a peak power of 90mW in the control field in the initial rail. We have measured a signal-to-background ratio of 13 with an efficiency of 14.6% (see red histogram in Fig. 4.3) with the input state containing a mean photon number of 8.

Due to the NPBS, a majority of the photons retrieved from the first memory are sent to the second rail together with all control field background photons without passing through the filtering setup. We find that after propagation losses (including the routing beam splitter and interconnecting losses from rail 1 to rail 2) of 53.4%, the mean photon number of the probe field at the input of the second memory is 0.6 photons (for the probe) compared to $10^8$ photons from the background. The weak pulses are stored and then retrieved using control field 2 (see dark blue histogram in Fig. 4.4). For comparison, we also show the counts recorded when the input has been blocked (see light blue bars in Fig. 4.4).

From the cascaded storage signal we obtain a SBR of 1.2 for our input state with $\langle n \rangle = 8$. Using a similar procedure to the one described in the previous paragraphs we have determined the overall efficiency of the cascaded storage (using a ROI in the interval from 3 to 4 $\mu$s in Figure 4.3) of $\eta_T = 3.17\%$. Similarly we can back calculate the efficiency of the second memory $\eta_2$ to be 21.7%.

Finally we turn our attention to the noise characteristics of our cascaded storage system. Specifically, we are interested in the influence of the background noise photons generated from the first optical storage event on the final cascaded storage signal (after memory 2). To do so, we have measured the cascaded storage efficiency ($\eta_T$), efficiency of the first storage $\eta_1$ and efficiency of the cascaded (second) storage $\eta_2$ with the mean optical power used in the first optical retrieval. In order to obtain a quality SBR and efficiency, we used input states containing an average of 18 photons per pulse and a

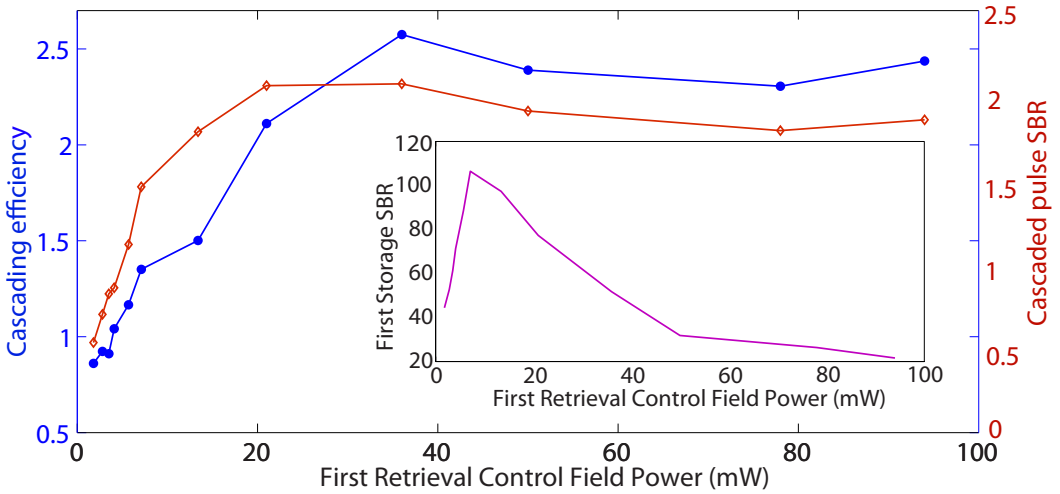


Figure 4.5: **Effect of first retrieval control field on Successive Storage.** Total efficiency (Blue line with circles) and the SBR of the second storage (Red line with diamonds) verses the change in the first retrieval control field power. Inset: SBR of first storage with increasing retrieval power.

TTL driven control field for the retrieval (as oppose to the reshaping method described earlier). In this way, any noise photons generated when the first control field is turned on (either leakage or atomic-triggered background) can be measured at the time of the cascaded storage signal.

The filtering consists of a set of polarization elements supplying 42 dB of control field attenuation while maintaining 80% probe transmission (summing both rails) followed by two monolithic, temperature-controlled etalon resonators to provide a further 102 dB of control field extinction. Overall, our setup achieves 154 dB control field suppression, including the 90/10 Beam Splitter, while yielding a total 0.39% probe field transmission for the first rail and a total 0.22% for the second rail, hence exhibiting an effective, control/probe suppression ratio of average 130 dB. We can see that the total SBR after the cascading event (solid red line in Fig. 4.5) follows the behavior of

the total storage efficiency $\eta_T$ (solid blue line in Fig. 4.4). By comparison, we can see that the SBR for the first storage event (see inset in Fig. 4.5) does not follow the SBR of the cascaded procedure. This indicates that the second EIT storage ensemble additionally serves as frequency filter of the background noise generated from the first storage ensemble. From a quantum engineering point of view this becomes an interesting aspect, implying that filtering schemes may only be needed before final measurement readout of a cascaded set of operations. Having an inherent filtering system provided by the nature of the setup could be beneficial over setups requiring filtering and clean-up hardware and operations after each individual task. The availability of such a self-filtering systems would lead to a decrease in both experimental overhead and loss of signal in the construction of networks of this type.

## 4.2 Parallel Quantum Memories

So far we investigated the interconnectivity of two in-series light-matter interfaces. In this section, we will discuss a network of two fully independent polarization qubit quantum memories. As we discussed in chapter 1, a practical quantum repeater requires four quantum memories to store two pairs of entangled photons. For the entanglement swapping process to be successfully done in a quantum repeater, the outputs of two of these memories need to interfere by passing through a non-polarization beam splitter which results in entangling the photons stored in the other two memories.

One of the big challenges to create a quantum repeater is to demonstrate suc-

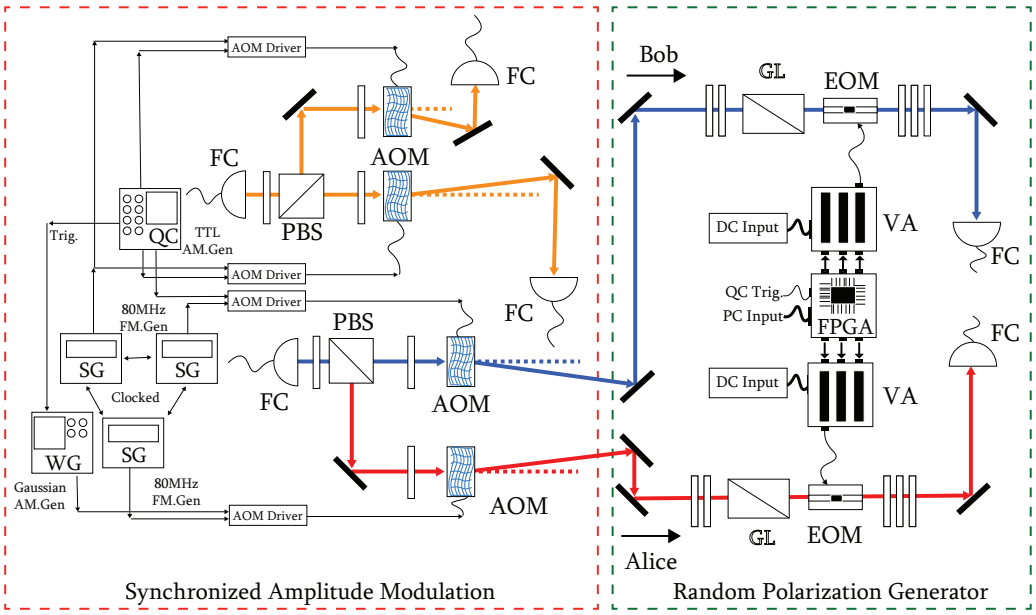


Figure 4.6: The Blueprint of the random qubit station. The setup can be divided into two main segments: First we temporally modulate the input qubits with a 400ns FWHM Gaussian curve after which pulses enter an optoelectrical section capable of randomly (or sequentially) polarizing each pulse using Electro-Optical Modulators (EOMs).

cessful Hong-Ou-Mandel (HOM) interference between two stored photons. In order to show that our memories are capable of perfectly preserving the initial states and retrieve identical pulses, we create a HOM measuring station, Charlie, to measure the coincidence rate of photons in two individual single photon counters. Because any 1:1 beam splitter is a unitary transformation, if two identical photons arrive at a beam splitter, the probability of simultaneous click of the two photon counters goes down to zero. In the case of weak coherent pulses containing on average less than a photon, the HOM coincidence rate goes to half of the rate for two indistinguishable photons, hence giving us a tool to measure how identical the output of two separate quantum memories

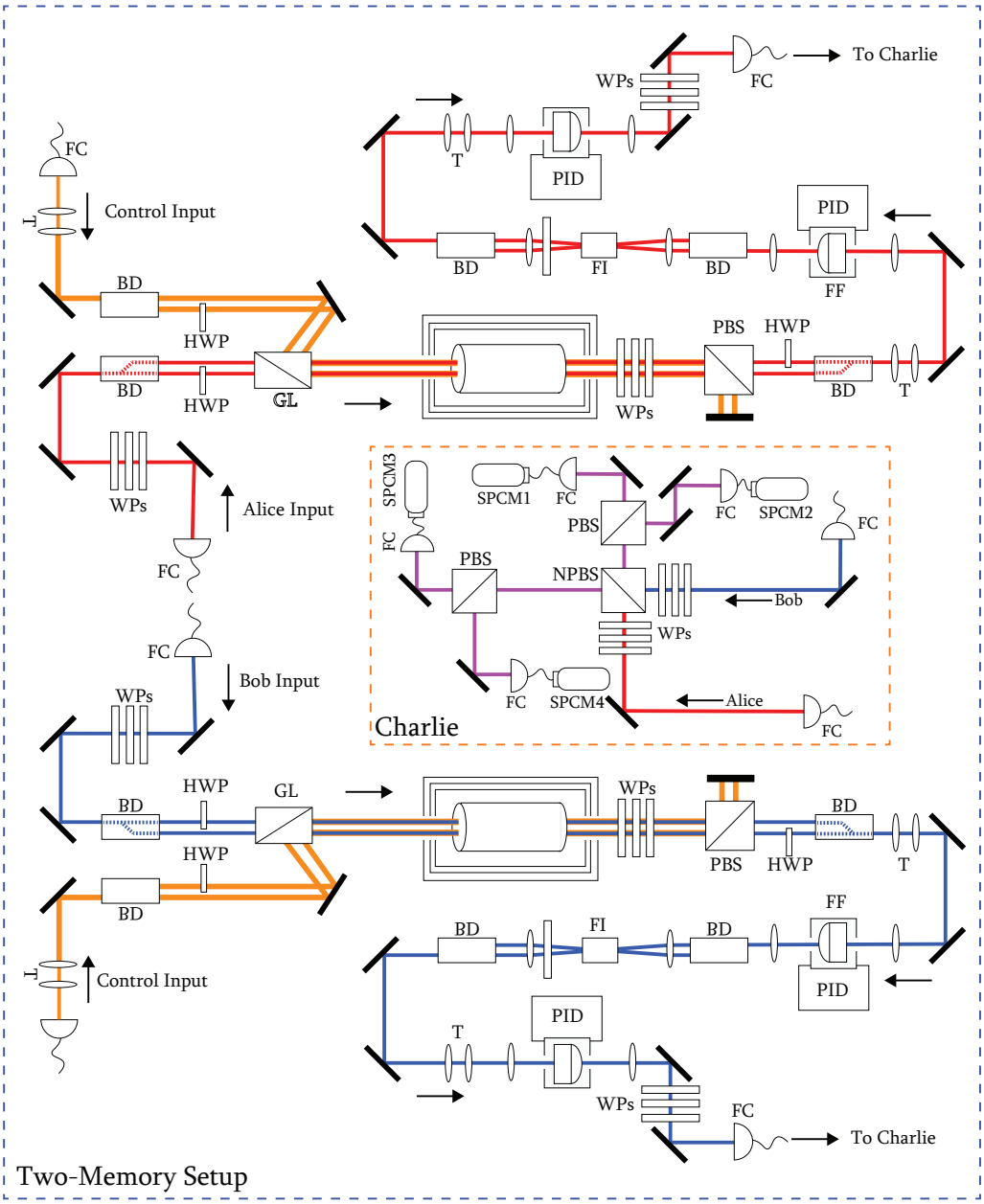


Figure 4.7: Experimental setup for observing a HOM interference of two coherent optical pulses after being stored in two individual room temperature quantum memories. Alice and Bob generate pulses with approximately $< n = 10 >$ photons per pulse. the outputs of the memories are sent to a detection setup, in which they are interfered in a non-polarizing beam splitter. After interference, we analyze the two-photon polarization state by simultaneous measurements in two polarization detectors.

are.

### 4.2.1 Experimental Setup

Four independent AOMs, placed in Lab I, are responsible for temporally shaping the probe and control field input of each memory (see fig. 4.6). To be in line with the quantum communication community, we name the two probe inputs as Alice and Bob. As the network grows, the precise control of the AOMs becomes more crucial. Three signal generators are clocked to each other to provide the 80MHz frequency modulation needed for the AOMs with enough flexibility for fine tuning the two-photon detuning of each memory. Two wave generators triggered by the master quantum composer are used to generate the 400ns FWHM Guassian envelope of the probe pulses. We use single photon counting modules (SPCMs) to fine tune the widths and the arrival time of the pulses with a nano-second precision. After the Gaussian pulses are generated, two Electro-Optical Modulation units (EOMs) are in place to code the desired polarization states on the pulses. EOMs are capable of modulating the output polarization based on the input applied voltage on the $|H, V>/|R, L>$ plane. Using a set of wave-plates we map this plane on $|H, V>/|D, A>$ and after calibrating the input voltages (usually in the range of 0-500V) we can generate $|H>$, $|V>$, $|D>$ and $|A>$ states. Two fast switching high voltage amplifiers are responsible to apply the input voltage while the temporal pulse is inside the AOM. Both voltage amplifiers are controlled with an FPGA-based circuit for fast switching. The FPGA can be programmed to generate any sequence of polarizations including a fully random sequence. All the electronic com-

ponents are made in our lab and the latest generation of our FPGA-based circuit has an internal random number generator based on atomic decay of Cs isotopes. For this section we will employ the FPGA to generate a pre-assigned sequence of polarizations. Finally, the qubit sequence is delivered to Lab II via 30m long non-polarization maintaining single-mode optical fibers.

Two individual dual-rail quantum memories at Lab II, are responsible for receiving and storing photons from Alice and Bob (see fig. 4.7). The technical layout of each memory is identical to the setup used in Chapter Two. Upon successful storage of pulses in both memories, the output of the memories are fiber-coupled to the Charlie station for quantum interference measurement (see fig. 4.7, orange inset).

Charlie is a four-SPCM-based multi-purpose quantum measuring station designed to be used for HOM, BS, and MDI-QKD measurements. Alice and Bob input pulses are compensated for any polarization rotation at the input of Charlie before entering a 1:1 non-polarizing beam splitter (NPBS). The NPBS is customized to have 50/50 ratio within $\pm 2\%$. After the NPBS, a PBS at each port splits the photon pulses into H and V and sends them to four separate SPCMs. If the input photons are decoded to be H(V), the coincidence rate is only between detectors 1 and 3(2 and 4). For all other polarizations we measure the coincidence rate of photons arriving at detectors 1+2 and 3+4 simultaneously. The quantum interference happens at the NPBS which results in a reduced coincidence rate of the indistinguishable photons. It is shown that for true single photons this rate goes down to zero while for weak coherent pulses containing on average one or less photons the rate reduced to

50%.

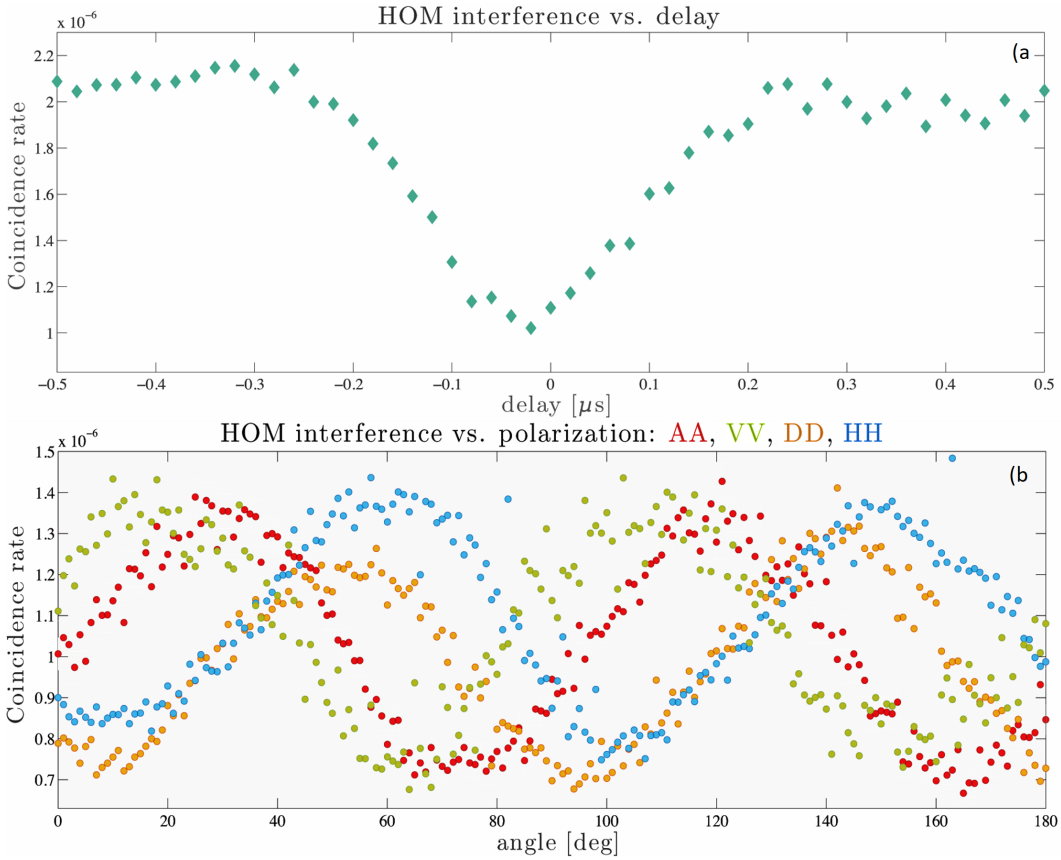


Figure 4.8: The HOM measurement results of polarized photons generated by Alice and Bob and Charlie station: a) HOM dip vs. the pulse delay, and b) HOM oscillation of all four polarization states vs. polarization rotation.

### 4.2.2 Second-Order Interference of Polarization Qubits

There are two common approaches to measuring HOM interference, by either scanning the input polarization or by scanning the temporal overlap. The key is to scan a parameter that varies the "degree of indistinguishability" of

the arriving photons. A typical design of HOM measuring setup contains a piezo-mounted mirror to allow for fast scan of the photons temporal overlap by changing the path length of one pulse with respect to the other. Such scan is not applicable to our system as the spatial coherence length of our qubits (120m in free-space) is much longer than the scan range of a piezo. To solve this obstacle, we directly scan the delay parameter of the wave generator that creates the temporal envelope of Alice (or Bob) AOM. We observe a 48% decrease in the coincidence rate (see fig. 4.8a) of horizontally polarized inputs with an average $< 0.4 >$ photons per pulse. The 2% loss in the HOM visibility can be related to the accuracy of the EOMs in modulating the polarization of the pulses and the mode-matching of the beams at the NPBS at Charlie. As expected, the width of the HOM curve matches exactly the temporal width of the input pulses (200ns for this measurement).

When using polarization qubits, it is also possible to observe the quantum interference while the pulses are fully overlaping by continuously varying the polarization of the qubits. This can be achieved by rotating the input polarization of one of the pulses relative to the other. Eventually, after a $90^o$-degrees rotation, the qubit polarizations will be perpendicular to each other, which results in two distinguishable photons with a maximum coincidence rate at the outputs of the NPBS. To ensure that our setup is balanced for all the input states, we have measured the HOM oscillation versus the relative polarization angle for all four qubit states (see fig. 4.8b) and achieved an average of 48% ($\pm$0.2%) decrease in the coincidence rate.

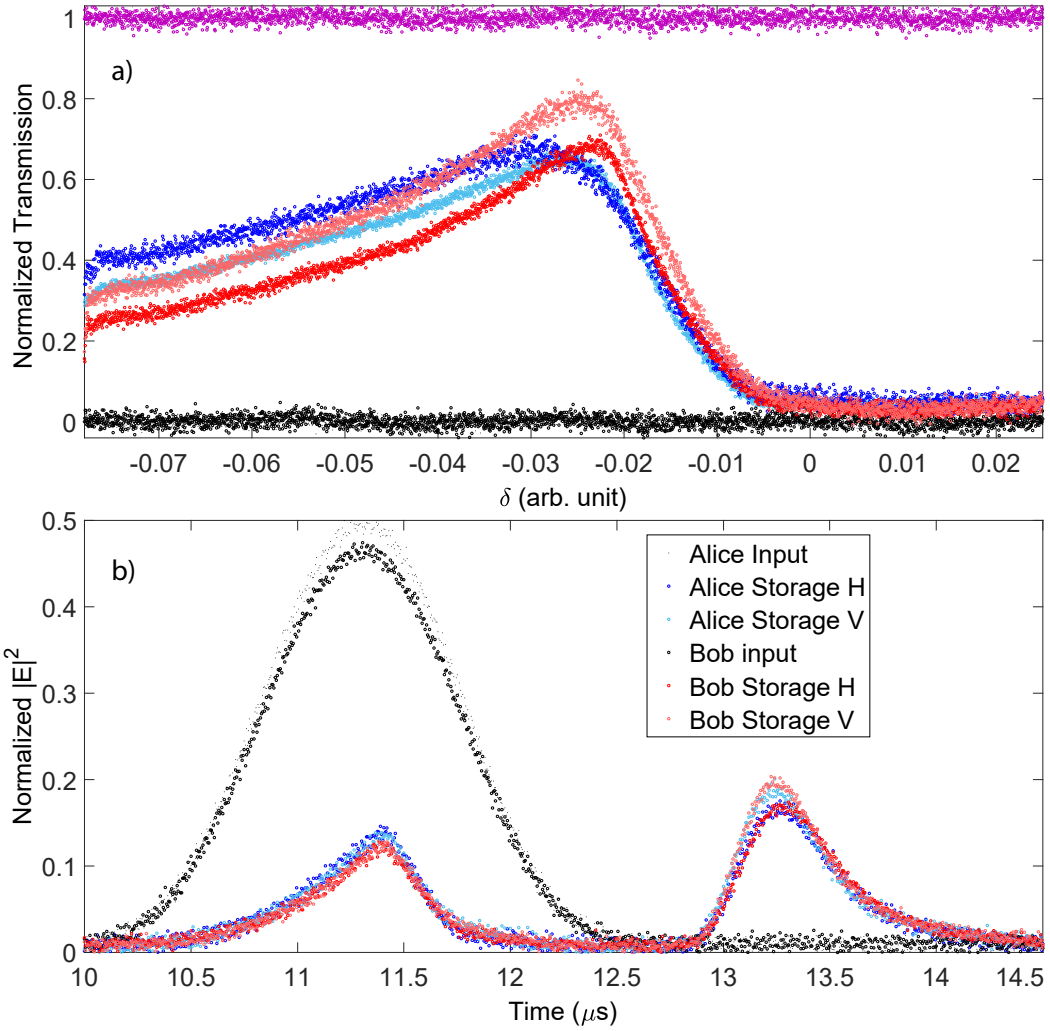


Figure 4.9: Mode-Matching of four single rail quantum memories: (a) The EIT lines for $|H>$ and $|V>$ rails, purple line: memory-free transmission, black line: atomic absorption, dark and Light blue: EIT lines for each rail of Alice memory and dark and light red: EIT lines for each rail of Bob memory. (b) Classical storage of each memory rail, black lines: input pulses for Alice and Bob, dark and light blue: storage of $|H>$ and $|V>$ pulses with Alice memory and dark and light red: storage of $|H>$ and $|V>$ with Bob memory, respectively.

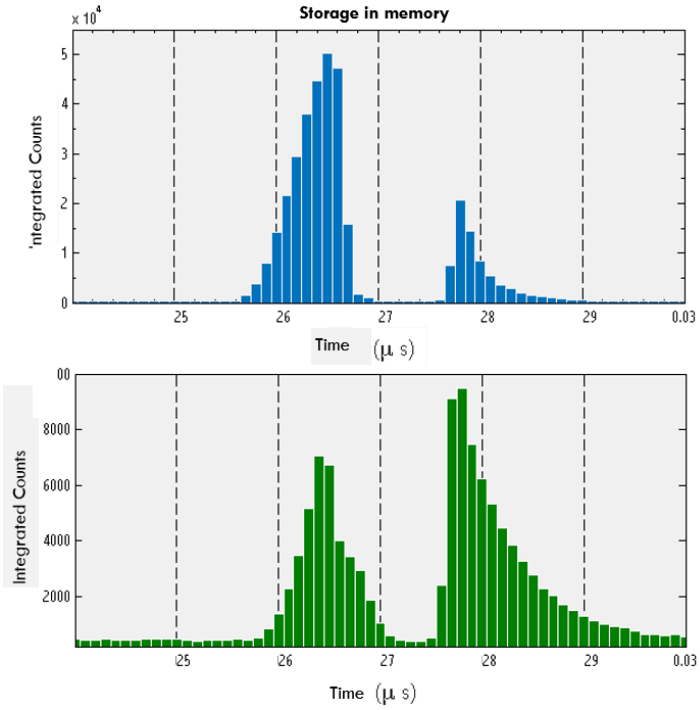


Figure 4.10: Simultaneous storage of few photons pulses carrying a $|D>$ polarization in two separate quantum memories

### 4.2.3 Second-Order Interference of stored photons

Each polarization quantum memory consists of two rails for storing $|H>$ and $|V>$ components of optical pulses. To preserve the indistinguishability of the input polarization qubits during the storage, all four memory rails must have identical EIT bandwidths (to preserve the frequency of the qubits) and storage efficiencies (to preserve the polarization of the qubits). This is possible by carefully adjusting all the electrical and optical parameters of the quantum memories (see fig. 4.9). Furthermore, we have made sure that all the four etalon filters have similar bandwidths (20MHz-40MHz)and identical transmission for $|H>$ and $|V>$. Figure 4.10 demonstrates the $1\mu$s long storage of two $|D>$ polarized pulses from Alice and Bob in our two dual-rail memories. As the first step, we have increased the number of input photons to an average of

$< 10 >$ per pulse in order to achieve high enough SBRs to avoid the destructive effects of the background noise (which is unpolarized) and solely study the retrieved pulses. One of the advantages of having quantum memories in this setup is that the input pulses do not need to be generated simultaneously and as long as they depart the quantum memories and arrive at Charlie at the same time, the second-order interference should be observable. This is a key feature that allows quantum repeaters defeat the natural losses of fiber optics while allowing the realization of imperfect quantum networks.

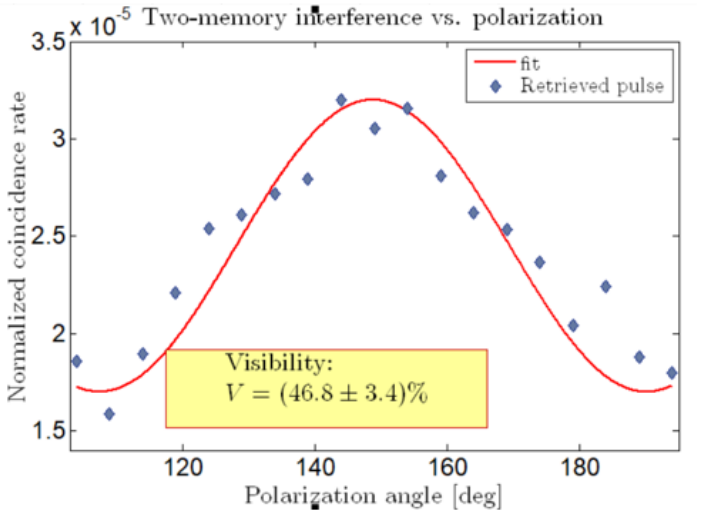


Figure 4.11: Hong-Ou-Mandel quantum interference for the output of the two quantum memories.

The stored pulses then overlap at Charlie where we can measure their coincidence rate. We generate temporally identical outputs by carefully matching all the relevant parameters in the quantum memories such as two-photon detunings, storage time, filtering transmission, and the EIT linewidths. The coincidence rate is measured versus the relative polarization of output pulses (see fig. 4.11). In the beginning, both memories are retrieving identical photons with the same temporal shape, frequency, and polarization, resulting in

a minimum in the coincidence rate. We then rotate the polarization of one of the output pulses before it reaches the beam splitter in order to make them distinguishable. Doing so results in a peak in the coincidence rate after 45 degrees rotation. We measure an interference visibility of $V = 46.8\% \pm 3.4\%$. The major source of the imperfection of the visibility is due to the input polarization station and Charlie's alignment. Typically the EOMs modulate the polarization within 1% accuracy which translate to 2% visibility loss at Charlie. The achieved results correspond to a quantum impedance matching fidelity of 97.6% between the output of two memories. This result can be used as a proof of principle for the feasibility of using EIT-based quantum memories as the building blocks of quantum repeaters.

## 4.3 Summary

In summary, we have demonstrated the cascaded storage of few-photon level pulses using two distinct room temperature ensembles contained in the same vapor cell. Our results show that with our current technology it is possible to realize the interconnection of two quantum light-matter interfaces in a sequential manner, a key attribute of a quantum optical network. This could be a milestone towards building more sophisticated machines that include many more interacting quantum nodes, thus paving the way for elementary one-way quantum information processors. We have also demonstrated an optimal quantum interference between the output of two separate quantum memories, a key feature for development of future quantum repeaters. In the next chap-

ter, we will conduct a final test on the quantum memories and use them within quantum secured systems.

# Chapter 5

# Quantum-Secured Systems

So far we have demonstrated the benefits of using EIT-based light-matter interfaces at room temperature to create quantum nodes for storage and processing of quantum information. We also deployed these nodes in networks of two memories to achieve the quantum connectivity needed to move towards developing more complex systems such as quantum repeaters. To be suitable for quantum communication purposes, these memories must pass one final test, store quantum information securely. The most important advantage of using quantum communication over digital networks is to boost the cyber-security of the channels to an eventual goal of un-hackable networks. The integrity of todays communication networks depends on well-known public key ciphers. These algorithms are based on mathematical equations that are fast to compute but require an excessive amount of processing power to decrypt. One of the biggest weaknesses of these protocols is that they are only secure against the current processing power accessible to hackers. The calculations needed

to break into a channel which take years now will be done within a second using a potential quantum computer. The most promising hardware option and long-term solution to address these issues is quantum cryptography. This method uses quantum properties such as the anti-commutator relationship between two observable to exchange secret information. The security of quantum ciphering relies on the fundamental laws of nature, which are invulnerable to increasing computational power, new attack algorithms or even quantum computers.

Development of such secure networks is currently limited by the optical fiber loss to distances about 100km. Quantum repeaters can be the key to break this barrier and realize intercontinental quantum communication networks but even before that, integrating quantum memories and entanglement sources within these networks can help to achieve quantum-secured communication between cities and nearby states. In this chapter, we will design a quantum system consisting of several quantum modules all working together to realize an ultra-secure communication link. We then integrate quantum memories to these systems in order to study how these memories respond to receiving random strings of polarization qubits.

The bulk part of this chapter is on a quantum system in which a room-temperature quantum memory assists a quantum-secured network based on the BB84 protocol. Such a network that is intrinsically secure and operates over long distances requires the interconnection of several quantum modules performing different tasks. In this chapter we study the interconnection of four

different quantum modules: (i) a random polarization qubit generator, (ii) a free-space quantum communication channel, (iii) an ultra-low noise portable quantum memory and (iv) a qubit decoder, in a functional elementary quantum network possessing all capabilities needed for quantum information distribution protocols. We create weak coherent pulses at the single photon level encoding polarization states $|H\rangle, |V\rangle, |D\rangle, |A\rangle$ in a randomized sequence. The random qubits are sent over a free-space link and coupled into a dual rail room temperature quantum memory and after storage and retrieval are analyzed in a four detector polarization analysis akin to the requirements of the BB84 protocol. We also show ultra-low noise and fully-portable operation, paving the way towards memory assisted all-environment free space quantum cryptographic networks. The last section of this chapter will provide the road-map for developing network of multi-memory MDI-QKD.

## 5.1 Development of Modular Quantum Networks

### 5.1.1 Introduction

The field of quantum information has recently seen remarkable progress regarding the implementation of elementary quantum devices and quantum communication protocols. On one hand, the advent of photonic quantum communication using long distance free space links [127, 128, 129, 130, 131] has opened the possibilities to securely exchange quantum states and entanglement

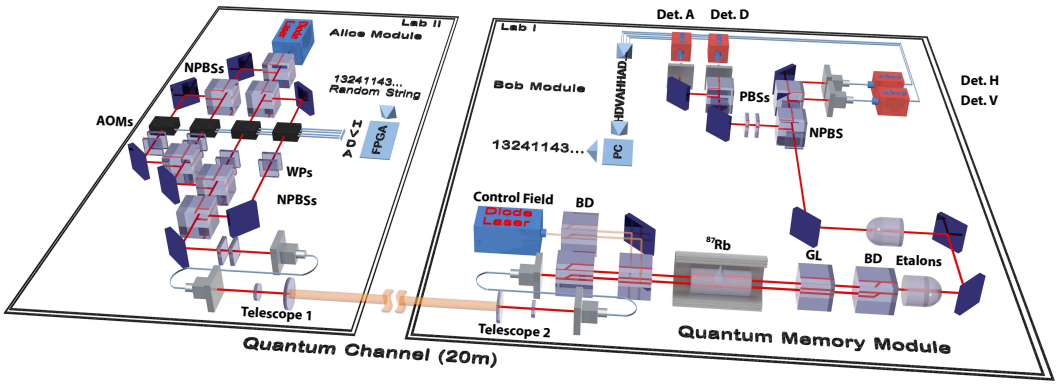


Figure 5.1: **Experimental setup for free-space quantum communication.** In Laboratory II Alice creates a random sequence of four orthogonal qubits ($|H\rangle, |V\rangle, |D\rangle, |A\rangle$). The 400ns-long qubits are produced every 40 $\mu$s. The qubits propagate in a free-space quantum communication channel over a distance of $\sim$ 20m and are then directed into a dual rail room temperature rubidium vapor quantum memory in Laboratory I. The control storage pulses are time-optimized to the arrival of the qubits in front of the memory. In Bob's site a four detector setup measures all possible basis at the exit of the memory to determine the quantum bit error rate (QBER). PBS: polarizing beam splitter, WP: wave plates, AOM: acousto-optical modulator, BD:beam displacer, GL: Glan-laser polarizer.

[132, 133, 134]. These developments together with quantum key distribution protocols have enormous potential for the creation of a global, secure quantum information exchange network [135, 136, 137, 138, 139, 140, 141]. On the other hand, an entirely different community of quantum scientists has developed sophisticated quantum light matter interfaces capable of receiving, storing and retrieving photonic qubits [142, 143, 144, 145]. Such devices, collectively known as quantum memories already operate with high fidelities[146, 147, 187], long storage times [149, 150] and high storage efficiencies [151, 152]. Furthermore, quantum memories already operate at room temperature [126, 153, 154], thus facilitating their interconnection with other quantum devices.

The construction of an interconnected set of many quantum devices that performs secure communication protocols in outside settings and with moving targets it is now within experimental reach [155, 156, 157]. Therefore it is of utmost relevance to engineer elementary networks of a few quantum nodes and quantum channels in order to understand the potential of these novel architectures [45, 46, 158, 159]. The emergent behaviour of such small quantum networks should allow us to realize more sophisticated quantum procedures [160]. An important example of such an elementary network will be the modular connection of quantum cryptography systems operating over free-space quantum channels [161], assisted by room temperature quantum memories increasing the distance, security and connectivity of quantum key distribution protocols [141, 140].

Paramount to the creation of such a free-space memory assisted quantum communication network is the use of shot-by-shot unconditional quantum memories capable of supporting the specific technical demands of outside-of-the-laboratory quantum communication channels. Among them, accepting random qubit states necessary to perform quantum key distribution protocols, having a minimized quantum bit error rate (QBER) and receiving spatially multi-mode signals, while simultaneously being cost-effective and fully-portable. These capabilities will allow the construction of elementary quantum networks without the need for frequency conversion among their components, that are intrinsically secure, quantum coherent and compatible with long distance operation.

Throughout this chapter, we report the creation of such an elementary quan-

tum network in which we mimic these desired properties into a scaled down setup. We present individual experiments addressing the various challenges in order to create the quantum connectivity needed to perform memory-assisted long distance communication of random polarization qubits. To our knowledge, our results represent the first time that the ideas of quantum communication, as used in the well known BB84 protocol, are combined with low-noise room-temperature quantum storage. Our results are obtained by cascading four different quantum modules: a random polarization qubit generator, a free space quantum communication channel,warm vapor quantum memory and a qubit decoder.

### 5.1.2 Experimental procedure.

Our elementary quantum network starts with the creation of a sequence of four polarization states ($|H\rangle, |V\rangle, |D\rangle = 1/\sqrt{2}(|H\rangle + |V\rangle), |A\rangle = 1/\sqrt{2}(|H\rangle - |V\rangle)$) in a distant laboratory (Alice's station, Laboratory II in Fig. 5.1). To test a different input preparation method, we create the qubits using 400ns-long pulses produced every 40 $\mu s$ by 4 individual acousto-optical modulators. In order to compensate for small deviations in the length of each AOM track, the AOMs are each driven by independent sources regarding their amplitude and frequency modulation. The setup is designed to generate either an ordered sequence of four qubits in cycles of 160 $\mu s$ (see Fig. 5.2) or a train of qubit pulses where the modulation sources are controlled by a FPGA chip programmed to randomly trigger one of the four AOM's. The resulting random sequence of pulses is attenuated to the single-photon-level and then sent into free space

quantum channel module.

The qubits created in the Alice station propagate in a free-space quantum communication channel over a distance of $\sim$ 20m without shielding or vacuum propagation and are then directed to a quantum memory setup in a different laboratory. We have chosen the characteristics of this setup as a test bed of the interconnectivity of this station and the quantum memory setup under more challenging out-of-the-laboratory operation. Of particular interest are the shot-by-shot changes in the mean input photon number due to the air turbulence between the laboratories and the capability of the memory to receive random polarization inputs, pulse-by-pulse. By careful alignment the loss in the free space propagation is set to be less than 4%. Together with 63% fiber coupling efficiency at the receiving end of the quantum memory setup this yields a total transmission of 59% for the quantum communication channel. The shot-by-shot fluctuations in the mean photon number were measured to be $\sim$ 5%.

Located in Laboratory I is the room temperature quantum memory in which we store the incoming qubits. The quantum memory is based upon a warm $^{87}$Rb vapor and controlled using electromagnetically induced transparency (EIT). Two independent control beams coherently prepare two volumes within a single $^{87}$Rb vapor cell at 60° C, containing Kr buffer gas to serve as the storage medium for each mode of the polarization qubit. We employed two external-cavity diode lasers phase-locked at 6.835 GHz. The probe field frequency is stabilized to the $5S_{1/2}F = 1 \rightarrow 5P_{1/2}F' = 1$ transition at a wavelength of 795 nm while the control field interacts with the $5S_{1/2}F = 2 \rightarrow$

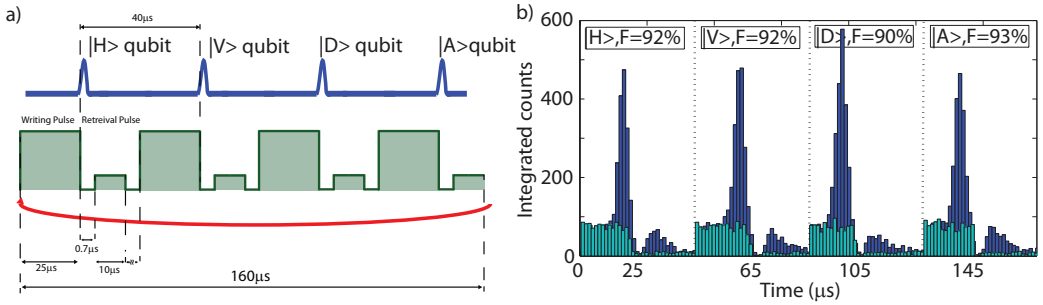


Figure 5.2: **Storage of a sequence of qubits.** (a) A stream of polarization qubits with on average 3.5 photons propagates through a free space quantum communication channel of 20m. In the quantum memory site, the single-photon level qubits are received and stored sequentially using timed control field pulses. (b) Histograms for each of the polarization inputs after storage (dark blue) and background floor (light blue). Each histogram is presented in a $2\mu$s time interval (see dashed black divisions). The fidelities are estimated from the signal-to-background ratio
.

$5P_{1/2}F' = 1$ transition. Polarization elements supply 42 dB of control field attenuation (80% probe transmission) while two temperature-controlled etalon resonators (linewidths of 40 and 24 MHz) provide additional 102 dB of control field extinction. The total probe field transmission is 4.5% for all polarization inputs, exhibiting an effective, control/probe suppression ratio of 130 dB [**?**]. The control field pulses are time-optimized to the arrival of the qubits in front of the memory (see Fig. 5.2a).

After passing through the polarization independent frequency filtering system, the stored pulses enter the Bob module, which is equipped with a non-polarizing beam splitter (separating the $Z = \{|H\rangle, |V\rangle\}$ and $X = \{|D\rangle, |A\rangle\}$ bases) and two polarizing beam splitters whose outputs are detected by four single-photon counting modules (SPCM). Each SPCM corresponds to a differ-

ent polarization state. This allow us to compare the detected sequence with the originally sent qubits and estimate the influence of the photonic background of the memory in the evaluation of the QBERs.

## 5.2 Storage of a sequence of four polarization qubits after free space propagation.

In our first experiment, a string of four ordered polarization qubits ($|H\rangle$, $|V\rangle$, $|D\rangle$ and $|A\rangle$) is sent from Alice module to the memory and Bob terminal through the free space channel in order to test the compatibility of all the modules and the performance of the quantum memory at the single photon level (see Fig. 5.2). The characterizations of the qubits after storage is done with a single detector placed after the memory bypassing the polarization analysis setup. We create histograms using the time of arrival and estimate a best-case-scenario fidelity of the stored polarization qubits containing on average 1.6 photons per pulse right before the memory.

We evaluate the signal to background ratio (SBR) in the measurements, defined as $\eta/q$, where $\eta$ is the retrieved fraction of a single excitation stored in a quantum memory and $q$ the average number of concurrently emitted photons due to background processes. Both are calculated by integrating the retrieved and background signals over 100 ns intervals. The fidelities are then estimated as $F = 1 - \frac{1}{2}\frac{q}{\eta}$. Our analysis shows that even with the additional constraint of shot-by-shot fluctuations in intensity due to free space propagation and the addition of randomly polarized background photons in the memory, maximum

fidelities of 92% for $|H\rangle$, 92% for $|V\rangle$, 90% for $|D\rangle$ and 93% for $|A\rangle$ can still be achieved.

These results are clearly above the classical threshold limit of 85% for the corresponding efficiencies thus providing the necessary condition of unconditional quantum memory operation [126]. They also show that our room temperature quantum memory implementation operates with the same parameters regardless of the polarization input, a fundamental attribute if the memory were to work as either a synchronization device for quantum cryptography protocols in which a stream of random qubits is used to distribute a quantum key or a as memory for polarization entanglement in a quantum repeater architecture.

## 5.3 Storage of a random sequence of polarization states with high photon number.

After showing unconditional memory operation over the free space network, we now show that the network also operates with high fidelity on a pulse-by-pulse basis, demonstrated by full polarization analysis at Bob location. This is done by randomizing the polarization input of the experiment. Further insight into our current capabilities is obtained by analyzing the quantum bit error rates (QBER) $Q_X$ and $Q_Z$ for $X$ and $Z$ bases after propagation and storage. Starting with pulses containing high number of photons ($\sim$ 100 photons, see Fig. 5.3), we evaluated the QBER after storage of the random polarization states. An average QBER of 0.57% for the two orthogonal bases have been measured within a region of interest equal to the input pulse width. This

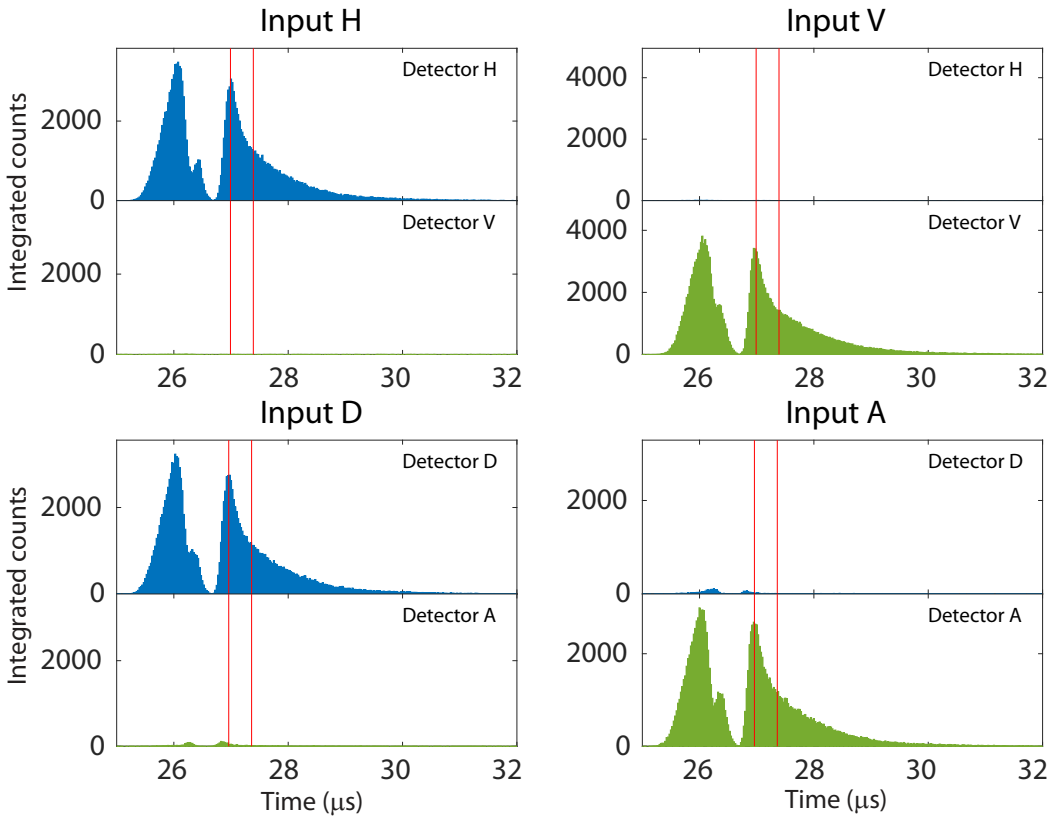


Figure 5.3: **QBER evaluation of the long distance communication setup plus memory.** In the Bob site the polarization states are received and stored sequentially in a room temperature quantum memory. We randomly choose one of the Z and X bases to measure the polarization state, and then calculate the QBER over a region of interest equal to the input pulse width (red bars). We show histograms on the photons counts in each of the four polarizations. The first peak represents non-stored photon (leakage) while the second peak represents the retrieved photons. In an experiment with high input photon number, the obtained QBERs are less than 1%, as it can be seen in the low counts corresponding to undesirable polarization detections.

QBER is compatible with the typical error rate obtained in a standard quantum key distribution experiment. The importance of this result is two-fold: 1) the storage process at room temperature does not intrinsically add non-unitary rotation to the states, and in the limit of high signal-to-background

has negligible effect on the total QBER; 2) the memory is capable of storing and retrieving generic polarization qubits on a shot-by-shot level.

## 5.4 Storage of a random sequence of polarization qubits.

In our next experiment the complete state measurement in the two bases was used again for an input of 1.6 photons before the memory, corresponding to 3.5 photons at Alice station. The evaluated QBERs after storage for polarization qubits are $Q_Z$= 11.0% and $Q_X$ =12.9% over a 100 ns region (see Fig. 5.4). The increase of the QBERs is only due to the background noise which is much more significant at the single-photon level. Nonetheless, the fidelities (corresponding to 1−QBER) still remain higher than the classical limit for the corresponding storage efficiency. The latter result is rather counter-intuitive when dealing with superpositions $|D\rangle$ and $|A\rangle$ as it implies that the two rails forming the quantum memory store or miss the pulse coherently (in order to preserve the storage fidelity for that particular polarization), as opposed to retrieving rather $|H\rangle$ or $|V\rangle$ at any given time in a shot-by-shot experiment. This ability is crucial in networks performing quantum key distribution protocols and it also shows that the memory is currently capable of receiving entangled polarization states without distorting them. We do mention that this last experiment constitutes the quantum communication part of the well known BB84 protocol [162], with the addition of a synchronizing quantum memory between Alice and Bob.

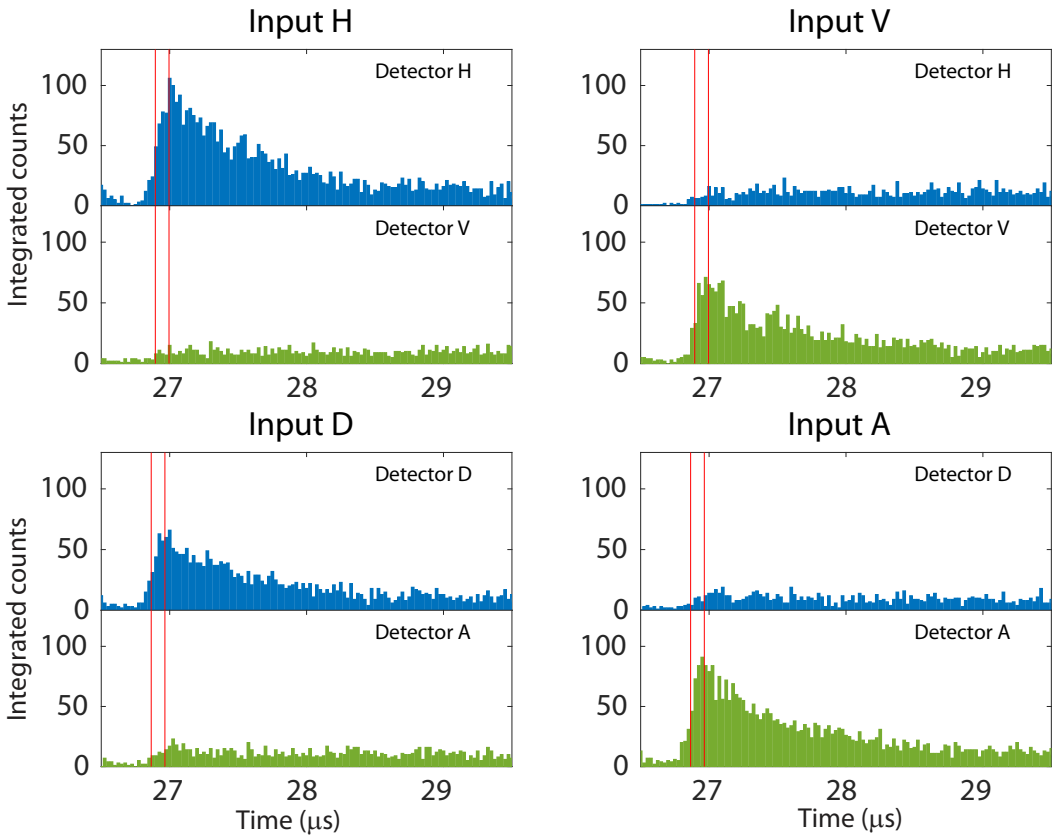


Figure 5.4: **QBER evaluation for single photon level experiment.** (a) The QBER is calculated in a $100ns$ window (red bars). QBER of 11.0% and 12.9% are respectively achieved for Z and X bases. At the single-photon level undesirable polarization rotations remain absent, noise in the orthogonal channel arises from control-field induced non-linear processes.

### 5.4.1 Noise-free operation and QBER improvements.

In order to unlock the potential of our elementary realization as a quantum cryptography network, the main bottleneck identified in the aforementioned experiments is the memory performance at the required single-photon level. Naturally, there has to exist a compromise between room-temperature, all-environment operation and the background noise of the device at the quan-

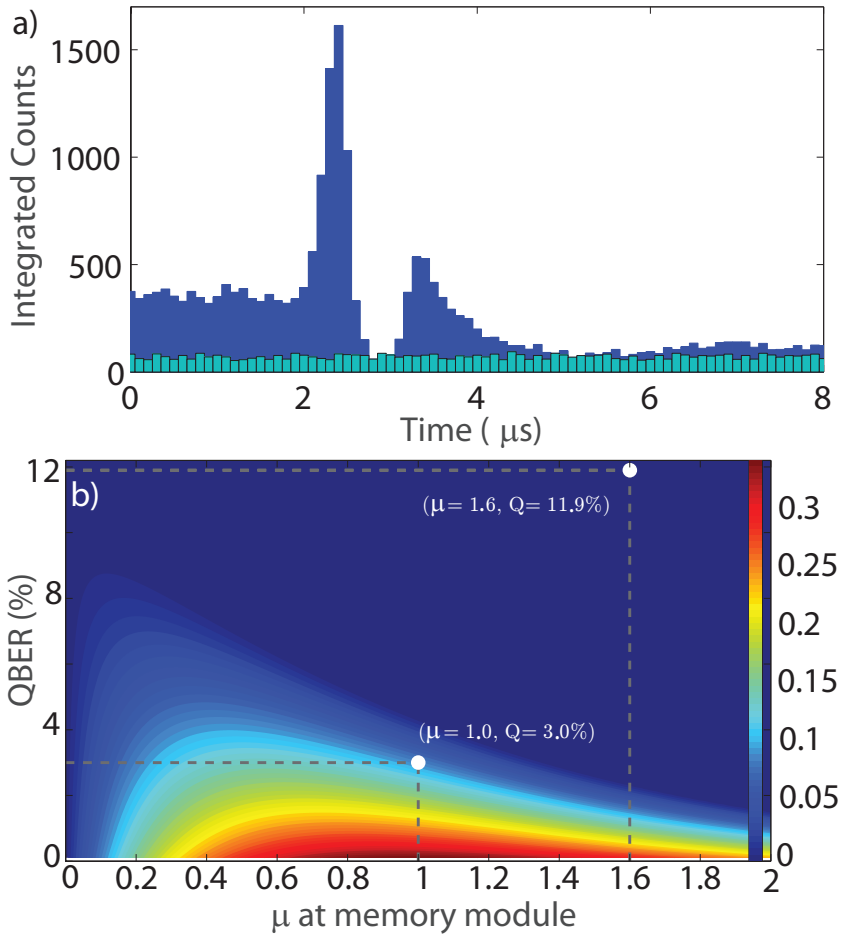


Figure 5.5: **Noise-free quantum memory operation**. a) Noise reduction by introducing an auxiliary field (light-blue histogram), the interaction between dark-state-polaritons creates a background free region. Retrieving the probe under these conditions results in a SBR >25. The SBR is calculated using a 100 ns intergration region at the peak of retrieve signal and a minimized averaged background obtained in a 1 $\mu$s region centered around 5.2 us (divided by 10). (b) Quantum key distribution rate vs mean photon number and quantum bit error rate. Color bar represents the key rate. The line intersecting light blue and dark blue (negative key rate area) corresponds to the boundary for the positive key rate. The white dots indicate the regime of bare quantum memory and noise-free memory regimes.

tum level, thereby creating limits to the achievable QBER. As we extensively discussed on Chapter 2, in our EIT configuration the single-photon level background mechanism is produced by several non-linear effects. Figure 5.5a shows the results of a one-rail experiment including the extra-repumper (light-blue). We can see that after retrieval, the two dark-state-polariton interaction creates regions without the additional background noise. In this experiment the auxiliary field strength is increased to highlight the noise-free regions. We measured a SBR $\sim 26$ for an input $\langle n \rangle \sim 1.3$ photons. We can then infer a corresponding fidelity of 97% and QBER's $\sim 3\%$ for $\langle n \rangle \sim 1$ (see caption in Fig. 5.5). Another important effect of this technique is the increase of the efficiency at single photon level when there is no limitation on the power of control field used for retrieving the photons. Increasing the control field power boosts up the storage efficiency to 30-50% without affecting the noise-free regions.

The relevance of this new regime of operation is highlighted by analyzing its consequences in the achievable quantum key distribution rate ($\underline{\mathrm{R}}$) per channel efficiency for sharing random secret key, encoded in random polarization states, between Alice and Bob. $\underline{\mathrm{R}}$ depends on the quantum bit error rate (QBER) and the mean photon number $\mu$. In the infinite key length limit, it is given by: $R = \mu(e^{-\mu}(1 - H(Q_X)) - H(Q_Z)f(Q_Z))$, where $Q_X$ and $Q_Z$ are the QBERs, $H(x)$ is the binary Shannon entropy function and $f(Q_Z)$ is the efficiency of the classical error correction protocol. We have evaluated the absolute key rate vs. the input photon number and our average QBER with $f(Q_Z)$=1.05 [163] for two cases. In the first case we include the bare quantum memory operation ($QBER = 11.9\%$ for $\mu = 1.6$). Fig. 5.5b shows that this regime lies

just outside of the region for positive key rate generation, indicating not fully-secure qubit communication. This situation is fully-corrected by applying the noise reduction techniques explained above, as in this new regime the operation ($QBER = 3\%$ for $\mu = 1$) is well inside the secure communication threshold. This is a very important achievement as our quantum network has all the elementary capabilities for quantum cryptography operation.

### 5.4.2 Fully-portable quantum memory operation.

In order to boost the achieved quantum network operation towards all-environment qubit connections between distant isolated locations, portable and robust quantum memories are paramount. In our last experiment we show the storage of single-photon level qubits in a first-prototype of a fully-portable plug-and-play memory. This prototype has the same features of the designs used in our aforementioned experiments but is fully independent of laboratory infrastructure as it only requires the probe photons and an EIT control field as inputs. It also possesses a miniaturized version of the filtering system with independent temperature controllers. A detailed depiction of the portable memory is shown in Fig. 5.6a. In Fig. 5.6b we show a storage of light experiment in which we store pulses with a mean photon number $\langle n \rangle \sim 2$, in a single-rail experiment, corresponding to a SBR of 7.2.

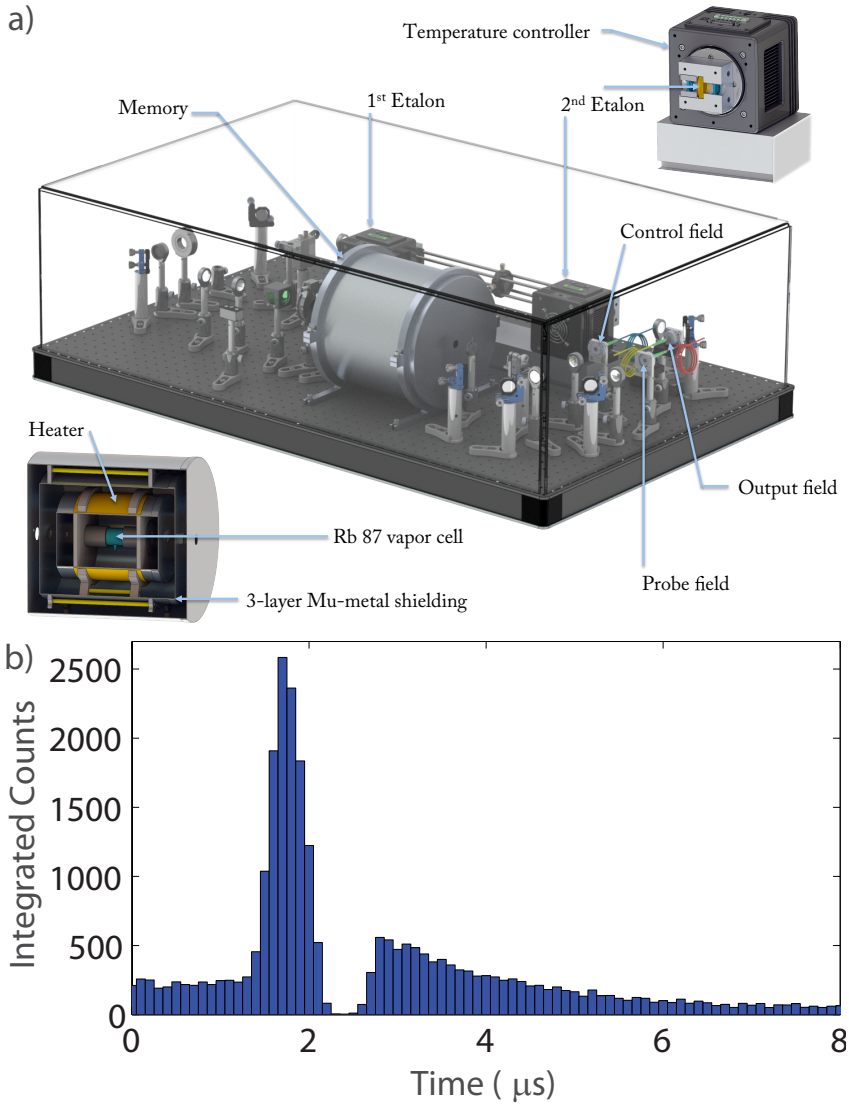


Figure 5.6: a) Prototype of a room temperature portable quantum memory. Upper-right inset: Detail of one of the frequency filtering units, including the silica etalon, isolation oven, temperature control cold-plate and PID temperature regulation circuitry. Bottom-left inset: Detail of the interaction zone including the Rb cell, temperature control electronics and three-layer magnetic shielding. b) Storage of single-photon level light pulses in the portable quantum memory.

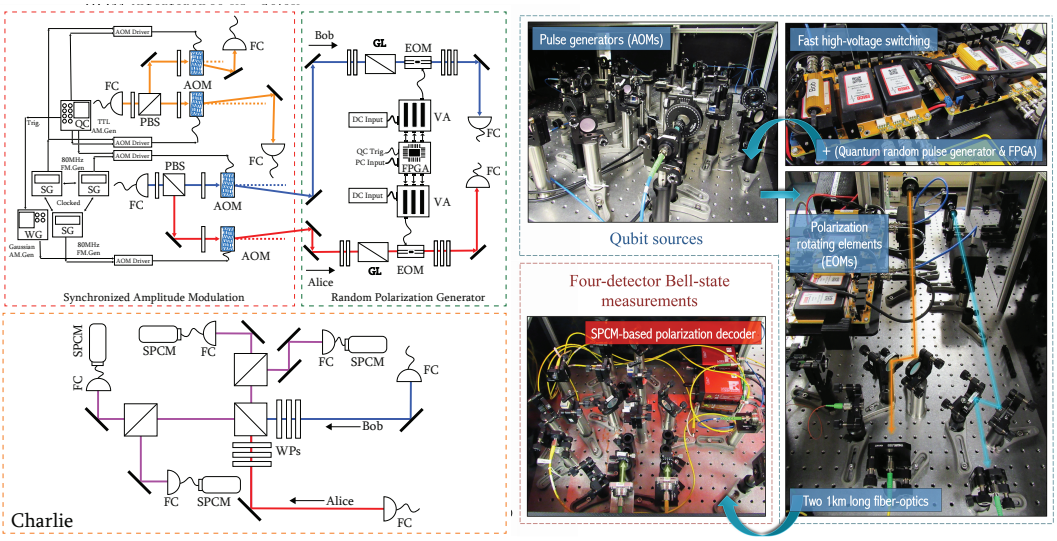


Figure 5.7: The experimental scheme of our MDI-QKD network. Alice and Bob generate randomized polarization qubits at Lab I while Charlie at Lab II reports back the result of the quantum interference measurement to both parties.

## 5.5 Towards Memory-Assisted MDI-QKD Systems

So far our quantum system consisted of quantum modules for a BB84 protocol with an integrated quantum memory module. As explained above, BB84 starts with Alice generating a random sequence of polarized qubits and ends with Bob measuring the arriving qubits in randomly selected polarization bases. This protocol suffers from two major weaknesses. The security of the network is conditioned upon perfect Alice and Bob stations. Although it is possible to create true random string of qubits with a near unity fidelity ( In our case an average fidelity of 99.5%), the average efficiency of single photon counters is still well below 90% (57% for the SPCMs in our lab). Such low efficiency

detectors jeopardize the security of the network even if the protocol is implemented perfectly. The other major issue with BB84 is its susceptibility to the losses in optical fibers, preventing the secure links to be established beyond 100km at telecom wavelength.

Both of these challenges can be resolved by a protocol known as Measurement-Device-Independent QKD [164, 165]. In this protocol both Alice and Bob generate their own random string of qubits which they then transmit to a public measuring station, Charlie. Charlie (which does not need to be in a secured location) then does a Bell-State measurement on the simultaneously arriving photons using a four-SPCM configuration (see fig. 5.7) and publicly announces the measured Bell states. By knowing these states and upon establishing a classical communication link, Alice and Bob can securely reconstruct the key generated by each party and ensure the security of the network. In this protocol, not only does Charlie not need to have access to perfect photon counters, due to the symmetries of the protocol structure Alice and Bob can use techniques such as entanglement swapping to overcome the optical fiber loss. Since Charlie requires both qubits to arrive simultaneously, quantum memories can play a major role by providing the synchronization buffer time the system needs. In fact, quantum memories alone, without the need of entanglement sources, can double the secure distance between Alice and Bob by synchronizing the qubits which are successfully transmitted over the long fibers.

We have developed all the infrastructure needed for implementing an MDI-QKD system (see fig. 5.7) along with two fully functional dual-rail quantum

memories to assist the network (see fig. 4.7 and 4.9). Furthermore, we already demonstrated a maximum quantum connectivity between Alice, Bob, Charlie and both quantum memories(see section 4.2). We estimate the realization of our memory-assisted MDI-QKD network by the end of fall 2018.

## 5.6 Summary

In conclusion, we have shown for a first time a system of quantum devices in which breakthrough operational capabilities are possible. We have achieved the first proof of principle combination of free-space propagation of random single-photon level polarization qubits and their storage and retrieval in a room temperature quantum memory. These results effectively constitute the quantum part of the BB84 protocol with the addition of a quantum memory. Furthermore we have shown noise-suppression techniques that allow our network to operate in a regime useful for quantum cryptographic communication with low QBER's. We have also shown the development of the structure needed for a double-memory MDI-QKD network. Together, all these capabilities pave the way for more sophisticated applications using a network of portable quantum memories.

Lastly, we demonstrated how these memories can be designed to be portable to operate outside a laboratory environment. The performance of our envisioned applications will benefit from a continuous development of our portable technology, including an increase in the speed (bandwidth) of the memory

together with shorter pulse duration and an increase in the success rate of the storage procedure by means of heralding. These chapters cover our efforts towards designing a platform for scalable room temperature quantum processing networks using EIT-based light-matter interfaces. For the first time to our knowledge, high performance quantum nodes are integrated in networks with high quantum connectivity between them, paving the path for scaling up the networks to many more quantum nodes. In the next and final chapter, we will briefly overview the directions for expanding these networks and their many potential applications.

# Chapter 6

# Outlook

Throughout this dissertation and since the spring of 2013, we have been following a very specific goal, to not only realize various quantum operations at room-temperature, but also develop a platform using which all these operations can come together in the form of a quantum system. Two of the most known examples of quantum systems are quantum simulators and quantum repeaters. Each of these systems can realize capabilities that are unmatched by any classical technology. For instance, quantum repeaters are the missing ingredient of intercontinental quantum communication and have the potential of revolutionizing the current telecommunications technology into a fully-secured hack-proof infrastructure. Such quantum networks can be also used to evolve many other technological fields such as autonomous vehicles and block-chains. Even though for long-distance applications we need to able to mass produce many quantum repeater nodes, each node on its own is a very complex system of several quantum modules. Two entanglement sources, four quantum

memories, (possibly) eight quantum frequency converters and a (potentially deterministic) Bell-state measuring (BSM) module, all working together in perfect harmony for a quantum repeater to beat the optical fiber losses. The main focus of this dissertation was on development of atomic quantum memories and their quantum connectivity between each other and other electro-optical quantum modules. Parallel to these efforts, our lab has been working on the other modules required in a quantum repeater: entanglement sources, frequency converters and phase-phase modulators to herald the memories and potentially be used in the design of a deterministic BSM module.

In this final chapter, we will briefly review the aforementioned devices and end the thesis by discussing the road-map ahead for developing a quantum system as complex as a quantum repeater at room-temperature.

## 6.1 Universal Set of Quantum Devices at Room-Temperature

We have in depth described the experimental realization of quantum memories and quantum simulators as two key modules of major quantum systems. There are other nodes currently under development, all with the outlook of joining our quantum network prototyping experiments together. We have recently demonstrated single photon-level cross-phase modulation operations at room temperature based on the same EIT platform. We have characterized the quantum states of pi-phase-shifted single-photon-level pulses in a double lambda closed-loop system [166, 167]. For particular choices in control field

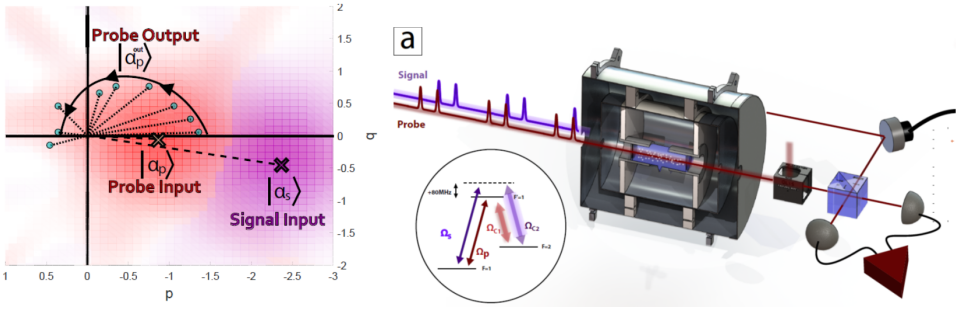


Figure 6.1: (left) Illustration of the output probes' Wigner function motion in phase space as the systems input phase is changed, triggered by a single photon level signal field.(right) A rendering of a room-temperature few-photon level phase gate. (Inset) Closed loop double-lambda system.

strength and input phase, the fidelity of the reconstructed quantum state can reach higher than 90% while having a pi-radians phase shift with respect to an original reference [168] (see Fig. 6.1). This node can enable the realization of several key technologies such as heralded quantum memories, deterministic Bell-State measuring devices and possibly a single photon level phase-phase quantum gate.

It is more beneficial to operate at telecom wavelengths (1300-1500nm) in order to maximize the transmission distances with a minimum number of quantum devices. Having low-noise light-matter interfaces in which quantized fields can be manipulated is the perfect spring board towards designing single photon frequency converters under EIT conditions [169]. We have recently achieved the wavelength conversion between the rubidium D1 and D2 lines through the use of adiabatic transfer using double-lambda schemes (see Fig. 6.2a) with a conversion of ∼10% for classical input pulses.

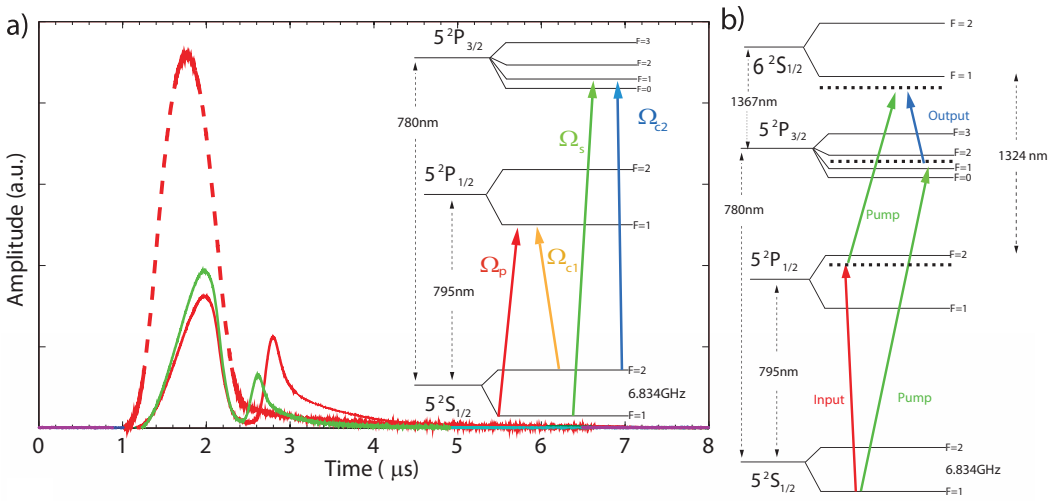


Figure 6.2: (a) Frequency conversion between the Rb D1 and D2 lines after storage and retrieval with different control fields (795nm: solid yellow, 780 nm: solid blue). Input: dashed red, 795nm: solid red, 780nm: solid green. Inset: Double-lambda configuration used to drive the adiabatic conversion, (b) atomic diamond scheme to achieve conversion from 795nm (solid red) to 1367nm (solid blue) using pump I at 780 nm and pump II at 1324nm (solid green).

As the next step, to create the essential photons at telecommunication wavelengths, nonlinear down conversion can be employed in rubidium using a diamond scheme [170]. This system requires a photon input at 795nm, and two pumps at 780 and 1324nm in order to generate a photon at a telecommunication wavelength of 1367nm (see Fig. 6.2b). Such a device can be developed and optimized in a table-top rubidium cell setups at the single-photon-level for reversible inputs at 795nm or 1367nm [171, 170, 172, 173, 174, 169, 175, 176].

Our lab has been also developing single photon sources tuned to Rb transitions based on Spontaneous Parametric Down-Conversion. The bow-tie cavity

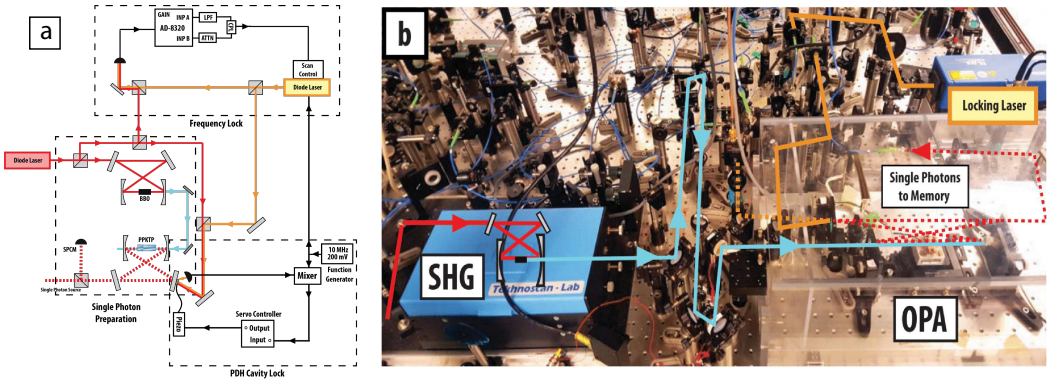


Figure 6.3: (a) The blueprint of a narrow-band quantum source tuned to Rb transitions, and (b) the experimental setup involving the OPA, bow-tie cavity and the locking system.

is pumped with 397.5nm light produced from a Second Harmonic Generation cavity (see fig. 6.3). The cavity is then stabilized using both a Pound-Drever-Hall and a frequency-lock ensuring emission at the right wavelength. The obtained narrow 2MHz cavity linewidth provides the spectral requirements on photons that are coupled to electromagnetically-induced transparency (EIT) based atomic experiments. By replacing the crystal inside the cavity with type II periodically poled non-linear crystals, the source can produce entangled photons within EIT bandwidth.

## 6.2 Realizing Many-Devices Quantum Systems

So far we have accomplished several milestone to realize a quantum system as complex as a repeater node. Development of the quantum memories, implementing networks of multi-memories, demonstrating systems of two memory

interference and memory-assisted QKD were a few of the necessary milestones to achieve before scaling up the network. In this final section we discuss the path ahead and the proposed technological advancements and mile-stones which need to be achieved to realize such quantum system.

### 6.2.1 Performance Improvements

Each quantum repeater requires four dual-rail quantum memories to allow enough buffer time for the synchronization of two entanglement sources. Throughout these years we have built four single-photon-level qubit memories operational systems (two stationary and two portable modules). These memories will be the foundation of a first table-top quantum repeater prototype. In order to attain the performance thresholds required for quantum repeater operation, we have identified key areas of further development: a) millisecond storage times, b) heralded operation and c) fast-duty-cycle operation.

The lifetime of the ground-state spin coherence is a crucial physical parameter that determines the achievable storage time [177]. One approach to increase this lifetime is the addition of a buffer gas with a low collisional depolarization cross-section ($N_2$, He). As we showed in section 2.4.2, we have already achieved storage times of $\sim 50$ $\mu$s at the few-photon-level by exploring different buffer gas pressures; we foresee increasing this to hundreds of micro-seconds by addressing cleaner lambda configurations in the atomic vapor. Additionally, adding anti-relaxation coatings to the interior cell walls will bring the storage times to $\sim 1$ ms [152].

Heralding a single-photon-generated spin wave increases the chances of performing entanglement swapping despite having non-unitary storage efficiencies. It is possible to herald our quantum memories by combining the qubit detection capabilities of our current setups together with homodyne state tomography of a heralding field [27, 168]. This approach is based upon our recent results presented in section 6.1. We envision to use the change in the quadrature and phase of a heralding field caused by the presence of a stored photon as a heralding event (see Fig. 6.1). The time tag of this measurement can be used to post-select the successful retrieval of the stored photon. We plan to develop the tools to analyse the quadrature changes in a real-time, in a shot-by-shot fashion. Not only is this scheme novel but its application for a quantum repeater will address the outstanding remaining challenge of improving the effective entanglement generation-rate after the memories [178, 179, 180].

Finally, increasing the duty cycle of our room-temperature devices relies upon increasing the speed (bandwidth) of the memory and decreasing the initial qubit pulse duration. This can be achieved by transferring the atomic configuration from on-resonance EIT to a high-bandwidth ($\sim$ 1 GHz) off-resonant Raman type. Within these settings it is possible to store ns-long pulses with repetition rates of $\sim$100MHz [182, 181, 183, 184, 185].

### 6.2.2 Technological Milestones

Using the optimized table-top quantum memories and entanglement sources, our lab should be able to explore the interconnection of many devices. In doing

so they will create elementary quantum networks aiming to tailor the functionalities required for quantum repeater operation. It is better to continue these experiments by operating at Rb wavelengths and finally incorporate the frequency converters to achieve operation at telecom wavelengths.
The next step is to intergrate an entanglement source into an experiment where each photon of the entangled pair is stored in an independent quantum memory. The preservation of entanglement will be tested after synchronizing the retrieval of the photons from the two memories and verifying their non-classical correlations [186, 187, 188, 189].

Another Milestone to achieve is to expand the experiments performed in Chapter 4 to a quantum network of four quantum memories in a quantum repeater node configuration. The first experiment sould oversee the realization of entanglement-assisted MDI-QKD by storing entanglement in two memories and random streams of qubits in the remaining two memories [190, 191]. This should be followed by experiments in which two EPR pairs are stored in two pairs of quantum memories. Successful storage and retrieval of the two entangled states will allow preliminary experiments on entanglement swapping.

Developing these networks will allow the group to understand the scaling laws of quantum networks and the main parameters involved in defining an optimal long-distant quantum communication channel. Developing scaling laws of communication in quantum networks requires to define what are the limiting factors in scaling these networks and how to formulate them. For instance,

it should be possible to experimentally verify that in quantum networks, the network capacity will be a function of the number of quantum memories each node has. Additionally, the quantum channel deteriorates as the flying time of the photons within the channel becomes longer than the available storage time at each amplification node.

Given the developments in the quantum network systems outlined above, the remaining technological milestone to achieve full network functionality is the creation of highly non-linear atomic systems in which photons retrieved on-demand from the quantum memories are made to interact, in order to create entangling operations. Provided our capability to create nonlinear systems in rubidium vapor (see section 6.1), the current experiments can be pushed to also include photon-photon operation. The key aspect of these new experiments will be the creation of double-lambda systems in which two single-photon-level fields can be made to cross-talk. The goal should be to maximize the phase shift at the single-photon level. Such a quantum repeater optical network presents a natural testbed for realizing multi-photon entangled states (GHZ states) by replacing the BSM station with an entangling quantum gate. Figure 6.4 shows the vision for a hybrid quantum network that combines all elements that the QIT lab is in the process of building and/or optimizing, including table-top entanglement generation, integrated frequency conversion units, portable quantum memories and a quantum gate for entangling operations.

The main advantage of developing these quantum repeater nodes is the fact

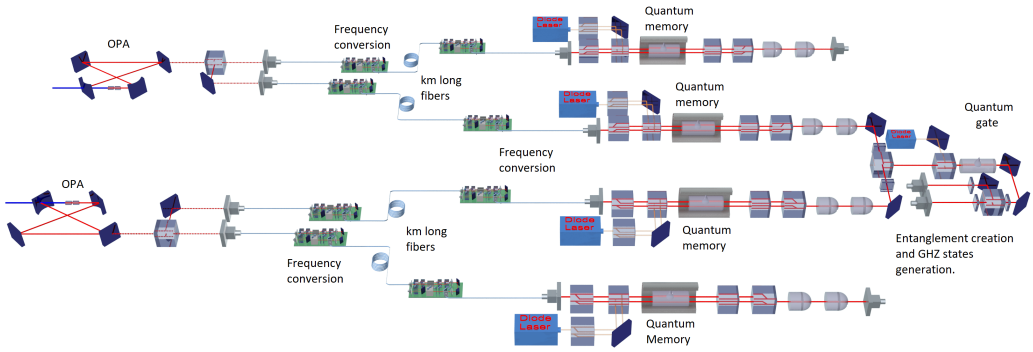


Figure 6.4: A hybrid network for the generation of multi-photon GHZ states. The network includes Rb-tuned entanglement sources, integrated frequency conversion units, portable quantum memories and an entangling gate.

that these nodes are based on the same platform as our quantum simulation and phase-phase modulation devices. Commercial quantum repeater nodes will not only allow the realization of a nationwide quantum-secured network but also provide the infrastructure needed for creating a neural network of quantum processing units that are already chained to each other to be used as a global quantum computer.

# Bibliography


[1] K. Heshami, D. G. England, P. C. Humphreys, P. J. Bustard, V. M. Acosta, J. Nunn, and B. J. Sussman, Quantum memories: emerging applications and recent advances, J. Mod. Opt. **63**, 2005 (2016).

[2] H. J. Kimble, Nature **453**, 1023 (2008).

[3] A. I. Lvovsky, B. C. Sanders and W. Tittel, Nature Photonics **3**, 706 (2009).

[4] Bussières, F., Sangouard, N., Afzelius, M., de Riedmatten, H., Simon, C., and Tittel, W., Prospective applications of optical quantum memories,Journal of Modern Optics **60**, 1519 (2013).

[5] Northup, T. E. and Blatt, R., Quantum information transfer using photons, Nat Photon **8**, 356 (2014).

[6] X. F. Xu, X. H. Bao and J. W. Pan, Phys. Rev. A **86**, 050304 (2012).

[7] C. Monroe et al., Phys. Rev. A **89,** 022317 (2014).

[8] L. M. Duan, M. D. Lukin, J. I. Cirac and P. Zoller, Nature **414,** 413 (2001).

[9] I. Novikova, R. L. Walsworth and Y. Xiao, Laser and Photonics Reviews **6,** 333-353 (2012).

[10] P. C. Maurer et al., Science **336,** 1283 (2012).

[11] K. Saeedi et al., Science **342,** 830 (2013).

[12] K. F. Reim et al., Phys. Rev. Lett. **107,** 053603 (2011).

[13] M. Hosseini, G. Campbell, B. M. Sparkes, P. K. Lam, and B. C. Buchler, Unconditional room-temperature quantum memory, Nat. Phys. **7**, 794 (2011).

[14] M. R. Sprague, P. S. Michelberger, T. F. M. Champion, D. G. England, J. Nunn, X.-M. Jin, W. S. Kolthammer, A. Abdolvand, P. S. J. Russell, and I. A. Walmsley, Broadband single-photon-level memory in a hollow-core photonic crystal fibre, Nat. Photonics **8**, 287 (2014).

[15] T. Baluktsian et al., Opt. Lett. **35,** 1950 (2010).

[16] G. Ghosh et al., Phys. Rev. Lett. **97,** 023603 (2006).

[17] P. Londero et al., Phys. Rev. Lett. **103,** 043602 (2009).

[18] V. Venkataraman, K. Saha and A. L. Gaeta, Nat. Phot. **7,** 138 (2013).

[19] M. Hosseini et al., Nature Physics **7,** 794 (2011).

[20] K. F. Reim et al., Nature Photonics **4,** 218 (2010).

[21] J. Appel, E. Figueroa, D. Korystov, M. Lobino and A. I. Lvovsky, Phys. Rev. Lett. **100**, 093602 (2008).

[22] K. Honda, D. Akamatsu, M. Arikawa, Y. Yokoi, K. Akiba, S. Nagatsuka, T. Tanimura, A. Furusawa and Mikio Kozuma, Phys. Rev. Lett. **100**, 093601 (2008).

[23] P. S. Michelberger, T. F. M. Champion, M. R. Sprague, K. T. Kaczmarek, M. Barbieri, X. M. Jin, D. G. England, W. S. Kolthammer, D. J. Saunders, J. Nunn and I. A. Walmsley, arXiv:1405.1470 (2014).

[24] D. G. England, K. A. G. Fisher, J. P. W. MacLean, P. J. Bustard, R. Lausten, K. J. Resch, B. J. Sussman, arXiv:1409.2892 (2014).

[25] Y. W. Cho and Y. H. Kim, Opt. Exp. **18,** 25786 (2010).

[26] D. G. England et al., J. Phys. B: At. Mol. Opt. Phys. **45,** 124008 (2012).

[27] C. Kupchak, T. Mittiga, B. Jordaan, M. Namazi, C. Noelleke and Eden Figueroa, Nature Scientific Reports **5**, 7658 (2015).

[28] Briegel, H.-J., Dür, W., Cirac, J. I., and Zoller, P., Quantum Repeaters: The Role of Imperfect Local Operations in Quantum Communication, Physical Review Letters **81**, 5932 (1998).

[29] Dür, W., Briegel, H.-J., Cirac, J. I., and Zoller, P., Quantum repeaters based on entanglement purification, Physical Review A **59**, 169 (1999).

[30] Reiserer, A. and Rempe, G., Cavity-based quantum networks with single atoms and optical photons, Rev. Mod. Phys. **87**, 1379 (2015).

[31] Heshami, K., England, D. G., Humphreys, P. C., Bustard, P. J., Acosta, V. M., Nunn, J., and Sussman, B. J., Quantum memories: emerging applications and recent advances, Journal of Modern Optics **63**, 2005 (2016).

[32] Kimble, H. J., The quantum internet, Nature **453**, 1023 (2008).

[33] Muralidharan, S., Li, L., Kim, J., Lütkenhaus, N., Lukin, M. D., and Jiang, L., Optimal architectures for long distance quantum communication, Scientific Reports **6**, 20463 (2016).

[34] Bernardes, N. K., Praxmeyer, L., and van Loock, P., Rate analysis for a hybrid quantum repeater, Physical Review A **83**, 012323 (2011).

[35] Razavi, M., Piani, M., and Lütkenhaus, N., Quantum repeaters with imperfect memories: Cost and scalability, Physical Review A **80**, 032301 (2009).

[36] Yuan, Z.-S., Chen, Y.-A., Zhao, B., Chen, S., Schmiedmayer, J., and Pan, J.-W., Experimental demonstration of a BDCZ quantum repeater node, Nature **454**, 1098 (2008).

[37] Sangouard, N., Simon, C., de Riedmatten, H., and Gisin, N., Quantum repeaters based on atomic ensembles and linear optics, Reviews of Modern Physics **83**, 33 (2011).

[38] Uphoff, M., Brekenfeld, M., Rempe, G., and Ritter, S., An integrated quantum repeater at telecom wavelength with single atoms in optical fiber cavities, Applied Physics B **122**, 46 (2016).

[39] Yang, S.-J., Wang, X.-J., Bao, X.-H., and Pan, J.-W., An efficient quantum light–matter interface with sub-second lifetime, Nature Photonics **10**, 381 (2016).

[40] Duan, L.-M., Lukin, M. D., Cirac, J. I., and Zoller, P., Long-distance quantum communication with atomic ensembles and linear optics, Nature **414**, 413 (2001), 17.

[41] Reim, K. F., Michelberger, P., Lee, K. C., Nunn, J., Langford, N. K., and Walmsley, I. A., Single-photon-level quantum memory at room temperature, Phys. Rev. Lett. **107**, 053603 (2011).

[42] Reim, K. F., Nunn, J., Lorenz, V. O., Sussman, B. J., Lee, K. C., Langford, N. K., Jaksch, D., and Walmsley, I. A., Towards high-speed optical quantum memories, Nat Photon **4**, 218 (2010).

[43] Michelberger, P. S., Champion, T. F. M., Sprague, M. R., Kaczmarek, K. T., Barbieri, M., Jin, X. M., England, D. G., Kolthammer, W. S., Saunders, D. J., Nunn, J., and Walmsley, I. A., Interfacing ghz-bandwidth heralded single photons with a warm vapour raman memory, New Journal of Physics **17**, 043006 (2015).

[44] Fleischhauer, M. and Lukin, M. D., Dark-State Polaritons in Electromagnetically Induced Transparency, Physical Review Letters **84**, 5094 (2000).

[45] A. Datta, L. Zhang, J. Nunn, N. K. Langford, A. Feito, M. B. Plenio, and I. A. Walmsley, Compact Continuous-Variable Entanglement Distillation, Phys. Rev. Lett. **108**, 060502 (2012).

[46] P. Kómár, E. M. Kessler, M. Bishof, L. Jiang, A. S. Sørensen, J. Ye, and M. D. Lukin, A quantum network of clocks, Nat. Phys. **10**, 582 (2014), 2.

[47] A. I. Lvovsky, B. C. Sanders, and W. Tittel, Optical quantum memory, Nat. Photonics **3**, 706 (2009).

[48] F. Bussières, N. Sangouard, M. Afzelius, H. de Riedmatten, C. Simon, and W. Tittel, Prospective applications of optical quantum memories, J. Mod. Opt. **60**, 1519 (2013).

[49] T. E. Northup and R. Blatt, Quantum information transfer using photons, Nat. Photonics **8**, 356 (2014).

[50] A. Reiserer and G. Rempe, Cavity-based quantum networks with single atoms and optical photons, Rev. Mod. Phys. **87**, 1379 (2015).

[51] K. C. Lee, M. R. Sprague, B. J. Sussman, J. Nunn, N. K. Langford, X.-M. Jin, T. Champion, P. Michelberger, K. F. Reim, D. England, D. Jaksch, and I. A. Walmsley, Entangling Macroscopic Diamonds at Room Temperature, Science **334**, 1253 (2011).

[52] K. Bader, D. Dengler, S. Lenz, B. Endeward, S.-D. Jiang, P. Neugebauer, and J. van Slageren, Room temperature quantum coherence in a potential molecular qubit, Nat. Commun. **5**, 5304 (2014).

[53] N. Yao, L. Jiang, A. Gorshkov, P. Maurer, G. Giedke, J. Cirac, and M. Lukin, Scalable architecture for a room temperature solid-state quantum information processor, Nat. Commun. **3**, 800 (2012).

[54] H. Krauter, D. Salart, C. A. Muschik, J. M. Petersen, H. Shen, T. Fernholz, and E. S. Polzik, Deterministic quantum teleportation between distant atomic objects, Nat. Phys. **9**, 400 (2013).

[55] K. F. Reim, P. Michelberger, K. C. Lee, J. Nunn, N. K. Langford, and I. A. Walmsley, Single-Photon-Level Quantum Memory at Room Temperature, Phys. Rev. Lett. **107**, 053603 (2011).

[56] S. Manz, T. Fernholz, J. Schmiedmayer, and J.-W. Pan, Collisional decoherence during writing and reading quantum states, Phys. Rev. A **75**, 040101 (2007).

[57] N. B. Phillips, A. V. Gorshkov, and I. Novikova, Light storage in an optically thick atomic ensemble under conditions of electromagnetically induced transparency and four-wave mixing, Phys. Rev. A **83**, 063823 (2011).

[58] M. Bashkansky, F. K. Fatemi, and I. Vurgaftman, Quantum memory in warm rubidium vapor with buffer gas, Opt. Lett. **37**, 142 (2012).

[59] I. Vurgaftman and M. Bashkansky, Suppressing four-wave mixing in warm-atomic-vapor quantum memory, Phys. Rev. A **87**, 063836 (2013).

[60] L. Karpa, F. Vewinger, and M. Weitz, Resonance Beating of Light Stored Using Atomic Spinor Polaritons, Phys. Rev. Lett. **101**, 170406 (2008).

[61] S. Riedl, M. Lettner, C. Vo, S. Baur, G. Rempe, and S. Dürr, Bose-Einstein condensate as a quantum memory for a photonic polarization qubit, Phys. Rev. A **85**, 022318 (2012).

[62] H. P. Specht, C. Nlleke, A. Reiserer, M. Uphoff, E. Figueroa, S. Ritter, and G. Rempe, A single-atom quantum memory, Nature **473**, 190 (2011).

[63] D. Saunders, J. Munns, T. Champion, C. Qiu, K. Kaczmarek, E. Poem, P. Ledingham, I. Walmsley, and J. Nunn, Cavity-Enhanced Room-Temperature Broadband Raman Memory, Phys. Rev. Lett. **116**, 090501 (2016).

[64] J. Wolters, G. Buser, A. Horsley, L. Bguin, A. Jckel, J.-P. Jahn, R. J. Warburton, and P. Treutlein, Simple Atomic Quantum Memory Suitable

for Semiconductor Quantum Dot Single Photons, Phys. Rev. Lett. **119**, 060502 (2017).

[65] J.-P. Dou, A.-l. Yang, M.-Y. Du, D. Lao, J. Gao, L.-F. Qiao, H. Li, X.-L. Pang, Z. Feng, H. Tang, and X.-M. Jin, A Broadband DLCZ Quantum Memory in Room-Temperature Atoms, arXiv 1704.06309 (2017).

[66] K. T. Kaczmarek, P. M. Ledingham, B. Brecht, S. E. Thomas, G. S. Thekkadath, O. Lazo-Arjona, J. H. D. Munns, E. Poem, A. Feizpour, D. J. Saunders, J. Nunn, and I. A. Walmsley, A room-temperature noise-free quantum memory for broadband light, arXiv 1704.00013 (2017).

[67] R. Finkelstein, E. Poem, O. Michel, O. Lahad, and O. Firstenberg, Fast, noise-free memory for photon synchronization at room temperature, arXiv 1708.01919 (2017).

[68] Cirac, J. I. and Zoller, P., Goals and opportunities in quantum simulation, Nat Phys **8**, 264 (2012).

[69] Bloch, I., Dalibard, J., and Nascimbene, S., Photonic quantum simulators, Nat Phys **8**, 267 (2012).

[70] Blatt, R. and Roos, C. F., Quantum simulations with trapped ions, Nat Phys **8**, 277 (2012).

[71] Houck, A. A. e. a., On-chip quantum simulation with superconducting circuits, Nat Phys **8**, 292 (2012).

[72] Aspuru-Guzik, A. and Walther, P., Photonic quantum simulators, Nat Phys **8**, 285 (2012).

[73] Rechtsman, M. C., Zeuner, J. M., Plotnik, Y., Lumer, Y., Podolsky, D., Dreisow, F., Nolte, S., Segev, M., and Szameit, A., Photonic floquet topological insulators, Nature **496**, 196 (2013).

[74] Radnaev, A. G., Dudin, Y. O., Zhao, R., Jen, H. H., Jenkins, S. D., Kuzmich, A., and Kennedy, T. A. B., A quantum memory with telecom-wavelength conversion, Nat Phys **6**, 894 (2010).

[75] Jackiw, R. and Rebbi, C., Solitons with fermion number, Phys. Rev. D **13**, 3398 (1976).

[76] Unanyan, R. G., Otterbach, J., Fleischhauer, M., Ruseckas, J., Kudriašov, V., and Juzeliūnas, G., Spinor slow-light and dirac particles with variable mass, Phys. Rev. Lett. **105**, 173603 (2010).

[77] Liu, C., Dutton, Z., Behroozi, C. H., and Hau, L. V., Observation of coherent optical information storage in an atomic medium using halted light pulses, Nature **409**, 490 (2001).

[78] Phillips, D. F., Fleischhauer, A., Mair, A., Walsworth, R. L., and Lukin, M. D., Storage of Light in Atomic Vapor, Physical Review Letters **86**, 783 (2001).

[79] Fleischhauer, M., Imamoglu, A., and Marangos, J. P., Electromagnetically induced transparency: Optics in coherent media, Reviews of modern physics **77**, 633 (2005).

[80] Noh, C. and Angelakis, D. G., Quantum simulations and many-body physics with light, Rep. Prog. Phys. **80**, 016401 (2017).

[81] Lee, M.-J., Ruseckas, J., Lee, C.-Y., Kudriaov, V., Chang, K.-F., Cho, H.-W., Juzelinas, G., and Yu, I. A., Experimental demonstration of spinor slow light, Nature Communications **5**, 5542 (2014).

[82] Angelakis, D. G., Huo, M.-X., Chang, D., Kwek, L. C., and Korepin, V., Mimicking interacting relativistic theories with stationary pulses of light, Phys. Rev. Lett. **110**, 100502 (2013).

[83] Niemi, A. and Semenoff, G., Fermion number fractionization in quantum field theory, Phys. Rep. **135**, 99 (1986).

[84] Ruostekoski, J., Dunne, G., and Javanainen, J., Particle number fractionalization of an atomic fermi-dirac gas in an optical lattice, Phys. Rev. Lett. **88**, 180401 (2002).

[85] Javanainen, J. and Ruostekoski, J., Optical detection of fractional particle number in an atomic fermi-dirac gas, Phys. Rev. Lett. **91**, 150404 (2003).

[86] Witthaut, D., Salger, T., Kling, S., Grossert, C., and Weitz, M., Effective dirac dynamics of ultracold atoms in bichromatic optical lattices, Phys. Rev. A **84**, 033601 (2011).

[87] Salger, T., Grossert, C., Kling, S., and Weitz, M., Klein tunneling of a quasirelativistic bose-einstein condensate in an optical lattice, Phys. Rev. Lett. **107**, 240401 (2011).

[88] Leder, M., Grossert, C., Sitta, L., Genske, M., Rosch, A., and Weitz, M., Real-space imaging of a topologically protected edge state with ultracold atoms in an amplitude-chirped optical lattice (2016).

[89] Lamata, L., Casanova, J., Gerritsma, R., Roos, C. F., Garca-Ripoll, J. J., and Solano, E., Relativistic quantum mechanics with trapped ions, New Journal of Physics **13**, 095003 (2011).

[90] Grossert, C., Leder, M., and Weitz, M., Phase dependent loading of bloch bands and quantum simulation of relativistic wave equation predictions with ultracold atoms in variably shaped optical lattice potentials, Journal of Modern Optics **63**, 1805 (2016).

[91] Casanova, J., García-Ripoll, J. J., Gerritsma, R., Roos, C. F., and Solano, E., Klein tunneling and dirac potentials in trapped ions, Phys. Rev. A **82**, 020101 (2010).

[92] Gerritsma, R., Lanyon, B. P., Kirchmair, G., Zähringer, F., Hempel, C., Casanova, J., García-Ripoll, J. J., Solano, E., Blatt, R., and Roos, C. F., Quantum simulation of the klein paradox with trapped ions, Phys. Rev. Lett. **106**, 060503 (2011).

[93] Wilczek, F., Particle physics and condensed matter: the saga continues, Physica Scripta **2016**, 014003 (2016).

[94] Zhang, D.-W., Zhao, Y. X., Liu, R.-B., Xue, Z.-Y., Zhu, S.-L., and Wang, Z. D., Quantum simulation of exotic $\mathcal{PT}$-invariant topological nodal loop bands with ultracold atoms in an optical lattice, Phys. Rev. A **93**, 043617 (2016).

[95] Mugel, S., Celi, A., Massignan, P., Asbóth, J. K., Lewenstein, M., and Lobo, C., Topological bound states of a quantum walk with cold atoms, Phys. Rev. A **94**, 023631 (2016).

[96] Tan, W., Chen, L., Ji, X., and Lin, H.-Q., Photonic simulation of topological superconductor edge state and zero-energy mode at a vortex (2014).

[97] Iadecola, T., Schuster, T., and Chamon, C., Non-abelian braiding of light, Phys. Rev. Lett. **117**, 073901 (2016).

[98] Hasan, M. and Kane, C. L., Colloquium: Topological insulators., Rev. Mod. Phys. **82**, 3045 (2010).

[99] Qi, X. L. and Zhang, S. C., Topological insulators and superconductors., Rev. Mod. Phys. **83**, 1057 (2011).

[100] Yefsah, T., Sommer, A. T., Ku, M. J. H., Cheuk, L. W., Ji, W., Bakr, W. S., and Zwierlein, M. W., Heavy solitons in a fermionic superfluid, Nature **499**, 426 (2013).

[101] Angelakis, D. G., Das, P., and Noh, C., Probing the topological properties of the jackiw-rebbi model with light, Scientific Reports **4**, 6110 EP (2014).

[102] M. Namazi, T. Mittiga, C. Kupchak, and E. Figueroa, Cascading quantum light-matter interfaces with minimal interconnection losses, Phys. Rev. A **92**, 033846 (2015).

[103] Klein, O., Die reflexion von elektronen an einem potentialsprung nach der relativistischen dynamik von dirac, Zeitschrift für Physik **53**, 157 (1929).

[104] Chodos, A., Jaffe, R. L., Johnson, K., and Thorn, C. B., Baryon structure in the bag theory, Phys. Rev. D **10**, 2599 (1974).

[105] Semenoff, G., Matsumoto, H., and Umezawa, H., Fermion zero modes, supersymmetry, and charge fractionalization of quantum solitons, Phys. Rev. D **25**, 1054 (1982).

[106] Keil, R., Zeuner, J. M., Dreisow, F., Heinrich, M., Tünnermann, A., Nolte, S., and Szameit, A., The random mass Dirac model and long-range correlations on an integrated optical platform, Nature Communications **4**, 1368 (2013).

[107] Shankar, R., Renormalization-group approach to interacting fermions, Rev. Mod. Phys. **66**, 129 (1994).

[108] Thirring, W. E., A soluble relativistic field theory, Annals of Physics **3**, 91 (1958).

[109] K. S. Choi, A. Goban, S. B. Papp, S. J. van Enk and H. J. Kimble, Nature 468, 412 (2010).

[110] S. Ritter, C. Noelleke, C. Hahn, A. Reiserer, A. Neuzner, M. Uphoff, M. Muecke, E. Figueroa, J. Bochmann and G. Rempe, Nature 484, 195 (2012).

[111] G. Vittorini, D. Hucul, I. V. Inlek, C. Crocker, and C. Monroe, Phys. Rev. A 90, 040302(R) (2014).

[112] L.-M. Duan and C. Monroe, Rev. Mod. Phys. 82, 1209 (2010).

[113] S. Perseguers, G. J. Lapeyre, D Cavalcanti, M. Lewenstein and A. Acin, Rep. Prog. Phys. 76, 096001 (2013).

[114] J. Nunn,1, N. K. Langford, W. S. Kolthammer, T. F. M. Champion, M. R. Sprague, P. S. Michelberger, X.-M. Jin, D. G. England and I. A. Walmsley, Phys. Rev. Lett. 110, 133601 (2013).

[115] D. A. B. Miller, Nature Photonics 4, 3 (2010).

[116] Y. Cai, J. Feng, H. Wang, G. Ferrini, X. Xu, J. Jing and N. Treps, arXiv:1410.3672v2 (2014).

[117] L. Huang and Y. C. Lai, Chaos 21, 025107 (2011).

[118] L. Fan, K. Y. Fong, M. Poot and H. X. Tang, Nature Communications 6, 5850 (2015).

[119] G. T. Campbell, O. Pinel, M. Hosseini, T. C. Ralph, B. C. Buchler and P. K. Lam, Phys. Rev. Lett. 113, 063601 (2014).

[120] C. Monroe, R. Raussendorf, A. Ruthven, K. R. Brown, P. Maunz, L.-M. Duan and J. Kim, Phys. Rev. A 89, 022317 (2014).

[121] F. Bussieres, N. Sangouard, M. Afzelius, H. de Riedmatten, C. Simon, W. Tittel, J. Mod. Opt. 60, 1519 (2013).

[122] I. Novikova et al., Laser and Photonics Reviews 6, 333 (2012).

[123] P. S. Michelberger, T. F. M. Champion, M. R. Sprague, K. T. Kaczmarek, M. Barbieri, X. M. Jin, D. G. England, W. S. Kolthammer, D. J. Saunders, J. Nunn and I. A. Walmsley, arXiv:1405.1470v1 (2014).

[124] D. G. England, K. A. G. Fisher, J.P. W. MacLean, P. J. Bustard, R. Lausten, K. J. Resch and B. J. Sussman, arXiv:1409.2892v2 (2014).

[125] Namazi, M., Kupchak, C., Jordaan, B., Shahrokhshahi, R., and Figueroa, E., Ultralow-noise room-temperature quantum memory for polarization qubits, Phys. Rev. Applied **8**, 034023 (2017).

[126] I. Capraro, A. Tomaello, A. Dall'Arche, F. Gerlin, R. Ursin, G. Vallone, and P. Villoresi, Impact of Turbulence in Long Range Quantum and Classical Communications, Phys. Rev. Lett. **109**, 200502 (2012).

[127] G. Vallone, V. D'Ambrosio, A. Sponselli, S. Slussarenko, L. Marrucci, F. Sciarrino, and P. Villoresi, Free-Space Quantum Key Distribution by Rotation-Invariant Twisted Photons, Phys. Rev. Lett. **113**, 060503 (2014).

[128] G. Vallone, D. Bacco, D. Dequal, S. Gaiarin, V. Luceri, G. Bianco, and P. Villoresi, Experimental Satellite Quantum Communications, Phys. Rev. Lett. **115**, 040502 (2015).

[129] T. Schmitt-Manderbach, H. Weier, M. Fürst, R. Ursin, F. Tiefenbacher, T. Scheidl, J. Perdigues, Z. Sodnik, C. Kurtsiefer, J. G. Rarity, A. Zeilinger, and H. Weinfurter, Experimental Demonstration of Free-Space Decoy-State Quantum Key Distribution over 144 k Phys. Rev. Lett. **98**, 010504 (2007).

[130] S. Nauerth, F. Moll, M. Rau, C. Fuchs, J. Horwath, S. Frick, and H. Weinfurter, Air-to-ground quantum communication, Nat. Photonics **7**, 382 (2013).

[131] S. Ritter, C. Nölleke, C. Hahn, A. Reiserer, A. Neuzner, M. Uphoff, M. Mücke, E. Figueroa, J. Bochmann, and G. Rempe, An elementary quantum network of single atoms in optical cavities, Nature **484**, 195 (2012).

[132] K. S. Choi, A. Goban, S. B. Papp, S. J. van Enk, and H. J. Kimble, Entanglement of spin waves among four quantum memories, Nature **468**, 412 (2010).

[133] C. Nölleke, A. Neuzner, A. Reiserer, C. Hahn, G. Rempe, and S. Ritter, Efficient Teleportation Between Remote Single-Atom Quantum Memories, Phys. Rev. Lett. **110**, 140403 (2013).

[134] V. Scarani, H. Bechmann-Pasquinucci, N. J. Cerf, M. Dušek, N. Lütkenhaus, and M. Peev, The security of practical quantum key distribution, Rev. Mod. Phys. **81**, 1301 (2009).

[135] H.-K. Lo, M. Curty, and B. Qi, Measurement-device-independent quantum key distribution, Phys. Rev. Lett. **108**, 130503 (2012).

[136] D. Bacco, M. Canale, N. Laurenti, G. Vallone, and P. Villoresi, Experimental quantum key distribution with finite-key security analysis for noisy channels, Nat. Commun. **4** (2013).

[137] Y. Liu, T.-Y. Chen, L.-J. Wang, H. Liang, G.-L. Shentu, J. Wang, K. Cui, H.-L. Yin, N.-L. Liu, L. Li, X. Ma, J. S. Pelc, M. M. Fejer, C.-Z. Peng, Q. Zhang, and J.-W. Pan, Experimental measurement-device-independent quantum key distribution, Phys. Rev. Lett. **111**, 130502 (2013).

[138] Z. Tang, Z. Liao, F. Xu, B. Qi, L. Qian, and H.-K. Lo, Experimental Demonstration of Polarization Encoding Measurement-Device-Independent Quantum Key Distribution, Phys. Rev. Lett. **112**, 190503 (2014).

[139] S. Abruzzo, H. Kampermann, and D. Bruß, Measurement-device-independent quantum key distribution with quantum memories, Phys. Rev. A **89**, 012301 (2014).

[140] C. Panayi, M. Razavi, X. Ma, and N. Lütkenhaus, Memory-assisted measurement-device-independent quantum key distribution, New J. Phys. **16**, 043005 (2014).

[141] A. Reiserer and G. Rempe, Cavity-based quantum networks with single atoms and optical photons, Rev. Mod. Phys. **87**, 1379 (2015), 6.

[142] T. E. Northup and R. Blatt, Quantum information transfer using photons, Nat. Photonics **8**, 356 (2014), 5.

[143] F. Bussières, N. Sangouard, M. Afzelius, H. de Riedmatten, C. Simon, and W. Tittel, Prospective applications of optical quantum memories, J. Mod. Opt. **60**, 1519 (2013), 4.

[144] K. Heshami, D. G. England, P. C. Humphreys, P. J. Bustard, V. M. Acosta, J. Nunn, and B. J. Sussman, Quantum memories: emerging applications and recent advances, J. Mod. Opt. **63**, 2005 (2016).

[145] S. Riedl, M. Lettner, C. Vo, S. Baur, G. Rempe, and S. Dürr, Bose-Einstein condensate as a quantum memory for a photonic polarization qubit, Phys. Rev. A **85**, 022318 (2012).

[146] M. Gündoğan, P. M. Ledingham, A. Almasi, M. Cristiani, and H. de Riedmatten, Quantum Storage of a Photonic Polarization Qubit in a Solid, Phys. Rev. Lett. **108**, 190504 (2012).

[147] E. Saglamyurek, J. Jin, V. B. Verma, M. D. Shaw, F. Marsili, S. W. Nam, D. Oblak, and W. Tittel, Quantum storage of entangled telecom-wavelength photons in an erbium-doped optical fibre, Nat. Photonics **9**, 83 (2015).

[148] I. Novikova, R. Walsworth, and Y. Xiao, Electromagnetically induced transparency-based slow and stored light in warm atoms, Laser & Photonics Rev. **6**, 333 (2012).

[149] Y.-F. Hsiao, P.-J. Tsai, H.-S. Chen, S.-X. Lin, C.-C. Hung, C.-H. Lee, Y.-H. Chen, Y.-F. Chen, I. A. Yu, and Y.-C. Chen, EIT-based photonic memory with near-unity storage efficiency, arXiv preprint arXiv:1605.08519 (2016).

[150] M. Hosseini, B. M. Sparkes, G. Campbell, P. K. Lam, and B. C. Buchler, High efficiency coherent optical memory with warm rubidium vapour, Nat. Commun. **2**, 174 (2011).

[151] S.-J. Yang, X.-J. Wang, X.-H. Bao, and J.-W. Pan, An efficient quantum lightmatter interface with sub-second lifetime, Nat. Photonics **10**, 381 (2016).

[152] D. G. England, K. A. Fisher, J.-P. W. MacLean, P. J. Bustard, R. Lausten, K. J. Resch, and B. J. Sussman, Storage and Retrieval of THz-Bandwidth Single Photons Using a Room-Temperature Diamond Quantum Memory, Phys. Rev. Lett. **114**, 053602 (2015).

[153] D. Saunders, J. Munns, T. Champion, C. Qiu, K. Kaczmarek, E. Poem, P. Ledingham, I. Walmsley, and J. Nunn, Cavity-Enhanced Room-Temperature Broadband Raman Memory, Phys. Rev. Lett. **116**, 090501 (2016).

[154] D. Bouwmeester, A. Ekert, and A. Zeilinger, editors, The Physics of Quantum Information, Springer Berlin Heidelberg, Berlin, Heidelberg (2000), ISBN 978-3-642-08607-6 978-3-662-04209-0.

[155] J. I. Cirac, P. Zoller, H. J. Kimble, and H. Mabuchi, Quantum state transfer and entanglement distribution among distant nodes in a quantum network, Phys. Rev. Lett. **78**, 3221 (1997).

[156] H. J. Kimble, The quantum internet, Nature **453**, 1023 (2008), 16.

[157] A. Reiserer, N. Kalb, M. S. Blok, K. J. M. van Bemmelen, T. H. Taminiau, R. Hanson, D. J. Twitchen, and M. Markham, Robust quantum-network memory using decoherence-protected subspaces of nuclear spins, Phys. Rev. X **6**, 021040 (2016).

[158] F. Bussières, C. Clausen, A. Tiranov, B. Korzh, V. B. Verma, S. W. Nam, F. Marsili, A. Ferrier, P. Goldner, H. Herrmann, C. Silberhorn, W. Sohler, M. Afzelius, and N. Gisin, Quantum teleportation from a telecom-wavelength photon to a solid-state quantum memory, Nat. Photonics **8**, 775 (2014).

[159] L.-M. Duan, M. D. Lukin, J. I. Cirac, and P. Zoller, Long-distance quantum communication with atomic ensembles and linear optics, Nature **414**, 413 (2001), 17.

[160] G. Vallone, D. Dequal, M. Tomasin, F. Vedovato, M. Schiavon, V. Luceri, G. Bianco, and P. Villoresi, Interference at the Single Photon Level Along Satellite-Ground Channels, Phys. Rev. Lett. **116**, 253601 (2016).

[161] C. H. Bennett and G. Brassard, Quantum Cryptography: Public Key Distribution and Coin T in Proceedings of the IEEE International Conference on Computers, Systems and Signal Processing, Bangalore, India, 175, IEEE, New York (1984).

[162] D. Elkouss, J. Martinez-Mateo, and V. Martin, Information Reconciliation for Quantum Key Distribution, Quantum Inf. Comput. **11**, 0226 (2011).

[163] Mizutani, A., Tamaki, K., Ikuta, R., Yamamoto, T., and Imoto, N., Measurement-device-independent quantum key distribution for scarani-acin-ribordy-gisin 04 protocol, Scientific Reports **4**, 5236 EP (2014).

[164] Liu, Y., Chen, T.-Y., Wang, L.-J., Liang, H., Shentu, G.-L., Wang, J., Cui, K., Yin, H.-L., Liu, N.-L., Li, L., Ma, X., Pelc, J. S., Fejer, M. M., Peng, C.-Z., Zhang, Q., and Pan, J.-W., Experimental measurement-device-independent quantum key distribution, Phys. Rev. Lett.

[165] Artoni, M. and Zavatta, A., Large phase-by-phase modulations in atomic interfaces, Phys. Rev. Lett. **115**, 113005 (2015).

[166] Z. Liu, Y. Chen, Y. Chen, H. Lo, P. Tsai, I. A. Yu, Y.-C. Chen, Y.-F. Chen, Large Cross-Phase Modulations at the Few-Photon Level, Phys. Rev. Lett. **117**, 203601 (2016).

[167] Reihaneh Shahrokhshahi, Steven Sagona-Stophel, Bertus Jordaan, Mehdi Namazi and Eden Figueroa, Room temperature conditional pi-phase shifts mediated by simultaneously propagating single-photon level pulses, arXiv:1803.07012 (2018).

[168] Vewinger, F., Appel, J., Figueroa, E., and Lvovsky, A. I., Adiabatic frequency conversion of optical information in atomic vapor, Opt. Lett. **32**, 2771 (2007).

[169] Radnaev, A. G., Dudin, Y. O., Zhao, R., Jen, H. H., Jenkins, S. D., Kuzmich, A., and Kennedy, T. A. B., A quantum memory with telecom-wavelength conversion, Nat Phys **6**, 894 (2010).

[170] Chanelière, T., Matsukevich, D. N., Jenkins, S. D., Kennedy, T. A. B., Chapman, M. S., and Kuzmich, A., Quantum telecommunication based on atomic cascade transitions, Phys. Rev. Lett. **96**, 093604 (2006).

[171] Willis, R. T., Becerra, F. E., Orozco, L. A., and Rolston, S. L., Four-wave mixing in the diamond configuration in an atomic vapor, Phys. Rev. A **79**, 033814 (2009).

[172] Gomez, E., Baumer, F., Lange, A. D., Sprouse, G. D., and Orozco, L. A., Lifetime measurement of the 6 s level of rubidium, Physical Review A **72**, 012502 (2005).

[173] Clemmen, S., Farsi, A., Ramelow, S., and Gaeta, A. L., Ramsey interference with single photons, Phys. Rev. Lett. **117**, 223601 (2016).

[174] Xia, K., Johnsson, M., Knight, P. L., and Twamley, J., Cavity-free scheme for nondestructive detection of a single optical photon, Phys. Rev. Lett. **116**, 023601 (2016).

[175] Liu, Z.-Y., Chen, Y.-H., Chen, Y.-C., Lo, H.-Y., Tsai, P.-J., Yu, I. A., Chen, Y.-C., and Chen, Y.-F., Large Cross-Phase Modulations at the Few-Photon Level, Physical Review Letters **117**, 203601 (2016).

[176] Xiao, Y., Spectral line narrowing in electromagnetically induced transparency, Modern Physics Letters B **23**, 661 (2009).

[177] Kalb, N., Reiserer, A., Ritter, S., and Rempe, G., Heralded Storage of a Photonic Quantum Bit in a Single Atom, Phys. Rev. Lett. **114**, 220501 (2015), 36.

[178] Tanji, H., Ghosh, S., Simon, J., Bloom, B., and Vuletić, V., Heralded single-magnon quantum memory for photon polarization states, Phys. Rev. Lett. **103**, 043601 (2009).

[179] Simon, C., de Riedmatten, H., Afzelius, M., Sangouard, N., Zbinden, H., and Gisin, N., Quantum repeaters with photon pair sources and multimode memories, Phys. Rev. Lett. **98**, 190503 (2007).

[180] Reim, K. F., Michelberger, P., Lee, K. C., Nunn, J., Langford, N. K., and Walmsley, I. A., Single-photon-level quantum memory at room temperature, Phys. Rev. Lett. **107**, 053603 (2011).

[181] Reim, K. F., Nunn, J., Lorenz, V. O., Sussman, B. J., Lee, K. C., Langford, N. K., Jaksch, D., and Walmsley, I. A., Towards high-speed optical quantum memories, Nat Photon **4**, 218 (2010).

[182] Michelberger, P. S., Champion, T. F. M., Sprague, M. R., Kaczmarek, K. T., Barbieri, M., Jin, X. M., England, D. G., Kolthammer, W. S., Saunders, D. J., Nunn, J., and Walmsley, I. A., Interfacing ghz-bandwidth heralded single photons with a warm vapour raman memory, New Journal of Physics **17**, 043006 (2015).

[183] Saunders, D. J., Munns, J. H. D., Champion, T. F. M., Qiu, C., Kaczmarek, K. T., Poem, E., Ledingham, P. M., Walmsley, I. A., and Nunn, J., Cavity-enhanced room-temperature broadband raman memory, Phys. Rev. Lett. **116**, 090501 (2016).

[184] Wolters, J., Buser, G., Horsley, A., Beguin, L., Jöckel, A., Jahn, J.-P., Warburton, R. J., and Treutlein, P., Simple atomic quantum memory suitable for semiconductor quantum dot single photons, arXiv 1703.00489

[185] Clausen, C., Usmani, I., Bussieres, F., Sangouard, N., Afzelius, M., de Riedmatten, H., and Gisin, N., Quantum storage of photonic entanglement in a crystal, Nature **469**, 508 (2011).

[186] Saglamyurek, E., Jin, J., Verma, V. B., Shaw, M. D., Marsili, F., Nam, S. W., Oblak, D., and Tittel, W., Quantum storage of entangled telecom-wavelength photons in an erbium-doped optical fibre, Nature Photonics **9**, 83 (2015).

[187] Lettner, M., Mücke, M., Riedl, S., Vo, C., Hahn, C., Baur, S., Bochmann, J., Ritter, S., Dürr, S., and Rempe, G., Remote Entanglement between a Single Atom and a Bose-Einstein Condensate, Physical Review Letters **106**, 210503 (2011).

[188] Ritter, S., Nolleke, C., Hahn, C., Reiserer, A., Neuzner, A., Uphoff, M., Mucke, M., Figueroa, E., Bochmann, J., and Rempe, G., An elementary quantum network of single atoms in optical cavities, Nature **484**, 195 (2012).

[189] Ekert, A. K., Quantum cryptography based on Bell's theorem, Physical Review Letters **67**, 661 (1991).

[190] Xu, F., Qi, B., Liao, Z., and Lo, H.-K., Long distance measurement-device-independent quantum key distribution with entangled photon sources, Applied Physics Letters **103**, 061101 (2013).

[191] Satoh, Takahiko, Franois Le Gall, and Hiroshi Imai. "Quantum network coding for quantum repeaters." Physical Review A 86, no. 3 (2012): 032331.